Assessing REE-phosphate mineral chemistry for ISCG exploration.

Travis Batch[1,2], Caroline Tiddy[1,2], Adrienne Brotodewo[1,2], David Giles[1,2]
[1] *Future Industries Institute, University of South Australia, Mawson Lakes, South Australia, Australia*
[2] *MinEx CRC, University of South Australia, Mawson Lakes, South Australia, Australia*

Abstract. Challenges related to thick cover sequences that bury rocks prospective for and/or hosting mineralisation make exploration challenging and financially risky. In response geochemical targeting tools based on mineral chemistry are being developed to aid deep exploration. One such tool being developed is based on the mineral chemistry of REE-bearing phosphate minerals (monazite, rhabdophane) to indicate proximity to Cu-Au ore deposits. To develop this tool, examples from known ore deposits must be tested. Here we present the initial results from the Jericho iron sulfide-copper-gold (ISCG) deposit in the Cloncurry District, Queensland, Australia. Metamorphic REE-bearing phosphates can be distinguished from mineralisation-associated hydrothermal REE-bearing phosphates based on Ca concentrations in combination with Th and S concentrations.

1 Introduction

The successful discovery of ore deposits is becoming increasingly difficult as explorers are forced to search within prospective terranes buried beneath thick cover sequences. This challenge is reflected in increased expenditure and declining rates of discovery. Decreasing rates of discovery are impacting global supplies of minerals, especially critical elements such as copper and rare-earth elements (REE), that are essential for the energy transition. To ensure we reach this future, more mineral deposits containing these critical minerals are required. New techniques are being developed for the exploration toolkit to increase the success rate of deposit discovery. Such techniques include the development of geochemical targeting tools that use mineral chemistry to understand proximity to ore deposits.

REE-bearing phosphates (e.g. monazite) are an ideal candidates for such a geochemical targeting tool, as these minerals occur in most geological environments and their chemistry can easily alter in response to changing environmental conditions, including those associated with mineralisation (Forbes et al. 2015; Tiddy et al. 2021). They can also be used as indicator minerals for mineralisation (McClenaghan et al. 2017; Layton-Matthews and McClenaghan 2022). Here, we consider the chemistry of REE-bearing phosphate minerals for iron sulfide-copper-gold (ISCG) exploration.

The Cloncurry District in Queensland, Australia (Figure 1) hosts a spectrum of iron oxide-copper-gold (IOCG) and ISCG deposits. IOCG deposits includes Ernest Henry, E1, Starra line and Osborne, and ISCG deposits include Eloise, Kulthor and Jericho. This study focusses on the Jericho ISCG deposit (14.1 Mt @ 1.46% Cu, 0.29 g/t Au and 1.6 g/t Ag; Demetallica 2022).

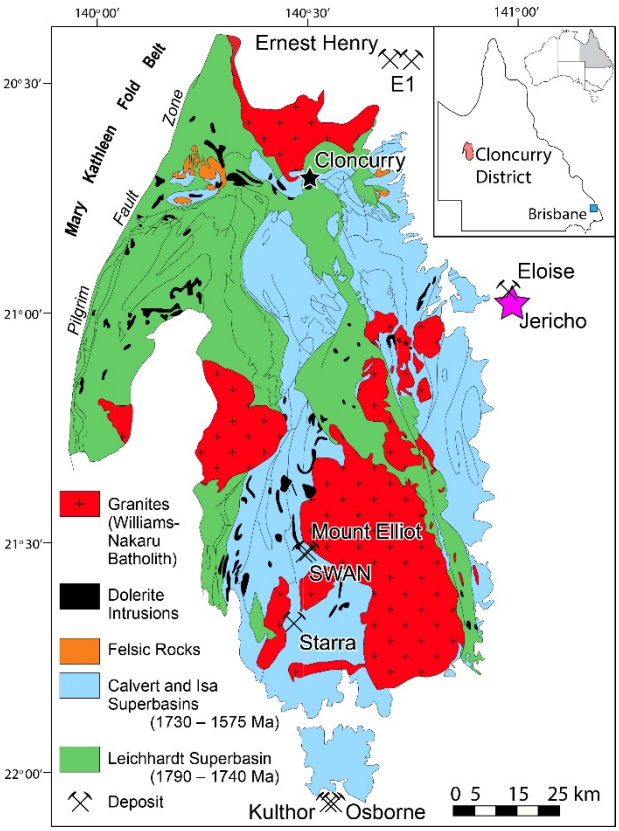

Figure 1. Extent of outcrop in the Cloncurry District in Queensland, Australia. Areas outside of the coloured areas east of the Pilgrim Fault Zone lie beneath sedimentary cover sequences. The location of Jericho is shown by the purple star. Locations of other major IOCG/ISCG deposits are shown. Modified after Betts et al. (2006). Inset: Map of Queensland, Australia showing the location of the Cloncurry District.

Jericho is located to the east of the Cloncurry District, approximately 58 km south-east of the Cloncurry township and about 2.5 km south of the Eloise ISCG deposit. Sulfide mineralisation is hosted in psammite and psammopelite primarily composed of K-feldspar, quartz, biotite, and relict tourmaline. Foliation is defined by the orientation of biotite. Low-grade metamorphic minerals (hornblende, scapolite) indicate the host rock has been metamorphosed and triple junctions at quartz grain boundaries indicate recrystallisation.

Mineralisation is dominated by pyrrhotite and chalcopyrite and occurs as three parallel lodes, aptly named J1, J2 and J3. They all dip steeply to the west, sub-parallel to foliation. Lodes have a strike

length of ~3.5 km and have a maximum width of ~13 m. J1 and J2 are the main mineralised lodes and occur 120 m apart.

2 Methods and Results

2.1 Sample Selection, Preparation and SEM Analysis

Polished thin sections for the J1 lode at Jericho were provided by Demetallica. Petrographic analysis was performed on the thin section before being coated with carbon. REE-bearing phosphates were imaged with a Zeiss Merlin FEG SEM. Operating conditions included a 20 kV accelerating voltage, 3 nA probe current and a working distance of 10 mm. Backscatter electron (BSE) images (Figure 2a) and energy dispersive spectroscopy (EDS) maps (Figure 2b-d) were used to locate REE-bearing phosphates and identify surrounding mineral phases. Apatite was found commonly associated with REE-bearing phosphates, likely indicating some formed from a fluid-apatite reaction, where REEs are leached from apatite and bond with P (Harlov et al. 2002, 2005; Harlov and Förster 2003).

Three textural types of REE-bearing phosphates were found at Jericho. The first are metamorphic, paragenetically late in the host rock, occasionally associated with sulfide minerals, and are large compared to other textural types, generally being 50 – 400 µm in length. The second group are hydrothermal, commonly associated with sulfide minerals, sometimes associated with apatite, and are small, normally 10 – 100 µm with rare grains up to 200 µm in length. A third textural type of phosphate is also hydrothermal, occurs as veins up to 1 mm long and 20 µm in width. These are the least common texture of phosphates.

2.2 Electron Probe Microanalyser (EPMA)

EPMA data was collected at Adelaide Microscopy, University of Adelaide using a Cameca SXFive Electron Microprobe. Light to middle REEs (La – Dy), U, Th, Ca, Al, Si, P, As and S were analysed. Oxygen was calculated from stoichiometric oxides. Combined conditions were used, with a 15 kV accelerating voltage and 20 nA beam current used for La, Ce, Pr, Nd, Sm, Al, Si, P and Th, while a 15 kV accelerating voltage and 100 nA beam current were used for Eu, Gd, Tb, Dy, Y, Ca, U, S and As. Results were filtered to only include analytical totals from 90 – 105 wt.%, Al + Si < 10 wt.%, Ca < 5 wt.% and S < 1 wt.%. This ensured the signal from surrounding mineral phases was limited. Filtered analyses were subsequently normalised to 100 wt.%

Metamorphic REE-bearing phosphates were characterised by higher U and Th concentrations and lower Ca and S concentrations than their hydrothermal counterparts. The Eu anomaly in metamorphic REE-bearing phosphates (Eu/Eu* = 0.02 – 1.97) was also much more variable than hydrothermal REE-bearing phosphates (Eu/Eu* = 0.15 – 0.64). Prior to normalisation, metamorphic REE-bearing phosphates typically have analytical EPMA totals between 97 and 100%, compared to hydrothermal REE-bearing phosphate analytical totals between 90 and 98% (Figure 3).

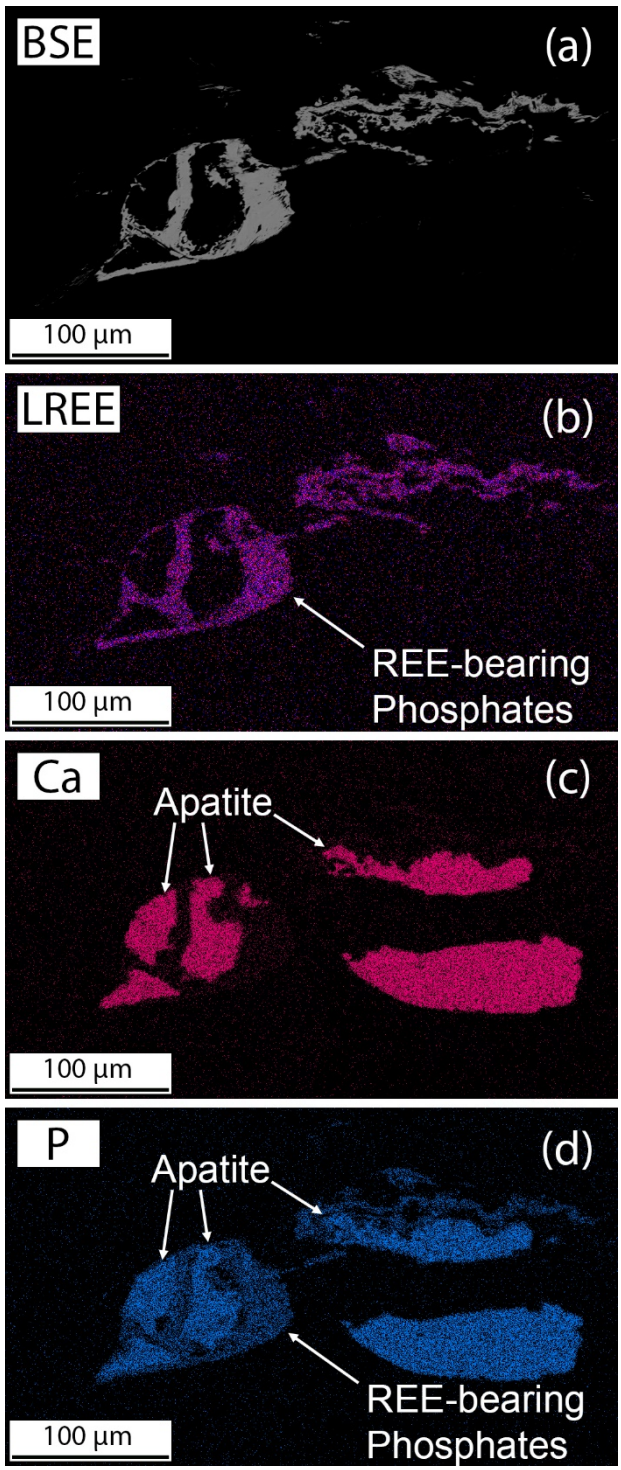

Figure 2. a BSE image and **b-d** EDS maps of REE-bearing phosphates and nearby mineral phases. Coincident LREE and P peaks show the presence of REE-bearing phosphates. Phosphates are associated with apatite as shown by coincident Ca and P peaks.

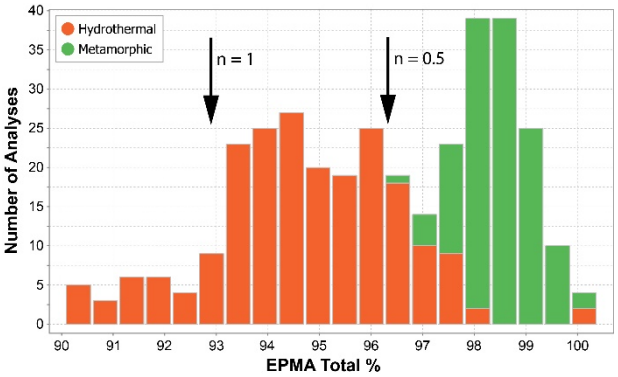

Figure 3. EPMA totals before normalisation. Arrows mark the EPMA total expected when the stoichiometric amount of water for rhabdophane is 0.5 and 1.

3 Discussion

REE-phosphate minerals present at Jericho could be monazite or rhabdophane. Monazite ($LREEPO_4$) and rhabdophane ($LREEPO_4 \cdot n\ H_2O$, where n = 0.5 – 1; where n = 1 in the rhabdophane formula, it can incorporate roughly 7 – 8 wt.% water) are geochemically indistinguishable when analysed by EDS, however the deficit in analytical totals from EPMA analysis can allow broad distinction between the two minerals whereby the water contained within rhabdophane is too light to be analysed by EPMA, and is reflected in low analysis totals. Both minerals are related, as monazite can alter to rhabdophane during low-grade and retrograde alteration in the presence of hydrothermal fluids (Berger et al. 2008; Nagy and Draganits 1999; Nagy et al. 2002).

At Jericho, the metamorphic REE-bearing phosphates with analytical totals between 97 and 100% (Figure 3) are interpreted to be monazite. The smaller hydrothermal grains that are associated with sulfides and the hydrothermal phosphate phase in the veins which yield low analytical totals between 90 and 98 wt.% (Figure 3) are interpreted to be rhabdophane. At Jericho, Ca concentrations can be used to discriminate between metamorphic and hydrothermal REE-bearing phosphates, while S and Th concentrations can mostly discriminate between the two types. Low Th is typical of hydrothermal REE-bearing phosphates (Schandl and Gorton 2004). Compared to metamorphic monazite from the Gawler Carton (Forbes et al. 2015), metamorphic monazite from Jericho has lower concentrations of U, Th and Ca, and higher concentrations of light REEs.

There is also a notable difference between the space groups of monazite and rhabdophane. Monazite is in the monoclinic P21/n space group (Ni et al. 1995) while rhabdophane is in the hexagonal $P6_222$ space group (Mooney 1950). With this structural difference, rhabdophane tends towards an apatite stoichiometry rather than a monazite stoichiometry (Poitrasson et al. 2000; Nagy et al. 2002; Figure 4).

The stability fields of monazite and rhabdophane are close at low temperatures (Poitrasson 2005) with fluid activity dictating which mineral is formed (Krenn and Finger 2007). The mineralising fluid at Jericho may have been the cause of rhabdophane formation considering the close relationship between rhabdophane and apatite (fluid-apatite reactions), and rhabdophane with sulfide minerals. This would indicate that rhabdophane formation is coeval with mineralisation and its chemistry reflects its association with mineralisation. Its presence also indicates mineralisation at Jericho occurred at low temperatures.

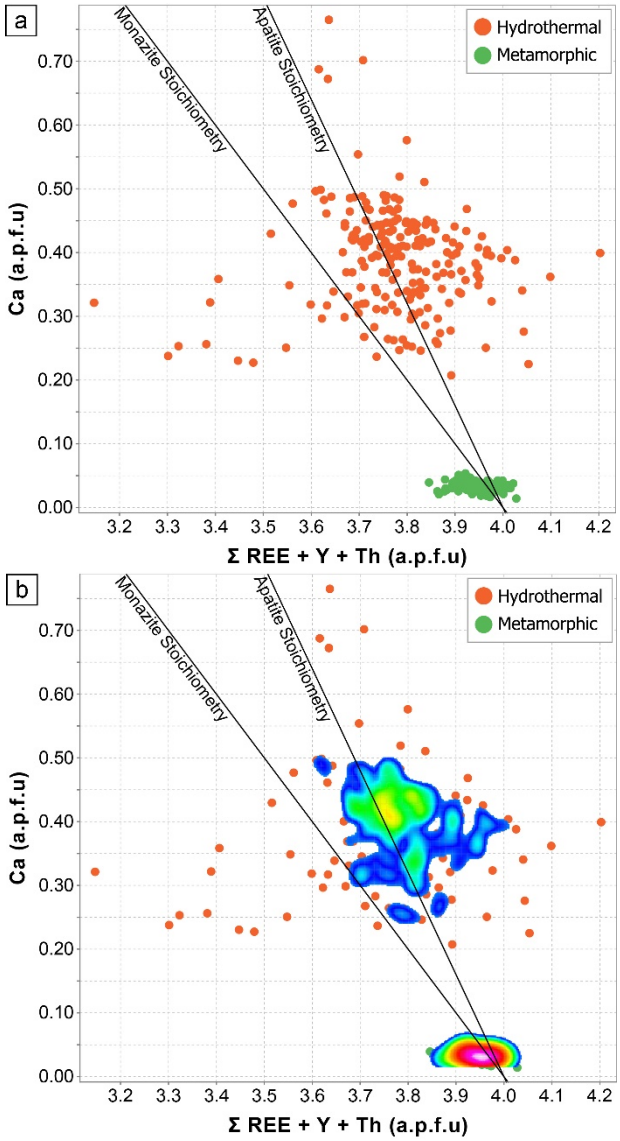

Figure 4. a Atomic proportions within REE-bearing phosphates at Jericho, recalculated based on 16 oxygen atoms per formula unit (a.p.f.u). Lines indicate ideal monazite and apatite stoichiometries (from Poitrasson et al. 2000). **b** As indicated by the heat map, **m**ost hydrothermal REE-bearing phosphates cluster around the apatite stoichiometry line. Metamorphic REE-bearing phosphates contain < 0.2 wt.% Ca, so all cluster around the bottom of the graph.

4 Conclusion

Initial development of a geochemical targeting tool using REE-bearing phosphate mineral chemistry shows promise for ISCG exploration, being able to

distinguish between different phases associated and unassociated with the mineralising event at Jericho. Ca, S and Th have been shown to be the main discriminators for rhabdophane and metamorphic monazite. Hydrothermal REE-bearing phosphates were found to be rhabdophane based on analytical totals and their tendancy towards an apatite stoichiometry, indicating Jericho is a low temperature system. Further development of this exploration tool using REE-bearing phosphates will be achieved by comparing this data to other ISCG deposits in the area (Kulthor and Eloise).

Acknowledgements

The authors would like to acknowledge the contributions of Tony Belperio and Glen Little for providing the samples. Nobuyuki Kawashima from the University of South Australia is thanked for his help with the collection of SEM and EDS data. Benjamin Wade from Adelaide Microscopy is thanked for his help with the collection of EPMA data. This project was kindly supported by MinEx CRC whose activities are funded by the Australian Government's Cooperative Research Centre Programme.

References

Berger A, Gnos E, Janots E, Fernandez A, Giese J (2008) Formation and composition of rhabdophane, bastnäsite and hydrated thorium minerals during alteration: Implications for geochronology and low-temperature processes. Chem Geol 254(3):238–248 https://doi.org/10.1016/j.chemgeo.2008.03.006

Betts P, Giles D, Mark G, Lister G, Goleby B, Aillères L (2006) Synthesis of the Proterozoic evolution of the Mt Isa Inlier. Aust J Earth Sci 53(1):187–211. https://doi.org/10.1080/08120090500434625

Demetallica (2022) Jericho mineral resource delivers 62% increase in contained copper. Demetallica ASX Release. https://openbriefing.com.au/AsxDownload.aspx?pdfUrl=Report%2FComNews%2F20221024%2F02586599.pdf Accessed 31 October 2022

Forbes C, Giles D, Freeman H, Sawyer M, Normington V (2015) Glacial dispersion of hydrothermal monazite in the Prominent Hill deposit: An exploration tool. J Geochem Explor 156:10–33. https://doi.org/10.1016/j.gexplo.2015.04.011

Harlov D, Förster HJ, Nijland T (2002) Fluid-induced nucleation of (Y + REE)-phosphate minerals within apatite: Nature and experiment. Part I. Chlorapatite. Am Min 87(2–3):245–261. https://doi.org/10.2138/am-2002-2-306

Harlov D, Förster HJ (2003) Fluid-induced nucleation of (Y + REE)-phosphate minerals within apatite: Nature and experiment. Part II. Fluorapatite. Am Min 88(8–9):1209–1229. https://doi.org/10.2138/am-2003-8-905

Harlov D, Wirth R, Förster HJ (2005) An experimental study of dissolution-reprecipitation in fluorapatite: fluid infiltration and the formation of monazite. Contrib Miner Petrol 150(3):268–286. https://doi.org/10.1007/s00410-005-0017-8

Krenn E, Finger F (2007) Formation of monazite and rhabdophane at the expense of allanite during Alpine low temperature retrogression of metapelitic basement rocks from Crete, Greece: Microprobe data and geochronological implications. Lithos 95(1):130–147 https://doi.org/10.1016/j.lithos.2006.07.007

Layton-Matthews D, McClenaghan M (2022) Current techniques and applications of mineral chemistry to mineral exploration; examples from glaciated terrain: A review. Minerals 12(1):59. https://doi.org/10.3390/min12010059

McClenaghan M, Paulen R, Kjarsgaard I, Fortin R (2017) Rare earth element indicator minerals: An example from the Strange Lake deposit, Quebec and Labrador, eastern Canada. In: McClenaghan M, Layton-Matthews D (ed) Application of indicator mineral methods to bedrock and sediments, Geological Survey of Canada Open File 8345 pp 78–86. https://doi.org/10.4095/306305

Mooney R (1950) X-ray diffraction study of cerous phosphate and related crystals. I. Hexagonal modification. Acta Crystallographica 3(5):337–340 https://doi.org/10.1107/S0365110X50000963

Nagy G, Draganits E (1999) Occurrence and mineral-chemistry of monazite and rhabdophane in the Lower and? Middle Austroalpine tectonic units of the southern Sopron Hills (Austria).

Nagy G, Draganits E, Demény A, Pantó G, Árkai P (2002) Genesis and transformations of monazite, florencite and rhabdophane during medium grade metamorphism: Examples from the Sopron Hills, Eastern Alps. Chem Geol 191:25–46. https://doi.org/10.1016/S0009-2541(02)00147-X

Ni Y, Hughes J, Mariano A (1995) Crystal chemistry of the monazite and xenotime structures. Am Min 80(1–2):21–26 https://doi.org/10.2138/am-1995-1-203

Poitrasson F (2005) Experimental studies of the stability of monazite in aqueous solutions. Geochimica et Cosmochimica Acta 69(10):6 https://doi.org/10.1016/j.gca.2005.03.023

Poitrasson F, Chenery S, Shepherd T (2000) Electron microprobe and LA-ICP-MS study of monazite hydrothermal alteration: Implications for U-Th-Pb geochronology and nuclear ceramics. Geochimica et Cosmochimica Acta 64(19):3283–3297. https://doi.org/10.1016/S0016-7037(00)00433-6

Schandl E, Gorton M (2004) A textural and geochemical guide to the identification of hydrothermal monazite: Criteria of selection of samples for dating epigenetic hydrothermal ore deposits. Economic Geology 99(5):1027–1035. https://doi.org/10.2113/gsecongeo.99.5.1027

Schodde R (2017) Challenges of exploring under deep cover. AMIRA International's 11th Biennial Exploration Managers Conference, 28th – 31st March

Tiddy C, Zivak D, Hill J, Giles D, Hodgkison J, Neumann M, Brotodewo A (2021) Monazite as an exploration tool for iron oxide-copper-gold mineralisation in the Gawler Craton, South Australia. Minerals 11(8):809. https://doi.org/10.3390/min11080809

Alteration Footprints of Metasomatic Iron and Alkali-Calcic Systems in the Northern Norrbotten, Sweden

Olivier Blein[1], Matthieu Harlaux[1], Louise Corriveau[2], Edward P. Lynch[3], Tero Niiranen[4], Vladimir Lisitsin[5], Kathy Ehrig[6], Jean-François Montreuil[7], Blandine Gourcerol[1]
[1]BRGM, 3 avenue Claude-Guillemin, BP 36009 – 45060 Orléans cedex 2 - France
[2]Geological Survey of Canada, Natural Resources Canada, Québec City, Canada
[3]Geological Survey of Sweden, P.O. Box 670, SE-75128 Uppsala, Sweden
[4]Geological Survey of Finland GTK, P.O. Box 77, FI-96190 Rovaniemi, Finland
[5]Geological Survey of Queensland, Brisbane, Australia
[6]BHP-Olympic Dam, Adelaide, Australia
[7]MacDonald Mines Exploration, Toronto, Canada

Abstract. Metasomatic iron and alkali-calcic mineral systems include a wide range of deposits with critical and precious metals, notably IOA, IOCG, skarn, albitite-hosted U, iron-rich Co (Au, Bi, Cu), and polymetallic vein deposits. Host systems evolve along diagnostic metasomatic paths with: 1) Na (albitite) and local skarn, 2) high-temperature (HT) Ca-Fe, 3) HT K-Fe, 4) K and K-Ca-Mg (K-skarn), 5) low-temperature (LT) K-Fe and Ca-Mg-Fe-(Si, CO_2), and 6) epithermal alteration. In this contribution, we show that chalcopyrite-rich IOCG-style deposits from the Northern Norrbotten, Sweden, are characterized by early Na alteration overprinted by Ca-Fe and K-Fe alteration with a geochemical footprint distinct from magnetite-rich (Great Bear magmatic zone) or hematite-rich (Olympic Dam) IOCG deposits. The IOCG-style deposits from the Northern Norrbotten have similarities with some found in the Cloncurry district in Australia.

1 Introduction

Metasomatic iron and alkali-calcic (MIAC) mineral systems chemically and texturally transform the entire upper crust across <500 km^2, precipitating successive metasomatic alteration facies rich in iron, alkali, and alkaline earth (e.g. Na, Ca) elements. Each facies shows distinct geochemical signatures, metal associations, and genetically linked deposits. Alteration footprints are thus key to explore mineral systems at deposit to province scales, and to interpret deposit types (Corriveau et al. 2016, 2022a-c; Day et al. 2016; Montreuil et al. 2016; Blein et al. 2022).

Globally, MIAC systems comprise regional albitite corridors (Na) and local skarn (±W, Fe), followed by HT Ca-Fe alteration and iron oxide-apatite (IOA) deposits, iron-rich Ni and REE deposits, HT Ca-K-Fe and iron-rich Co deposits, and HT K-Fe to LT K-Fe and Ca-Mg-Fe-Si-CO_2, with IOCG and iron-rich to iron-poor deposits (Corriveau et al. 2022a-c). Albitite-hosted deposits, deposits with iron-rich silicates, carbonates or sulfides instead of oxides, and polymetallic vein (e.g. five-element) deposits also occur (Montreuil et al. 2015; Hofstra et al. 2021; Corriveau et al. 2022c).

In this contribution, we characterize the metasomatic footprints of IOCG-style deposits in the Northern Norrbotten province (Sweden), and we show similarities to IOCG deposits from the Cloncurry district, Australia. These results allow for improving metallogenic models and optimizing the exploration for critical mineral resources in Europe and beyond.

2 Alteration footprints of MIAC

Alteration facies in MIAC systems display highly distinctive molar proportions of Na, Ca, K, Fe, and Mg which can be visualized in diagnostic barcodes as proportions of intense alteration and overprints significantly differ from those in igneous, metamorphic, or sedimentary rocks. Least-altered samples have relatively balanced proportions of these cations. In contrast, metasomatized rocks display barcodes with one or two dominant elements and their distinctive associations serve as proxies for discriminating alteration facies. Plotting Na-Ca-Fe-K-Mg barcodes in the Alteration Index Iron-Oxide Copper-Gold (AIOCG) diagram of Montreuil et al. (2013) provides a visual representation of the evolution of metasomatic paths for MIAC systems. Increasing albitization of a least-altered rock is discriminated from overprints on albitite and the transition from albitite to HT Ca-Fe alteration by the diagnostic proportions of Ca-Fe-K-Mg of the overprinting alteration facies and the decreasing trend of Na from the Na field in the AIOCG diagram (Blein et al. 2022; Corriveau et al. 2022b).

In Figure 1A, strongly altered samples from the magnetite-rich deposits of the Great Bear magmatic zone (GBMZ) in Canada define a prograde metasomatic path (in blue) across the fields of the five main alteration facies (Na, HT Ca-Fe, HT K-Fe, K, and LT K-Fe). This dataset is complemented by the footprint of the hematite-rich Olympic Dam deposit. The footprint of increasing alteration of least-altered rocks (in yellow) is illustrated by the trend from least-altered granite to K-Fe alteration in Figure 1B along which Na-Ca proportions decrease and K-Fe proportions increase. Therefore, IOCG deposits having abundant iron oxides fall within the Fe-rich fields of the AIOCG diagram, while IOA deposits plot within the Fe-rich, Ca-Fe field, and albitite-hosted deposits along a trend between the Na field of the albitite and the field of the alteration overprint(s) (Blein et al. 2022; Corriveau et al. 2022b).

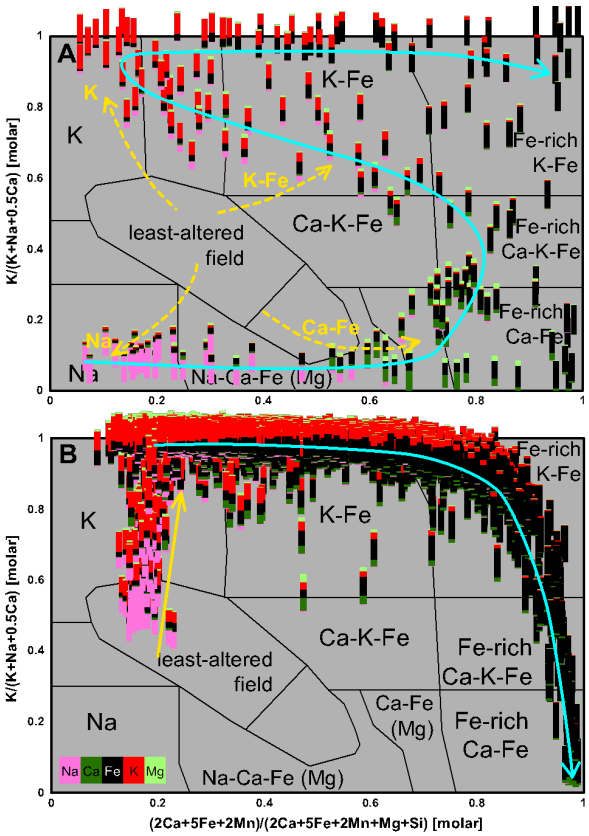

Figure 1. Evolution of metasomatic paths of the GBMZ (**A**) and Olympic Dam deposit (**B**), modified from Blein et al. (2022). Data: Corriveau et al. (2015), and BHP Olympic Dam (unpublished data; boreholes RD2366 and RD2382). Blue trend: most intense alteration. Yellow trend: least to most altered trends.

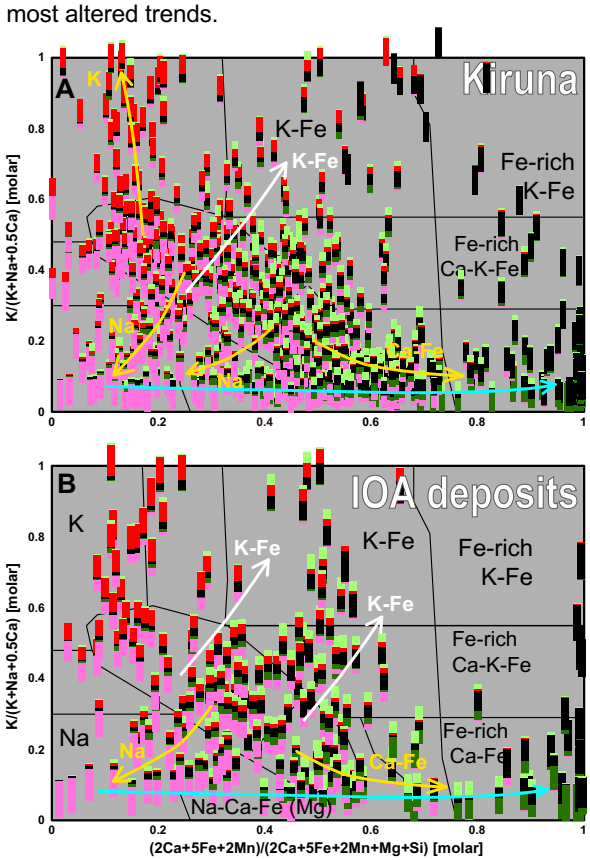

Figure 2. Diagnostic trends of the MIAC system for the Kiruna area (**A**), and IOA deposits subset (**B**). Data: Geological Survey of Sweden (SGU) lithogeochemistry database. White trend: overprints on albitite.

3 The Northern Norrbotten district, Sweden

The MIAC systems in the Northern Norrbotten formed in an intracontinental back-arc basin and were associated with comagmatic volcano-plutonic rocks dated at ca. 1.89-1.86 Ga. These processes resulted in the formation of IOA deposits, such as Kiruna and Malmberget, before undergoing crustal shortening and basin inversion (Martinsson et al. 2016; Sarlus et al. 2020; Andersson et al. 2021).

Epigenetic Cu-Au and Au deposits formed subsequently and are hosted within the basin inversion structures; those with iron oxide and iron silicate gangue minerals were assigned to IOCG such as the Nautanen deposit (Andersson et al. 2021; Bauer et al. 2022). The Northern Norrbotten district also includes Paleoproterozoic stratabound sulfide, iron skarn, and BIF deposits (Billström et al. 2010). Deposits assigned to the IOCG also occur in the Pajala-Kolari region (Niiranen et al. 2007).

Lithogeochemical samples collected within 20 km of the main deposits in the Kiruna area define trends from the least-altered field to the Na, K, K-Fe, and Ca-Fe fields (Fig. 2A). Samples close (< 2 km) to IOA deposits define a horizontal path starting from the Na field through the Na-Ca-Fe and Ca-Fe fields, and trends from the least-altered field to Na and Ca-Fe fields (Fig. 2B). The Na to Fe-rich Ca-Fe and Na to K-Fe trends recorded by the Fe-rich with Na barcodes and uneven increase of the normal Ca-Fe-K-Mg proportions of least-altered rocks as Na decreases is typical of albitite overprinted by a Ca-Fe or K-Fe alteration or transitioning to HT Ca-Fe alteration. Skarn (Ca-Mg barcodes), Fe-rich skarn (Ca-Fe-Mg barcodes), and apatite-rich ore (Ca-Fe barcodes) plot along a Na-Ca-Fe to Fe-rich Ca-Fe trend (Fig. 2B, Corriveau et al. 2022b).

Samples within 20 km of the main deposits in the Gallivare area plot essentially along least-altered to Na, least-altered to Ca-K-Fe and K-Fe or K trends, and albitite transitioning to Fe-rich Ca-Fe (Fig. 3A). The Nautanen deposit records a Ca-K-Fe to K-Fe alteration with localized Ca-Fe metasomatism (Fig. 3B) while for the Malmberget deposit the evolution from Na-Ca-Fe to K-Fe and Fe-rich Ca-Fe fields is typical of albitite overprinted by K-Fe alteration and transitioning to HT Ca-Fe alteration (Fig. 3C).

Samples within 20 km of the main deposits in the Pajala-Kolari area plot along least-altered felsic and mafic to Na trends, least-altered to K and K-Fe trends, and albitized mafic to the Fe-rich Ca-Fe trend (Fig. 4A). The Cu-Au deposits assigned to IOCGs fall along these trends with a better-defined path marked by decreasing Na and increasing Ca-Mg or Fe (Fig. 4B). Similar to the Kiruna district, skarn alteration plots along the Ca-Fe and Fe-rich Ca-Fe fields, with Ca-Mg±Fe-rich barcodes.

4 The Cloncurry district, Australia

In the Cloncurry district, 1.85–1.60 Ga supracrustal sequences intruded by several generations of granitoids hosts several magnetite-bearing Cu-Au

deposits, including the Ernest-Henry magnetite-group IOCG deposit (Williams 2010). The IOCG deposits consist of iron oxide breccias among regional, albite-rich Na-(Ca) alteration and proximal HT K-Fe and LT Ca-Mg-Fe alteration synchronous with and hosting most of the Cu-Au mineralization, which typically overprints the earlier Na-(Ca) alteration (Marshall and Oliver 2008; Corriveau et al. 2022a).

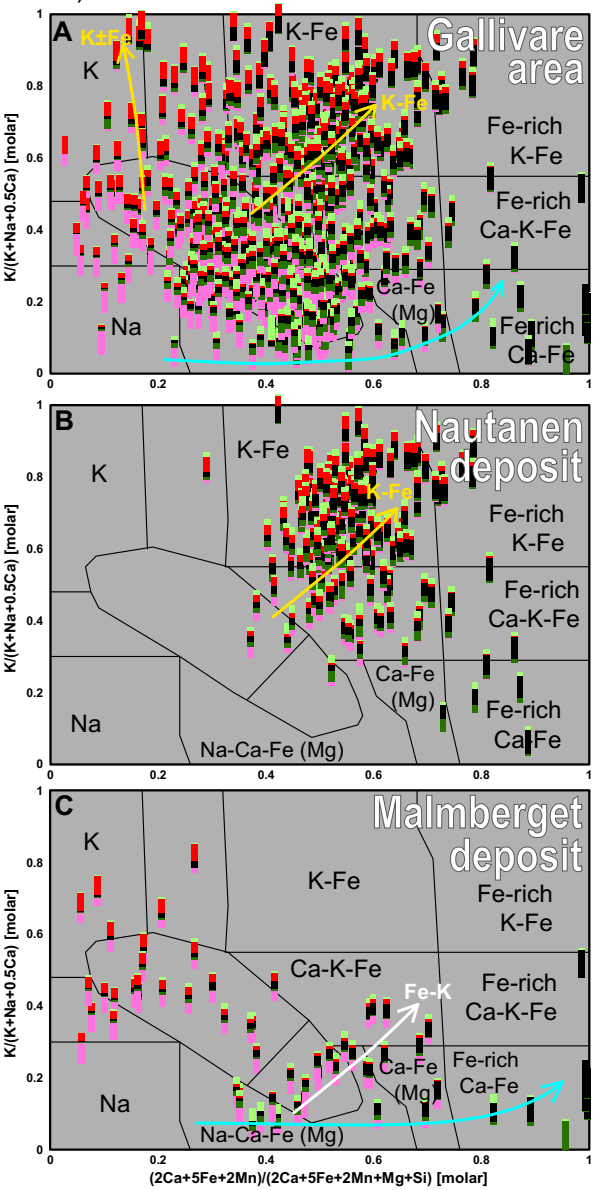

Figure 3. Diagnostic trends of the samples from the Gallivare area (**A**), Nautanen IOCG (**B**), and Malmberget IOA deposits (**C**). Data: SGU lithogeochemistry database.

Samples from the magnetite-rich IOCG Ernest-Henry deposit plot in the K-Fe, Ca-K-Fe, Ca-Fe, and Fe-rich alteration fields with few least-altered samples (Fig. 5A). High Na proportions reaching the Fe-rich fields are expected considering the preserved evidence of multiple overprints on albitite in the deposit (Corriveau et al. 2022a, b). Samples from the magnetite-rich Cu-Au skarn of the SWAN deposit define a horizontal Na to Fe-rich Ca-Fe trend (in blue; Fig. 5B). Some samples present a K-Fe alteration superimposed on earlier albitite (in white).

Similar to the Northern Norrbotten district, the Cloncurry district is characterized by extensive Na alteration overprinted by Ca-Fe and K-Fe alterations.

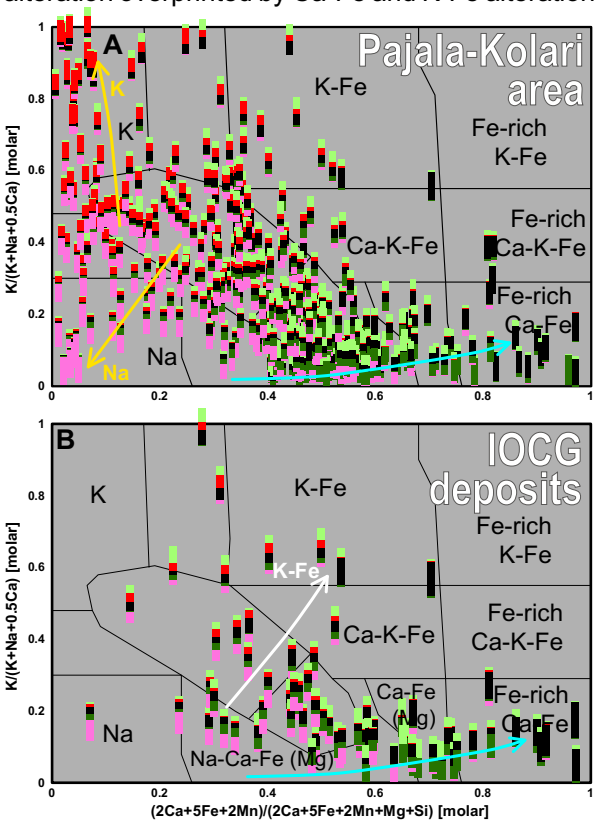

Figure 4. Diagnostic trends of the samples from the Pajala-Kolari area (**A**), and deposits assigned to the IOCG type (**B**). Data: SGU lithogeochemistry database and Rasilainen et al. (2007).

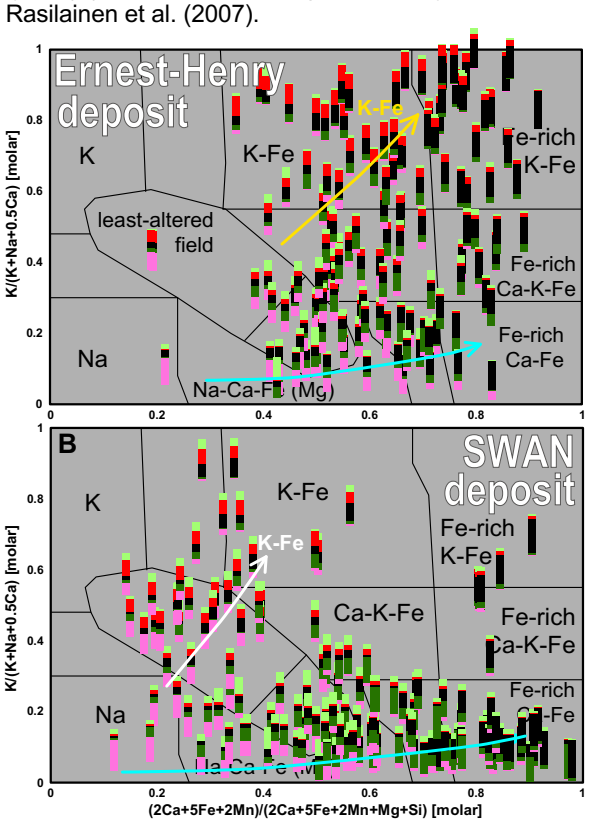

Figure 5. Diagnostic trends of the samples from the Ernest-Henry (**A**), and SWAN (**B**) IOCG deposits from the Cloncurry district. Data: Dhnaram et al. (2021).

5 Discussion

In the Pajala-Kolara area, Cu-Au deposits formally assigned to the IOCG class show metasomatic footprints which are distinct from magnetite- and hematite-rich IOCG deposits such as Olympic Dam (Fig. 1B) and Ernest-Henry (Fig. 5A). The alteration footprint is typical of HT Ca-Fe and K-Fe trends overprinting and increasingly replacing regionally albitized and/or scapolitized host rocks as exemplified by IOA deposits of the Kiruna district. In the Pajala-Kolari area, Cu-Au mineralization has HT Ca-Fe ± weak HT K-Fe alteration overprinting skarn and albitite. According to the ore deposition model and case studies by Corriveau et al. (2022c), additional types of mineralization may occur within these Scandinavian MIAC systems and their known deposits.

Acknowledgments

Financial support from the European Union's Horizon Europe research and innovation program under Grant agreement n°1010557357, EIS – Exploration Information System (https://eis-he.eu). Research took place in collaboration with the Targeted Geoscience Initiative program and is Natural Resources Canada contribution 20220593.

References

Bauer TE, Lynch EP, Sarlus Z, Drejing-Carroll D, Martinsson O, Metzger N, Wanhainen, C (2022) Structural controls on iron oxide copper-gold mineralization and related alteration in a Paleoproterozoic supracrustal belt: Insights from the Nautanen deformation zone and surroundings, Northern Sweden. Econ Geol 117:327–359

Billström K, Broman C, Eilu P, Martinsson O, Niiranen T, Ojala J, Wanhainen C, Weihed P (2010) IOCG and related mineral deposits of the Northern Fennoscandian Shield. In: Porter TM (ed) Hydrothermal Iron Oxide Copper-Gold and related deposits: A global perspective advances in the understanding of IOCG deposits, v. 4. PGC Publishing, Adelaide, p. 381–414

Blein O., Corriveau L, Montreuil J-L, Ehrig K, Fabris A, Reid A, Pal D (2022) Geochemical signatures of metasomatic ore systems hosting IOCG, IOA, albite-hosted uranium and filiated deposits: a tool for process studies and mineral exploration. In: Corriveau L, Potter EG, Mumin AH (eds) Mineral systems with iron oxide copper-gold (IOCG) and affiliated deposits. Geol Assoc Canada, Special Paper 52, p. 263–298

Corriveau L, Lauzière K, Montreuil J-F, Potter EG, Hanes R, Premont S (2015) Dataset of geochemical data from iron oxide alkali altered mineralizing systems of the Great Bear magmatic zone (NWT. Geol Survey Canada, Open File 7643, 19 p.

Corriveau L, Montreuil J-F, Potter EG (2016) Alteration facies linkages among IOCG, IOA and affiliated deposits in the Great Bear magmatic zone, Canada. Econ Geol 111:2045–2072

Corriveau L, Montreuil JF, Potter EG, Ehrig K, Clark JM, Mumin AH, Williams PJ (2022a) Mineral systems with IOCG and affiliated deposits: part 1 – metasomatic footprints of alteration facies. In: Corriveau L, Potter EG, Mumin AH (eds) Mineral systems with iron oxide copper-gold (IOCG) and affiliated deposits: Geol Assoc Canada, Special Paper 52, p. 113–158

Corriveau L, Montreuil JF, Blein O, Ehrig K, Potter EG, Fabris A, Clark JM (2022b) Mineral systems with IOCG and affiliated deposits: part 2 – geochemical footprints. In: Corriveau L, Potter EG, Mumin AH (eds) Mineral systems with iron oxide copper-gold (IOCG) and affiliated deposits. Geol Assoc Canada, Special Paper 52, p. 159–204

Corriveau L, Montreuil J-F, Potter EG, Blein O, de Toni, AF (2022c) Mineral systems with IOCG and affiliated deposits: part 3 – metal pathways and ore deposit model. In: Mineral systems with iron oxide copper-gold (IOCG) and affiliated deposits, Corriveau L, Potter EG, Mumin AH (eds) Geol Assoc Canada, Special Paper 52, p. 205–245

Day WC, Slack JF, Ayuso RA, Seeger CM (2016) Regional geologic and petrologic framework for iron oxide ± apatite ± rare earth element and iron oxide copper-gold deposits of the Mesoproterozoic St. Francois Mountains terrane, southeast Missouri, USA. Econ Geol 111:1825–1858

Dhanaram C, Lisitsin V, Gopalakrishnan S, Tang J, Killen D, von Gnielinski F (2021) Eastern Mount Isa Province IOCG data package. GSQ Technical Notes 2021/06

Hofstra A, Lisitsin V, Corriveau L, Paradis S, Peter J, Lauzière K, Lawley C, Gadd M, Pilote J-L, Honsberger I, Bastrakov E, Champion D, Czarnota K, Doublier M, Huston D, Raymond O, VanDerWielen S, Emsbo P, Granitto M, Kreiner D (2021) Deposit classification scheme for the critical minerals mapping initiative global geochemical database. USGS, Open-File Report 2021–1042, 60 p

Marshall LJ, Oliver NHS (2008) Constraints on hydrothermal fluid pathways within Mary Kathleen Group stratigraphy of the Cloncurry iron-oxide-copper-gold district, Australia. Precamb Res 163:151–158

Martinsson O, Billström K, Broman C, Weihed P, Wanhainen C (2016) Metallogeny of the northern Norrbotten ore province, northern Fennoscandian Shield with emphasis on IOCG and apatite-iron ore deposits. Ore Geol Rev 78: 447–492

Montreuil J-F, Corriveau L, Grunsky EC (2013) Compositional data analysis of IOCG systems, Great Bear magmatic zone, Canada: to each alteration types its own geochemical signature. GEEA 13: 229–247

Montreuil J-F, Corriveau L, Potter EG (2015) Formation of albitite-hosted uranium within IOCG systems: The Southern Breccia, Great Bear magmatic zone, Northwest Territories, Canada. Miner Depos 50:293–325

Montreuil J-F, Corriveau L, Potter EG, De Toni AF (2016) On the relation between alteration facies and metal endowment of iron oxide–alkali-altered systems, southern Great Bear magmatic zone (Canada). Econ Geol 111:2139–2168

Niiranen T, Poutiainen M, Mänttäri I (2007) Geology, geochemistry, fluid inclusion characteristics, and U–Pb age studies on iron oxide–Cu–Au deposits in the Kolari region, northern Finland. Ore Geol Rev 30:75–105

Rasilainen K, Lahtinen R, Bornhost TJ (2007) The rock geochemical database of Finland manual. Geologian tutkimuskeskus, Tutkimusraportti 164 – Geological Survey of Finland, Report of Investigation 164, 38 p

Sarlus Z, Andersson UB, Martinsson O, Bauer TE, Wanhainen C, Andersson JBH, Whitehouse MJ (2020) Timing and origin of the host rocks to the Malmberget iron oxide-apatite deposit, Sweden. Precamb Res 342:105652

Williams PJ (2010) "Magnetite-group" IOCGs with special reference to Cloncurry and Northern Sweden: settings, alteration, deposit characteristics, fluid sources, and their relationship to apatite-rich iron ores. In: Corriveau L, Mumin AH (eds) Exploring for iron oxide copper gold deposits: Canada and global analogues. Geol Assoc Canada, Short Course Notes 20:23–38

Williams PJ, Barton MD, Fontboté L, deHaller A, Johnson DA, Mark G, Oliver NHS, Marschik R (2005) Iron oxide-copper-gold deposits: Geology, space-time distribution and possible modes of origin. Econ Geol 100th, 371–405

Similarities, yet differences: Olympic Dam, Oak Dam West, Wirrda Well, Island Dam and Acropolis IOCG deposits, Olympic Cu-Au Province, South Australia

Kathy Ehrig[1,2], Cristiana L. Ciobanu[2], Nigel J. Cook[2], Vadim S. Kamenetsky[3], Maya Kamenetsky[3], Jocelyn McPhie[3]

[1]BHP Olympic Dam, 10 Franklin St., Adelaide, South Australia, 5000, Australia
[2]School of Chemical Engineering, University of Adelaide, Adelaide, South Australia, 5005, Australia
[3]School of Natural Sciences, University of Tasmania, Hobart, Tasmania, 7005, Australia

Abstract. The Olympic Cu-Au Province hosts not only one of the world's largest Cu-Au-U deposits, Olympic Dam, but also Prominent Hill and Carrapateena. Additionally, REEs, other critical minerals (e.g. Sb, Bi, C, Co, W, Se, Te) plus F, S, As, Fe, Mo, Pb, Sn, Y, Zn are present at concentrations greater than mean continental crust. Other IOCGs (Fe-oxide Cu-Au) occur within a radius of ~150 km from Olympic Dam, which broadly defines the Olympic Cu-Au Province. These mineralised occurrences include, but are not limited to, Acropolis, Wirrda Well, Island Dam, Oak Dam East, Vulcan, Titan, Emmie Bluff, and the recently discovered Oak Dam West. Like any other global ore deposit type, IOCGs in the Olympic Cu-Au Province display similarities (e.g. hydrothermal magnetite/ hematite, hematite ages, U-Mo-Sn-W enriched hematite, Cu(±Fe) sulfides) and differences (e.g. host lithologies with different ages, nanoprecipitates/inclusions preserved in Fe-oxides, mineralization styles and depths of post-mineral cover). Simple down-drillhole magnetic susceptibility and total Fe concentration profiles reveal some of the complexities of these deposits. However, when coupled with micro- to nanoscale mineralogical characterisation, the macroscale trends can be articulated in terms of systematic transitions from magmatic magnetite to hydrothermal magnetite and finally to multi-generations of hematite.

1 Introduction

Hematite and magnetite are ubiquitous minerals in IOCG deposits, recording repeated cycles of replacement, remobilization and recrystallization from magmatic to hydrothermal conditions. A volume of research has been published focussed on the macro- to nanoscale Fe-oxide mineralogy and overall geochemical trends at Olympic Dam (OD), Wirrda Well (WW), Acropolis (AC), and Island Dam (ID). See detailed references in Ciobanu et al. (2019) and Cook et al. (2022). The present study shows magnetite susceptibility (*k*) values (i.e. proxy for magnetite abundance) and total Fe concentration, measured on 1-5m composite diamond drill core samples, to describe macro-scale magnetite and total Fe concentration at OD, WW, AC, ID and Oak Dam West (OKD). Published micro- to nanoscale mineralogical studies for OD, WW, AC, ID, and OKD are then used to clarify overall characteristics of the Olympic Dam Province IOCG deposits.

2 Geology and Mineralization Summary

Salient geology, sulfide mineralogy and geochronology data, mineralisation styles and geochemically anomalous element groups (see References section) for OD, WW, AC, ID and OKD are presented in Table 1.

	OD	WW	AC	ID	OKD
post-mineral cover thick (~m)	300-550	340-580	360-770	270-380	650-960
gravity anomaly	yes	yes	yes	yes	yes
magnetic anomaly	yes	yes	yes	yes	no
deposit host	HS	DS	GRV	WG	DS
host age (~Ma)	1590	1850	1590	1750	1850
other lithology	WG, BCF		DS, HS	DS	WG, GRV
mafic/UM dykes	GRV, GDS	TS, GDS		GDS	TS, GRV, GDS
mineral style	diss	diss	vein	skarn, lenses	diss
Cu±Fe sulfides	py-cp-bn-cc	py-cp, trace bn-cc	py-cp, trace bn-cc	py-cp, trace bn-cc	py-cp-bn-cc
anomal. whole-rock geochem	U-W-Sn-Mo	U-W-Sn-Mo	U-W-Sn-Mo	U-W-Sn-Mo	U-W-Sn-Mo
	HFSE, REE	HFSE, REE	HFSE, REE	HFSE, REE	HFSE, REE
	TM	TM	TM	TM	TM
dominant alteration	hydro	hydro	hydro	hydro	hydro
early alteration	alkali-calcic	alkali-calcic	alkali-calcic	alkali-calcic	alkali-calcic

Table 1. Geology, ages and sulfide mineralogy (refer to References section). Abbreviations are Donington Suite granitoids (DS, ~1850Ma), Tournefort Metadolerite Dykes (TS, ~1810Ma), Wallaroo Group metasediments and metavolcanics (WG, ~1750Ma), Hiltaba Suite Granitoids (HS, ~1590Ma), felsic, mafic, ultramafic Gawler Range Volcanics lavas and dykes (GRV, ~1590Ma), bedded clastic facies (BCF, ~1590Ma), Gairdner Dyke Swarm (GDS, ~830Ma), disseminated (diss), transition metals (TM = Zn, Mn, Co, Ni, Cr), hydrolytic alteration (hydro). References for 1) BCF is McPhie et al. 2016, 2) mafic and ultramafic dykes are Huang et al. 2015, 2016 and 3) anomalous whole-rock geochemistry trends, refer to Ehrig et al. 2012, Dmitrijeva et al. 2019a, 2019b, 2022.

3 Macroscale Magnetite-Hematite Variation

Down-hole magnetic susceptibility and Fe concentration profiles for OD (Figs 1A-B), WW (Fig 2A), ID (Fig 2B), AC (Fig 3A) and ODW (Fig 3B). As a rough guide, magnetic susceptibility (*k*) values of 0.1, 10, 100, 1000 x 10^{-3} SI units are approximately 0.025, 0.25, 2.5, 25 vol% magnetite (Clark and

Emerson, 1991). Scaling of *k* and Fe concentration axis are consistent between graphs for easy visualization of the trends.

k ranges for Olympic Dam sulfide mineralized granitic to hematite breccias are 0.25-2 x 10^{-3} SI (RD2852A, Fig 2A), very low magnetite content (Verdugo-Ihl et al. 2017). *k* values > 5 x 10^{-3} SI are anomalous and typically occur at depth and on the deposit margins (Fig 2B, RD2366), i.e. distal deposit margins with significant Fe-oxide addition (Verdugo-Ihl et al. 2020). RD2366 contains zones of magnetite-bearing hematite breccias below ~700m depth and a few isolated narrow zones from 450-525m.

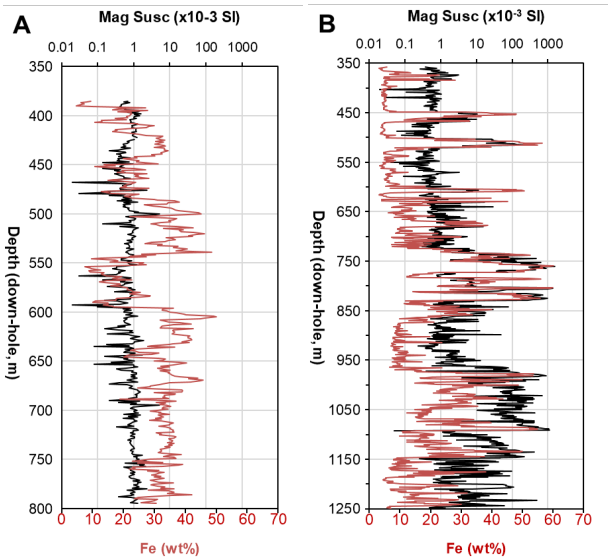

Figure 1. Magnetic susceptibility and Fe drill hole profiles for Olympic Dam A) RD2852A and B) RD2366.

k ranges for Wirrda Well sulfide mineralized granitic to hematite and magnetite-bearing hematite breccias (Fig 2A) are very similar to equivalent Olympic Dam breccias (Fig 1A-1B, respectively). However, significant short-scale variation in the WW Fe concentration reflects relatively narrow thickness, yet high frequency, of the Fe-oxide breccias within granitic breccias. Magnetite-bearing hematite breccias are dominant below 900m depth.

Island Dam Fe-oxides (Fig 2B, relatively low total %Fe) occur in skarn-style altered Fe-oxide bearing Wallaroo Group metasediments (Keyser et al. 2022). Intense hematite alteration of GRV feldspar-phyric rhyolites dominates above ~920m depth (Fig 3A) at Acropolis. The mineralisation style changes to magnetite-apatite veins in less intensely altered rhyolites from ~920-1065m and fine-grained dacite below 1065m depth (Krneta et al. 2017, Courtney-Davies et al. 2019, McPhie et al. 2020, Verdugo-Ihl et al. 2021).

A distinct magnetic anomaly is not present at Oak Dam West (Davidson et al. 2007, Oliveira 2012). This is different to the other IOCG deposits which are typified by spatial coincident gravity and magnetic anomalies. However, very low concentrations of magnetite are present (Fig 3B). Copper-barren (~680-1050m) and sulfide-bearing (~1050-1415m) hematite breccias occur in the profile, with altered Donington granitoids below 1450m (Fig 4A) (BHP 2019). The total REE+Y oxide (TREO) concentration is typically >1000 ppm in hematite breccias (Fig 4B). Felsic GRV dykes intersect the hematite breccias and deformed/altered granites in multiple locations.

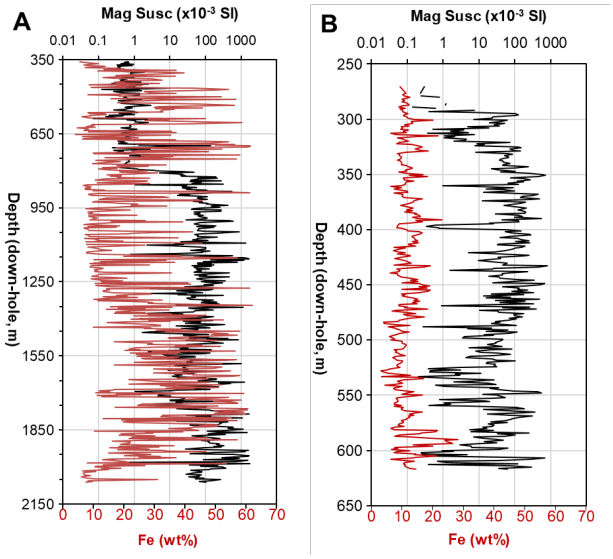

Figure 2. Magnetic susceptibility and Fe drill hole profiles for A) Wirrda Well WRD33 and B) Island Dam IDD4W1.

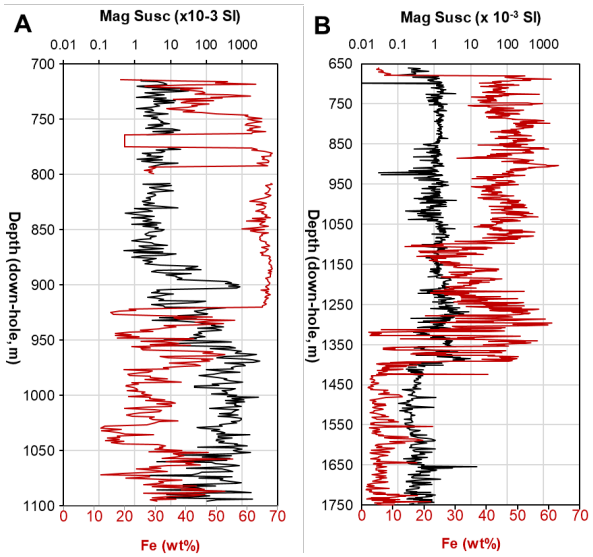

Figure 3. Magnetic susceptibility and Fe drill hole profiles for A) Acropolis ACD1 and B) Oak Dam West AD27W3.

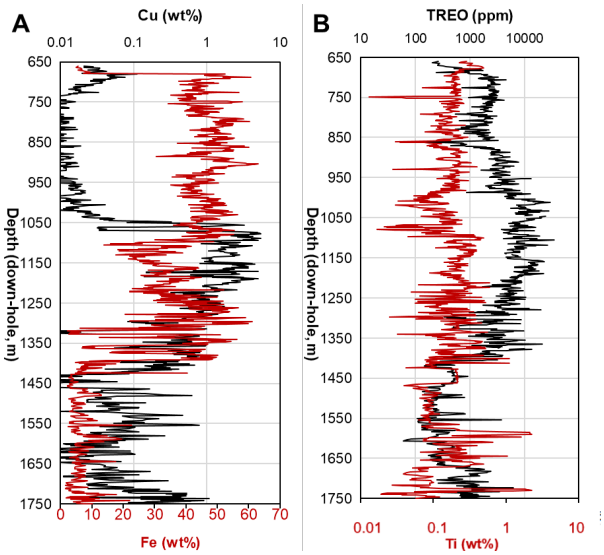

Figure 4. Cu, Fe (A) and TREO, Ti (B) profiles for Oak Dam West AD27W3.

4 Discussion and Implications

Essential attributes from Fe-oxide micro- to nanoscale studies across the Olympic Cu-Au Province are summarised in Table 2.

	OD	WW	AC	ID	OKD
mt of other origin (predating IOCG event)	U-bearing mt, older BIF	older metam. mt, fts incl., Si-Fe-nano-defects			?
silician mt <111> Si-Fe nanoscale defects, silicate nano-incl.	act, ep, ser	chl	no	yes (nano-scale work lacking)	?
titano-magnetite: trellis ilm, spinel incl. (herc, ulv, etc.)	preserved magmatic accessory from RDG	no	yes	no	no
hematite	yes	yes	yes	yes	yes
hem trace element signature	U-W-Sn-Mo	U-W-Sn-Mo	U-W-Sn-Mo	U-W-Sn-Mo	U-W-Sn-Mo
	Ti-V		Ti-V	Ti-V	
	Cu-As				

Table 2. Magnetite, hematite and alteration types summarized from previous micro- and nanoscale studies. Abbreviations: magnetite (mt), hematite (hem), banded iron formation (BIF), actinolite (act), epidote (ep), sericite (ser), chlorite (chl), ilmenite (ilm), hercynite (herc), ulvöspinel (ulv), ferrotschermakite (fts), hydrolytic alteration (hydro).

Iron-oxides were precipitated, replaced, or modified more or less continuously from the earliest stages of host rock alteration to the late, fluid-assisted overprinting events recorded throughout the province. Rock-buffered, coupled dissolution reprecipitation (CDRR)-driven reactions document a pervasive early alkali-calcic to late-stage hydrolytic alteration recognized across the Olympic Province (Krneta et al. 2017; Kontonikas-Charos et al. 2018, 2019).

In contrast to CDRR-driven alteration, fluid-buffered vein-filling at AC assists formation of high-temperature (~600 ºC) trellis titanomagnetite (Verdugo-Ihl et al. 2021). At OD, the alkali calcic stage is recorded within silician magnetite (Ciobanu et al. 2019; Verdugo-Ihl et al. 2020).

Alteration of host granites leads to release of Si, Al, Mg, and Ca, elements that assist formation of silician magnetite and associated (calc)-silicate inclusions also at WW and ID (Ciobanu et al. 2022; Keyser et al. 2022). The preservation of ferrotschermakite nanoinclusions within magnetite at WW (Ciobanu et al. 2022) are evidence for a pre-1590 Ma metamorphism of the otherwise altered country rock.

Interconversion between Fe-oxides, a phenomenon common to all deposits discussed here, contributes to enrichment in trace elements. Whilst the U-W-Sn-Mo signature is the most conspicuous (Courtney-Davies et al. 2019; Verdugo-Ihl et al. 2020; Keyser et al. 2022), the presence of up to hundreds of ppm REE and HFSE in iron-oxides is also noteworthy (Cook et al. 2022a, b). The U-Mo-W-Sn signature, although most pronounced in hematite formed during hydrolytic alteration, persists throughout the lifespan of the IOCG mineralizing system as OD (Verdugo-Ihl et al. 2017; Courtney-Davies et al., 2020).

Recognition of iron-oxides from older Fe-rich lithologies, including a ~1760 Ma uranium-bearing magnetite documented at OD (Courtney-Davies et al. 2020) provide new clues to interpret the spatial-temporal links between BIFs and IOCG mineralization in the Olympic Province, with broader implications for analogous terranes elsewhere.

Hematite geochemistry and U-Pb geochronology, explored beyond OD at WW, AC and ID, can resolve the genetic and temporal links among IOCG deposits in the Olympic Cu-Au Province (Courtney Davies et al. 2019; Keyser et al. 2022). Moreover, and as demonstrated by a study of Andean systems in Northern Chile (Verdugo-Ihl et al., 2022), iron-oxides are a powerful interpretive tool that will find broad application elsewhere.

Acknowledgements

We acknowledge Australian Research Council funding through LP130100438, LP200100156 and IH130200033, co-supported by BHP Olympic Dam, and by the FOX project funded by BHP Olympic Dam and the South Australian Government Mining and Petroleum Services Centre of Excellence.

References

BHP (2019) Operational Review for the quarter ended 30 September 2019 – Appendix. https://www.bhp.com/-/media/documents/media/reports-and-presentations/2019/191017_bhpoperationalreviewforthequarterended30september2019.pdf?la=en

Ciobanu, CL, Verdugo-Ihl MR, Slattery A, Cook NJ, Ehrig K,

Courtney-Davies L, Wade BJ (2019) Silician magnetite: Si-Fe-nanoprecipitates and other mineral inclusions in magnetite from the Olympic Dam deposit, South Australia. Minerals 9:311

Ciobanu CL, Verdugo-Ihl MR, Cook NJ, Ehrig K, Slattery A, Courtney-Davies L (2022) Ferro-tschermakite with polysomatic chain-width disorder identified in silician magnetite from Wirrda Well, South Australia: a HAADF STEM study. Am Mineral 107:765-777

Cherry A, Ehrig K, Kamenetsky VS, McPhie J, Kamenetsky M, Crowley J (2018) Precise geochronological constraints on the origin, setting and incorporation of ca. 1.59 Ga surficial facies into the Olympic Dam Breccia Complex, South Australia. Precambr Res, 315:162-178

Clark DH, Emerson DW (1991) Notes on rock magnetization characteristics in applied geophysical studies. Exploration Geophysics 22:547-555

Cook NJ, Ciobanu CL, Verdugo-Ihl MR, Courtney-Davies L, Ehrig K, Li W, Liu W, Xu J (2022a) Trace elements in minerals: where do we stand on the road between the Holy Grail and a can of worms? In: The Critical Role of Minerals in the Carbon-Neutral Future, Proc 16th SGA Biennial Meeting, Rotorua, New Zealand

Cook NJ, Ciobanu CL, Ehrig K, Slattery AD, Gilbert S (2022b) Micron- to atomic-scale investigation in iron oxides. Front Earth Sci 10:967189

Courtney-Davies L, Ciobanu CL, Verdugo-Ihl MR, Dmitrijeva M, Cook NJ, Ehrig K, Wade B (2019) Hematite geochemistry and geochronology resolve genetic and temporal links among iron-oxide copper gold systems, Olympic Dam district, South Australia. Precamb Res 334:105480

Courtney-Davies L, Ciobanu CL, Verdugo-Ihl MR, Cook NJ, Ehrig K, Wade B, Zhu Z, Kamenetsky VS (2020a) ~1760 Ma magnetite-bearing protoliths in the Olympic Dam deposit, South Australia: Implications for ore genesis and regional metallogeny. Ore Geol Rev 118:103337

Courtney-Davies L, Ciobanu CL, Tapster SR, Cook NJ, Ehrig K, Crowley JL, Verdugo-Ihl M, Wade BP, Condon DJ (2020b) Opening the magmatic-hydrothermal window: High precision U-Pb geochronology of the Mesoproterozoic Olympic Dam Cu-U-Au-Ag deposit, South Australia. Econ Geol 115-1855-1870

Davidson GJ, Paterson H, Meffre S, Berry RF (2007) Characteristics and Origin of the Oak Dam East Breccia-Hosted, Iron Oxide Cu-U-(Au) Deposit: Olympic Dam Region, Gawler Craton, South Australia. Econ Geol 102:1471-1498

Dmitrijeva M, Ehrig K, Ciobanu CL, Cook NJ, Verdugo-Ihl M, Metcalfe AV (2019a) Defining IOCG signatures through compositional data analysis: A case study of lithogeochemical zoning from the Olympic Dam deposit, South Australia. Ore Geol Rev 105:86-101

Dmitrijeva M, Ciobanu CL, Ehrig K, Cook NJ, Metcalfe A, Verdugo-Ihl M, McPhie J (2019b) Mineralization-alteration footprints in the Olympic Dam IOCG district, South Australia: The Acropolis prospect. J Geochem Explor 205:106333

Dmitrijeva M, Ciobanu CL, Ehrig K, Cook NJ, Verdugo-Ihl M, Metcalfe A, Kamenetsky VS, McPhie J (2022) Geochemical data analysis of iron-oxide copper gold mineralization, Wirrda Well prospect, South Australia. Econ Geol 117:853-874

Ehrig K, McPhie J, Kamenetsky VS (2012) Geology and mineralogical zonation of the Olympic Dam iron oxide Cu-U-Au-Ag Deposit, South Australia. In: Hedenquist JW, Harris M, Camus F (eds) Geology and Genesis of Major Copper Deposits and Districts of the World - A tribute to Richard H Sillitoe, SEG Spec Publ 16:237-268

Huang Q, Kamenetsky VS, McPhie J, Ehrig K, Meffre S, Maas R, Thompson J, Kamenetsky M, Chambefort I, Apukhtina O, Hu Y (2015) Neoproterozoic (ca. 820–830 Ma) mafic dykes at Olympic Dam, South Australia: Links with the Gairdner Large Igneous Province. Precambr Res 271:160–172.

Huang Q, Kamenetsky VS, Ehrig K, McPhie J, Kamenetsky M, Cross K, Meffre S, Agangi A, Chambefort I, Direen N G, Maas R Apukhtina O (2016) Olivine-phyric basalt at the Olympic Dam iron oxide Cu-U-Au-Ag deposit: insights into the mantle source and petrogenesis of the Gawler Silicic Large Igneous Province, South Australia: Precambr Res, 281:185-199

Keyser W, Ciobanu CL, Ehrig K, Dmitrijeva M, Wade BP, Courtney-Davies L, Cook NJ (2022) Skarn-style alteration in Proterozoic metasedimentary protoliths hosting IOCG mineralization: the Island Dam Prospect, South Australia. Miner Deposita 57:1227-1250

Kontonikas-Charos A, Ciobanu CL, Cook NJ, Ehrig K, Krneta S, Kamenetsky VS (2018) Rare earth element geochemistry of feldspars: Examples from Fe-oxide Cu-Au systems in the Olympic Cu-Au Province, South Australia. Mineral Petrol 112:145-172

Kontonikas-Charos A, Ehrig K, Cook NJ, Ciobanu CL (2019) Crystal chemistry of titanite from the Roxby Downs Granite, South Australia: Insights into petrogenesis, subsolidus evolution and hydrothermal alteration. Contrib Mineral Petrol, 174:59

Krneta, S, Cook, NJ, Ciobanu, CL, Ehrig, K and Kontonikas-Charos, A (2017) The Wirrda Well and Acropolis prospects, Gawler Craton, South Australia: Insights into evolving fluid conditions through apatite chemistry. J Geochem Explor 181:276-291

McPhie J, Orth K, Kamenetsky V, Kamenetsky M and Ehrig K (2016) Characteristics, origin and significance of Mesoproterozoic bedded clastic facies at the Olympic Dam Cu-U-Au-Ag deposit, South Australia. Precambr Res 276: 85-100

McPhie J, Ehrig K, Kamenetsky M, Crowley J, Kamenetsky VS (2020) Geology of the Acropolis prospect, South Australia, constrained by high-precision CA-IDTIMS ages. Austr J Earth Sci 67:699-716

Oliveira T (2021) Oak Dam Update: South Australian Exploration and Mining Conference, 26 November 2021, Adelaide

Verdugo-Ihl M, Ciobanu CL, Cook NJ, Ehrig K, Courtney-Davies L, Gilbert S (2017) Textures and U-W-Sn-Mo signatures in hematite from the Olympic Dam Cu-U-Au-Ag deposit, South Australia: defining the archetype for IOCG deposits. Ore Geol Rev 91:173-195

Verdugo-Ihl MR, Ciobanu CL, Slattery A, Cook NJ, Ehrig K, Courtney-Davies L (2019) Copper-arsenic nanoparticles in hematite: Fingerprinting fluid-mineral interaction. Minerals 9: 388.

Verdugo-Ihl M, Ciobanu CL, Cook NJ, Ehrig, K, Courtney-Davies L (2020) Defining early stages of IOCG systems: evidence from iron-oxides in the outer shell of the Olympic Dam deposit, South Australia. Miner Deposita 55:429-452

Verdugo-Ihl, MR, Ciobanu CL, Cook NJ, Ehrig K, Slattery A, Courtney-Davies L, Dmitrijeva M (2021) Nanomineralogy of hydrothermal magnetite from Acropolis, South Australia: Genetic implications for iron-oxide copper gold mineralization: Am Mineral 106:1273-1293

Verdugo-Ihl MR, Ciobanu CL, Courtney-Davies L, Cook NJ, Slattery A, Ehrig K, Tornos F, Hanchar JM (2022) U-Pb geochronology and mineralogy of hematite from Mantoverde and Carmen de Cobre, Northern Chile: Constraints on Andean IOCG mineralization. Econ Geol 117:943-960

Apatite and REE in iron oxide-apatite (IOA) deposits

Daniel E. Harlov[1]
[1]Deutsche GeoForschungsZentrum GFZ, Telegrafenberg, Potsdam 14473, Germany

Iron oxide-apatite (IOA) deposits world-wide are commonly exploited for their iron ore. However, their potential as REE ore deposits has neither been explored nor exploited. Over the last 20 or more years a number of studies have been made specifically focussing on the presence of REE in IOA deposits (Harlov et al. 2002, 2016; Taghipour et al. 2015; Jonsson et al. 2016; Normandeau et al. 2018; Maraszewska et al. 2023; Yin et al. 2023).

The primary host for REE in IOA deposits is fluorapatite, which, when metasomatically altered, results in the formation of monazite, xenotime, allanite, REE-carbonates, and REE-fluorides as secondary REE-bearing minerals (cf. Harlov 2015). Metasomatic alteration of the fluorapatite occurs by a coupled dissolution-reprecipitation process (Putnis 2002, 2009) such that the REE are liberated to form the above minerals either as inclusions in or rim grains associated with the fluorapatite.

In a number of IOA deposits, dating of monazite inclusions in fluorapatite or monazite associated with fluorapatite, using EPMA, LA-ICP-MS, and/or SHRIMP, have demonstrated that the monazite formed right after or even during the genesis and mineralization of the IOA ore body. Examples include Pea Ridge, SE Missouri, USA (Harlov et al. 2016; Neymark et al. 2016), Chogart, Bafq region, central Iran (Torab and Lehmann 2007; Stosch et al. 2011), or Heiyingshan, Beishan Metallogenic Belt, NW China (Yin et al. 2023).

Additional remobilization of REE due to further fluid infiltration, coupled with tectonic reworking, results in the remobilization of these REE-bearing minerals such that they become intergrown with magnetite, hematite, and silicate minerals in the IOA ore deposit or are redeposited in surrounding country rock that is in direct contact with the IOA ore deposit.

The REE content in IOA deposits world-wide is extremely variable ranging from IOA deposits that are quite enriched in REE, such as Pea Ridge, SE Missouri, USA (Harlov et al. 2016), to the IOA ore bodies of the middle to lower Yangtze River metallogenic belt (MLYRMB), east central China, which are relatively depleted in REE (Hu et al. 2020).

This broad variability in the REE content among different IOA ore bodies appears to be linked to the mechanism(s) involved behind their formation and the sources of Fe, P, Ca, REE, F, etc exploited during this formation. IOA deposits are associated with sub-volcanic intrusions and volcanic terranes in general. These volcanic terranes in turn are generally associated with subduction zone environments in the case of IOA deposits dating from the late Proterozoic to the late Cenozoic. However, the genesis and evolution of IOA deposits is still somewhat controversial fluctuating between an igneous vs. a metasomatic origin.

Recently Hu et al. (2020), building on the work of Knipping et al. (2015a,b) and others, has proposed a dual magmatic-metasomatic origin, which takes into account the close physical and temporal relationship in the MLYRMB between IOA deposits, associated subvolcanic diorite porphyry intrusions, and local iron skarns in what was originally a subduction zone environment during the collision between the Yangtze craton and the North China craton at around 130-132 Ma.

In such a scenario, genesis of the diorite porphyry intrusions began as a complex melting event in the enriched mantle wedge above the subducting oceanic plate associated with the collision. These melts then rose and ponded at the crust-mantle boundary from which a diorite porphyry diapir differentiated and ascended due to its buoyancy. The mechanisms associated with this genesis would suggest that the diorite porphyry diapir would have had an NaCl-H_2O component derived ultimately from fluids/melts originating from the subducting oceanic plate.

While presumed to be a one phase melt at the crust-mantle boundary, as this diapir rises upwards into the crust, and lower pressures, it is assumed that there would be a separation of the melt into a diorite porphyry magma and a NaCl-rich fluid or perhaps NaCl-melt of sorts with an H_2O component. This NaCl-rich fluid is then presumed to act as a scavenger for Fe, P, Ca, and F from the diorite porphyry melt, along with various trace elements such as the REE, since all of these elements can complex as chlorides. The affinity of REE as both chloride and fluoride complexes at high temperatures and pressures (800 °C, 1000 MPa) is well known from the NaCl-, KCl-, and NaF-bearing solubility experiments of Tropper et al. (2011, 2013) and Mair et al. (2017).

Due to their lower density, these NaCl-rich fluids would rise to the top of the diapir. Upon being emplaced into the upper crust a kilometer or two below the surface as part of a volcanic system, the high temperature (900–1000 °C) NaCl-rich fluid at the top of the magma chamber would then be injected into the fractured country rock by the interaction between the diapir and deep-seated meteoric waters. This injected NaCl-rich fluid, along with the various elements inherent to it as chlorides, is the progenitor of the IOA deposit with the Fe, P, Ca, F, etc. crystallizing out as magnetite and fluorapatite plus minor amounts of silicate minerals such as pyroxenes and amphiboles. The NaCl would have been removed from the IOA deposit via deep seated circulating meteoric waters causing the

surrounding country rocks to be albitized in the form of a contact aureole. Further migration and dilution of these cooling NaCl-rich fluids further up along the fractured rock column and their chemical interaction with the surrounding rocks would then have resulted in the formation of associated iron skarns.

Evidence for NaCl-rich fluids/salt melts associated with IOA deposits has been documented in NaCl melt inclusions from both fluorapatite and pyroxene in a variety of IOA deposits including El Laco in Chile (Broman et al. 1999) and IOA deposits of the MLYRMB, central eastern China (Li et al. 2015). In addition, many IOA deposits such as those in the MLYRMB (Hu et al. 2020), Great Bear magmatic zone, Slave Craton, north-western Canada (Normandeau et al. 2018), and Bafq, central Iran (Taghipour et al. 2015) are characterized by albitization of the country rock surrounding the IOA deposit.

If this scenario regarding IOA deposit formation is correct, then the REE content of an IOA deposit is dependent first on the magma source of the original one phase melt, originating in the mantle wedge and ponding at the crust mantle boundary, and secondly on the ability of Cl to scavenge REE from the melt as chloride complexes and subsequently incorporate them into the NaCl-rich fluid/melt during phase separation from the diorite porphyry melt. Assuming that the mechanism behind the phase separation of melts and scavenging of elements from the melt by an NaCl-dominated fluid are basically the same for all IOA deposits, the high variability in REE content seen between different IOA ore deposits, which appears to be independent of their age, would suggest that the source area of the IOA deposit is responsible for this variability in REE content. That is for REE-poor IOA deposits, the source of the melts responsible for the deposit was poor in REE whereas for REE-rich deposits, the source was rich in REE. It is also possible in such a scenario that during its migration upwards from the crust mantle-boundary the melt might have encountered REE-enriched regions or deposits such as carbonatites or been relatively more efficient at scavenging REE's from the lower crust as it passed through due to the particular nature of its whole rock and fluid chemistry.

In order to confirm this hypothesis, experiments at 900 – 1000 °C and 200 - 1000 MPa involving simple Fe-, P-, Ca-, and F-bearing granitoid melts with an NaCl-H_2O melt component that were seeded with one or two REE, such as Ce and Y, as proxies would need to be performed in order to see if, along with Fe, P, Ca, and F, the REE would be naturally partitioned into a separate NaCl-H_2O melt allowing for magnetite and fluorapatite to crystallize out separate from the granitoid melt in the capsule as the capsule is slowly cooled from 900 – 1000 °C to 500 – 600 °C over a period of days.

References

Broman C, Nyström JO, Henriquez F, Elfman, M (1999) Fluid inclusions in magnetite-fluorapatite ore from a cooling magmatic system at El Laco, Chile; Geol Fören Stockholm Förhand 121:253–267

Harlov DE, Andersson UB, Förster H-J, Nyström JO, Dulski P, Broman, C (2002) Apatite–monazite relations in the Kiirunavaara magnetite–apatite ore, northern Sweden Chem Geol 191:47-72

Harlov DE, Meighan CJ, Kerr ID, Samson IM (2016) Mineralogy, chemistry, and fluid-aided evolution of the Pea Ridge Fe oxide-(Y + REE) deposit, southeast Missouri, USA. Econ Geol 111:1963-1984

Harlov DE (2015) Apatite: a fingerprint for metasomatic processes. Elements 11:171-176

Hu H, Li J-W, Harlov DE, Lentz DE, McFarlane RM, Yang, Y-H (2020) A genetic link between iron oxide-apatite and iron skarn mineralization in the Jinniu volcanic basin, Daye district, eastern China: evidence from magnetite geochemistry and multi-mineral U-Pb geochronology. Geol Soc Am Bull, https://doi.org/10.1130/B35180.1

Jonsson E, Harlov DE, Majka J, Högdahl K, Persson-Nilsson K (2016) Fluorapatite-monazite-allanite relations in the Grängesberg apatite-iron oxide ore district, Bergslagen, Sweden. Am Mineral 101:1769-1782

Knipping JL, Bilenker LD, Simon AC, Reich M, Barra F, Deditius AP, Lundstrom C, Bindeman I, Munizaga R (2015a) Giant Kiruna-type deposits form by efficient flotation of magmatic magnetite suspensions. Geology 43: 591-594

Knipping JL, Bilenker LD, Simon AC, Reich M, Barra F, Deditius AP, Wälle M, Heinrich CA, Holtz F, Munizaga R (2015b) Trace elements in magnetite from massive iron oxide-apatite deposits indicate a combined formation by igneous and magmatic-hydrothermal processes. Geochim Cosmochim Acta 171:15-38

Li W, Audétat A, Zhang J (2015) The role of evaporates in the formation of magnetite-apatite deposits along the Middle and Lower Yangtze River, China: evidence from LA-ICP-MS analysis of fluid inclusions. Ore Geol Rev 67:264-278

Mair P, Tropper P, Harlov DE, Manning CE (2017) The solubility of $CePO_4$ monazite and YPO_4 xenotime in KCl-H_2O fluids at 800 °C and 1.0 GPa: implications for REE transport in high-grade crustal fluids. Am Mineral 102: 2457-2466

Maraszewska M, Majka J, Harlov DE, Manecki M, Schneider DA, Broska I, Myhre P-I (2023) Multi-stage metamorphic and metasomatic imprints on apatite-monazite-xenotime assemblages in a set of small iron oxide-apatite (IOA) ore bodies, Prins Karls Forland, Svalbard. Ore Geol Rev 155: 105344

Neymark L A, Holm-Denoma CS, Pietruszka A, Aleinikoff JN, Fanning, C. M., Pillers, R. M., Moscati, R. J. (2016) High spatial resolution U-Pb geochronology and Pb isotope geochemistry of magnetite-apatite ore from the Pea Ridge iron oxide-apatite deposit, St. Francois Mountains, southeast Missouri, USA. Econ Geol 111:1915-1933

Normandeau PX, Harlov DE, Corriveau L, Paquette J, McMartin I (2018) Characterization of fluorapatite within iron oxide alkali-calcic alteration systems of the Great Bear magmatic zone: a potential metasomatic process record. Can Mineral 56:167-187

Putnis A (2002) Mineral replacement reactions: from macroscopic observations to microscopic mechanisms. Mineral Mag 66:689-708

Putnis A, (2009) Mineral replacement reactions: thermodynamics and kinetics of water-rock interaction; Rev Mineral Geochem 70:87-124

Stosch H-G, Romer RL, Daliran F, Rhede D (2011) Uranium–lead ages of apatite from iron oxide ores of the Bafq District, East-Central Iran. Mineral Dep 46:9-21

Taghipour S, Kananian A, Harlov D, Oberhänsli R (2015) Kiruna-type iron oxide-apatite deposits, Bafq district, central Iran: fluid-aided genesis of fluorapatite-monazite-xenotime assemblages. Can Mineral 53:479-496

Torab F, Lehmann B (2007) Magnetite-apatite deposits of the Bafq district, central Iran: apatite geochemistry and monazite geochronology. Mineral Mag 71:347-363

Tropper P, Manning CE, Harlov DE (2011) Solubility of $CePO_4$ monazite and YPO_4 xenotime in H_2O and H_2O–NaCl at 800 °C and 1 GPa: implications for REE and Y transport during high-grade metamorphism. Chem Geol 282:58-66

Tropper P, Manning CE, Harlov DE (2013) Experimental determination of $CePO_4$ and YPO_4 solubilities in H_2O–NaF at 800 °C and 1 GPa: implications for rare earth element transport in high-grade metamorphic fluids. Geofluids 13: 372-380.

Yin Y, Li J-W, Harlov D, Pan Z-J, Hu H (2023) Timing of fluid-induced alteration of fluorapatite in iron oxide–apatite deposits: Insights from monazite U–Pb geochronology of the Heiyingshan IOA deposit, Beishan Metallogenic Belt, Northwest China; Ore Geology Reviews (submitted).

Fe-O isotope systematics and magnetite chemistry of the Malmberget iron-oxide apatite deposit, Sweden

Jens S Henriksson[1,2], Valentin R Troll[1], Ellen Kooijman[3], Ilya Bindeman[4]
[1]Exploration Department, Luossavaara Kiirunavaara Aktiebolag, Sweden
[2]Department of Earth Sciences, Uppsala University, Sweden
[3]Department of Geosciences, Swedish Museum of Natural History, Stockholm, Sweden
[4]Department of Earth Sciences, University of Oregon, Eugene, USA

Abstract. Fe-O isotopes from drill core samples and whole rock chemistry from massive magnetite in LKAB's geochemical database have been used to unravel the origin, affinity, and stratigraphic position of the ore bodies in the Malmberget iron-oxide apatite deposit. Fe-O isotopes suggest a magmatic to magmatic-hydrothermal origin of the Malmberget deposit. Seven distinct magnetite populations have been identified using a novel Fe/V versus V/Ti magnetite discrimination diagram. Six of the magnetite populations form distinct spatio-geochemical clusters, whereas the massive magnetite data from the Fabian-Kapten ore body are scattered. Aggregated, this can be explained by a system where separate events form chemically distinct sill-type apatite-iron oxide intrusions within the volcano-sedimentary package, and repeated eruptions form a chemically scattered ore package on top.

1 Introduction

The Malmberget iron-oxide apatite (IOA) deposit, located in northern Sweden (671148°N, 204101°E), is the second largest underground iron mine in the world. Current annual production amounts to 19 Mt at 39.4 Fe wt.%, with total mineral resources, excluding reserves, estimated to 981 Mt at 53.8 Fe wt.%. The formation of giant-sized IOA deposits remains ambiguous and is surrounded by intense scientific debate (c.f. Geijer 1910; Parák 1975; Hildebrand 1986; Hitzman et al. 1992; Jonsson et al. 2013; Dare et al. 2015; Knipping et al. 2015; Bilenker et al. 2016; Tornos et al. 2016; Simon et al. 2018; Troll et al. 2019). Recent stable isotope thermometry studies on global IOA deposits predominately suggest a high-temperature (high-T) origin (>800 °C), where the chemically inert and refractory massive magnetite buffers the system with regards to post-depositional reequilibration of the Fe-O composition and low-T hydrothermal features are attributed to a progressively cooling magmatic system (e.g. Jonsson et al. 2013; Bilenker et al. 2016; Troll et al. 2019). Aside from two poorly constrained oxygen isotope values (Lund 2014), no Fe-O isotope data have previously been reported for the Malmberget deposit.

The trace element composition of magnetite chemistry has previously been used to classify magnetite from different ore-forming environments (e.g. Dupuis and Beaudoin 2011; Dare et al 2014; Nadoll et al. 2014), but also to identify deposit-scale chemical differences (Ovalle et al. 2018). Wen et al. 2017 questioned the applicability of these discriminatory diagrams for genetic interpretation, especially for reequilibrated magnetite.

In this contribution, we use Fe-O isotopes and whole rock geochemical data from massive magnetite to: (1) Investigate the Fe-O isotopes of the Malmberget magnetite to constrain the ore-source and compare the Fe-O isotope signatures to those of global IOA ore deposits; and (2) characterise magnetite chemistry to identify affinities and discrepancies between the geometrically complex ore bodies in the Malmberget deposit.

1.1 Geological background

The Malmberget area occupies the southernmost part of the Paleoproterozoic northern Norrbotten ore province and comprises over twenty historically defined ore bodies that are hosted in a package of mafic to felsic metavolcanics (Figure 1). Age constraints from U-Pb dating of oscillatory zoned zircons from the metavolcanic host rocks yield magmatic ages between 1.89 and 1.87 Ga and metamorphic ages between 1.80 and 1.77 Ga, where the later age coincides with the emplacement of the minimum melt Lina-type granite-pegmatite suite (Sarlus et al. 2018; Sarlus et al. 2020). Further U-Pb dating of zircons from the Kiirunavaara ore constrains IOA deposit formation in the region between 1.88 and 1.87 Ga (Westhues et al. 2016).

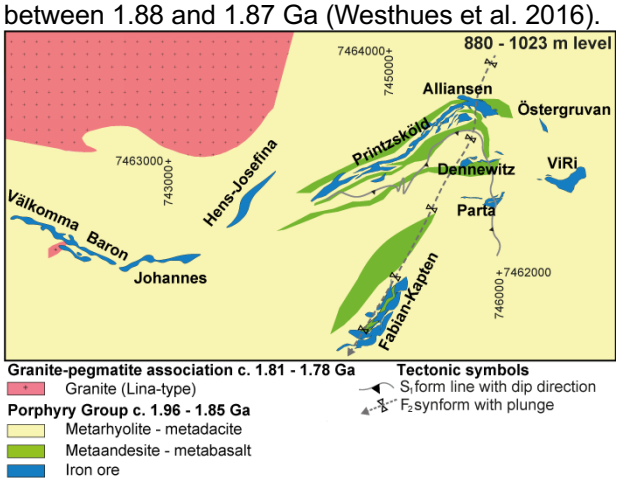

Figure 1. Simplified geological map of the Malmberget IOA deposit at the 880-1023 m level below surface.

The geology of the Malmberget area is characterised by multiple events of alteration, deformation and metamorphism that have overprinted primary textures and features of both host rock and ore, as well as transpositioned the originally continuous, bedding parallel ore-bearing volcano-sedimentary package (Geijer 1930;

Martinsson et al. 2016; Bauer et al. 2018). Consequently, the affinity and stratigraphic position of the individual ore bodies is complex and remains unclear. Lund (2013) suggested that the Malmberget ore is hosted in three different stratigraphic positions, where Fabian-Kapten (FA-KA) and Vitåfors-Ridderstolpe (ViRi) ore bodies sit at the lowest position, Printzsköld-Alliansen (PR-AL) at the middle position, and the Välkomma (VA), Baron (BA), Johannes (JH) and Hens-Josefina (HN-JS), collectively referred to as the Western Field (WF), at the highest position. On the contrary, Bauer et al. (2018) interpreted at least two stratigraphic positions of the ore from structural data, suggesting that the stratigraphically lower ore position forms a ca. 5 km semi-continuous ore zone, from the WF through PR-AL to Östergruvan (ÖG), Dennewitz (DE), Parta (PA) and ViRi in the east. The stratigraphically upper ore position comprises the FA-KA ore body and is situated in the hinge of the Malmberget synform. Work on the Malmberget stratigraphy (Allen 2022) interprets at least five stratigraphic positions for the ore, from the lowest position to the highest position: WF, PR-AL, DE, PA, and FA-KA.

2 Methodology

For Fe-O isotope analysis, we collected massive magnetite samples along two drill cores transecting the FA-KA (n=5) and the ViRi (n=1) ore bodies at depths of -1550 m and -1220 m, respectively. The magnetite samples were crushed, magnetically separated, and inspected to ensure purity at Uppsala University.

Oxygen isotopes were analysed at the University of Oregon following the procedures of Bindeman et al. (2022), using a MAT 253 gas isotope ratio mass spectrometer with a fluorination line attached, in dual inlet mode, and using BrF_5 as a reagent. An in-house Gore Mountain garnet standard (+6.52‰) was used for calibration before and after sample analysis. Oxygen isotope values are reported relative to SMOW.

Iron isotope analysis was conducted at the Vegacenter at the Swedish Museum of Natural History in Stockholm. Digestion and purification of the crystals was achieved in HF, HNO_3 and 10 M HCl acid following the procedures of Borrok et al. (2007) and Millet et al. (2012). Before analysis, each sample was diluted with 0.3 M HNO_3 to a concentration of 2–3 ppm. The instrument used for Fe isotope analyses was a Nu Plasma II HR-MC-ICP-MS in pseudo-high-resolution mode. All values were corrected for mass bias and are reported relative to IRMM-014 from Isotopic Reference Materials and Measurements (Brand et al. 2014).

Literature magnetite Fe-O isotopes from global IOA ore deposits, combined with Fe-O isotopes from volcanic, igneous, low-T hydrothermal and hydrothermal replacement magnetite have been used to establish reference fields for the Fe-O data.

Whole rock assays from 63 480 drill core samples have been queried for massive magnetite from LKAB's geochemical database using the following parameters: Fe > 65.00 wt.%, magnetite/hematite > 10.00, and P_2O_5 < 0.25 wt.%, with a total of 1964 samples fitting the established criteria. All samples have been analysed by ALS Laboratories or MSALABS for ferrous iron by titration and for whole rock chemistry using a lithium metaborate/tetraborate fusion with XRF finish.

Clusters were identified in geochemical plots of the massive magnetite were evaluated based on their spatio-geochemical relationships.

3 Fe-O isotopes

The Malmberget magnetite samples plot within the range of common igneous magnetite (1‰ < $\delta^{18}O$ < 4‰ and 0.05‰ < $\delta^{56}Fe$ < 0.9‰), despite the observed equilibrated textures in (Geijer 1930), reflecting the original, magmatic origin of the Malmberget deposit (Figure 2). In addition, all the Malmberget samples plot within the field of the Kiruna deposit established in Troll et al. (2019) and emphasise the similarities of the two deposits.

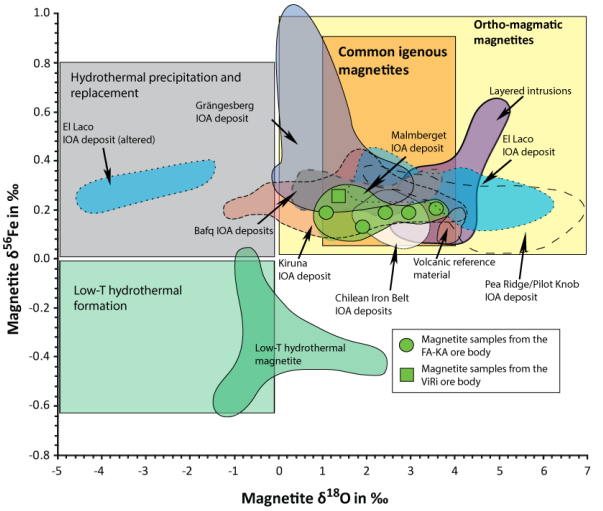

Figure 2. Discriminatory diagram for magnetite based on $\delta^{18}O$-values and $\delta^{56}Fe$-values. The coloured fields correspond to the distribution of values reported in Troll et al. (2019) and Xie et al. (2021).

Equilibrium calculations (Table 1) have been conducted to evaluate the potential magnetite source(s). Potential sources include basaltic to dacitic magmas (900°C) and magmatically derived high-T fluids (800°C). For $\delta^{18}O$-values, three samples are in equilibrium with a basaltic source, five samples with an andesitic source, five samples with a dacitic source, and all six samples with a high-T fluid source. All samples have $\delta^{56}Fe$-values in equilibrium with a magma source, whereas all samples except ViRi-01 are in equilibrium with a high-T fluid source. Thus, uniform equilibrium for the FA-KA magnetite is exclusively attained with a high-T fluid source, whereas the ViRi magnetite is in equilibrium with a dacitic to andesitic magma.

Table 1. Results for the magnetite-magma (900°C) and magnetite-magmatic fluid (800°C) equilibrium calculation.

Sample	$\delta^{18}O$	2σ	$\delta^{56}Fe$	2σ	$\delta^{18}O$ Basalt	$\delta^{18}O$ Andesite	$\delta^{18}O$ Dacite	$\delta^{18}O$ Fluid	$\delta^{56}Fe$ Magma	$\delta^{56}Fe$ Fluid	Formation Temp.
FA-001	2.0	±0.2	0.16	0.07	5.4	**6.0**	**6.3**	**7.2**	**0.13**	**-0.08**	≥ 800°C
FA-003	1.1	±0.2	0.18	0.07	4.5	5.1	5.4	**6.3**	**0.15**	**-0.06**	≥ 800°C
FA-004	3.7	±0.2	0.19	0.07	**7.1**	**7.7**	**8.0**	**8.9**	**0.16**	**-0.05**	≥ 800°C
FA-005	2.5	±0.2	0.18	0.07	**5.9**	**6.5**	**6.8**	**7.7**	**0.15**	**-0.06**	≥ 800°C
FA-006	3.2	±0.2	0.18	0.08	**6.6**	**7.2**	**7.5**	**8.4**	**0.15**	**-0.06**	≥ 800°C
ViRi-01	1.7	±0.2	0.25	0.07	5.1	**5.7**	**6.0**	**6.9**	**0.22**	0.01	> 800°C

Bold=in equilibrium. **Oxygen**: 1000lnα mt - (basalt) or (andesite) or (dacite) or (magmatic water 800°C) = (-3.4 ‰), (-4.0‰), (-4.3‰), (-5.2‰); range of basalts, arc andesites/dacites +5.7‰ to +8.0‰ (Taylor 1968; Bindeman et al. 2022); range of high-T magmatic fluids 5-10 ‰ (Zheng 1991; Hoefs 1997). **Iron**: 1000lnα mt - (magma) or (magmatic water 800°C) = (0.03 ‰), (0.24 ‰); range for arc andesites/dacites +0.00 to +0.12 ‰ (Heimann et al. 2008); range for high-T magmatic fluids 0.00 to -0.35 ‰ (Heimann et al. 2008; Severmann and Anbar 2009).

The observed magnetite-source dissimilarity between the ViRi and FA-KA ore bodies supports the interpretation of Bauer et al. (2018) and Allen (2022), where ViRi sits in a structurally lower position, more proximal to the magmatic centre of the ore-forming system.

4 Whole rock magnetite geochemistry

The massive magnetite, queried from LKAB's geochemical database, has been colour-coded by ore body and plotted on Ti+V vs Al+Mn, Fe vs V/Ti and Fe/V vs V/Ti magnetite discrimination diagrams (Figures 3a-f; Dupuis and Beaudoin 2011; Wen et al. 2017; this study).

In all three geochemical plots (Figure 3a,c,e), the FA-KA ore is comparatively scattered to the massive magnetite from the other ore bodies. The scattering of the FA-KA data agrees with the chemically distinct sub-units described for FA-KA in Lund (2013).

The massive magnetite from PR-AL has V/Ti ratios >1, which is indicative of hydrothermal magnetite (Dupuis and Beaudoin 2011). The hydrothermal character of PR-AL is possibly related to the D_1 shear-zone described in Bauer et al. (2018), where the shear-zone acted as a conduit for the hydrothermal fluids that may have remobilised the mobile elements (i.e. vanadium).

In the Ti+V vs Al+Mn plots (Figures 3a,b) four spatio-geochemical clusters have been identified: FA-KA, PR-AL, WF, and DE-PA-PR-ViRi-ÖG. Spatio-geochemical clusters cannot be identified in the Fe vs V/Ti plot (Figures 3c,d), however, the plots clearly display the reequilibration trend from magmatic magnetite to hydrothermal magnetite (Wen et al. 2017).

In Figures 3e,f we present a novel discriminatory diagram for magnetite. The diagram is a modification of the diagram in Wen et al (2017). Fe wt.% has been substituted for Fe/V to circumvent the increase in iron and vanadium contents coupled to iron and mobile trace element purification of magnetite by hydrothermal fluid induced reequilibration by magnetite-magnetite dissolution and reprecipitation (Wen et al. 2017). Five distinct spatio-geochemical clusters have been identified for the main ore bodies using the discriminatory diagram: FA-KA, PR-AL, WF, WF-HW, DE, and PA-ViRi-ÖG. Two additional clusters have been identified, one in the PR hanging wall (HW) and one in the WF hanging wall. The identified clusters agree with the stratigraphic interpretation of Allen (2022), and highlight the affinity of the isolated PA, ViRi and ÖG ore bodies in the eastern part of the deposit.

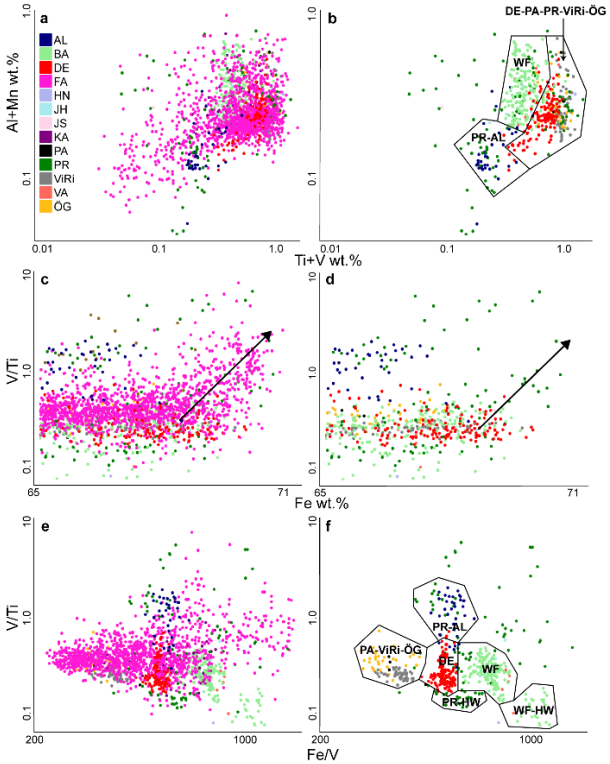

Figure 3. Magnetite chemistry plots (Dupuis and Beaudoin 2011; Wen et al. 2017). **a** Ti+V vs Al+Mn for all ore bodies and **b** for all ore bodies excluding FA-KA. **c** Fe vs V/Ti for all ore bodies and **d** for all ore bodies excluding FA-KA. The black arrow shows the trend of magnetite-magnetite reequilibration. **e** Fe/V vs V/Ti for all ore bodies and f) for all ore bodies excluding FA-KA. The fields in **b** and **f** outlines the identified spatio-geochemical clusters.

5 Conclusion

Combined, our data suggest that the Malmberget IOA deposit is primarily of magmatic to magmatic-hydrothermal origin and that the main ore bodies of the structurally complex deposit originally belonged to at least five spatio-geochemically distinct ores. All ore bodies, except FA-KA, are characterised by tightly clustered geochemical data. This discrepancy is likely related to the stratigraphic position of the ore bodies. We propose an ore-forming scenario for the Malmberget IOA deposit where coupled intrusive-extrusive events emplace chemically distinct sill-type

ore intrusions at different stratigraphic positions in the volcano-sedimentary package and simultaneously deposit the FA-KA ore at surface.

Acknowledgements

We thank Vetenskapsrådet (grant number 2020-03789) for funding this project.

References

Allen R (2022) Defining host-rocks stratigraphy and structure in order to explore for new ore lenses: Malmberget. LKAB Internal Report.

Bauer T, Andersson JBH, Sarlus Z, Lund C, Kearney T (2018) Structural Controls on the Setting, Shape, and Hydrothermal Alteration of the Malmberget Iron Oxide-Apatite Deposit, Northern Sweden. Economic Geology 133:377–395.

Bindeman IN, Ionov DA, Tollan PME, Golovin AV (2022) Oxygen isotope (δ18O, Δ′17O) insights into continental mantle evolution since the Archean. Nature Communications 13:3779.

Bilenker LD, Simon AC, Reich M, Lundstrom CC. Gajos N, Bindeman I, Barra F, Munizaga, R (2016) Fe–O stable isotope pairs elucidate a high-temperature origin of Chilean iron oxide-apatite deposits. Geochimica et Cosmochimica Acta 177:94–104.

Brand WA, Coplen TB, Vogl J, Rosner M, Prohaska T (2014) Assessment of international reference materials for isotope-ratio analysis (IUPAC Technical Report). Pure and Applied Chemistry 86:425–467.

Borrok DM, Wanty RB, Ridley WI, Wolf R, Lamothe PJ, Adams M (2007) Separation of copper, iron, and zinc from complex aqueous solutions for isotopic measurement. Chemical Geology 242:400–414.

Dare SAS, Barnes S, Beaudoin G (2015) Did the massive magnetite "lava flows" of El Laco (Chile) form by magmatic or hydrothermal processes? New constraints from magnetite composition by LA-ICP-MS. Mineralium Deposita 50:607–617.

Geijer P (1910) Igneous rocks and iron ores of Kiirunavaara, Luossavaara and Tuollavaara. Scientific and Practical Researches in Lapland arranged by the Luossavaara-Kiirunavaara Aktiebolag. Geology of the Kiruna district 2, Stockholm: 278 p.

Geijer P (1930) Gällivare malmfält: geologisk beskrivning. Sveriges Geologiska Undersokning C 22: 115 p

Hildebrand R.S (1986) Kiruna-type deposits; their origin and relationship to intermediate subvolcanic plutons in the Great Bear magmatic zone, Northwest Canada. Economic Geology 81:640–659.

Hitzman MW, Oreskes N, Einaudi MT (1992) Geological characteristics and tectonic setting of Proterozoic iron oxide (Cu-U-Au-REE) deposits. Precambrian Research 58:241–287.

Heimann A, Beard BL, Johnson CM (2008) The role of volatile exsolution and sub-solidus fluid/rock interactions in producing high 56Fe/54Fe ratios in siliceous igneous rocks. Geochimica et Cosmochimica Acta 72:4379–4396.

Hoefs J (1997) Stable isotope geochemistry. Springer, Berlin, 286 p

Jonsson E, Troll VR, Högdahl K, Harris C, Weis F, Nilsson KP, Skelton A (2013) Magmatic origin of giant 'Kiruna-type' apatite-iron-oxide ores in Central Sweden. Scientific Reports 3:1644–1644.

Knipping JL, Bilenker LD, Simon AC, Reich M, Barra F, Deditius AP, Lundstrom C, Bindeman I, Munizaga R (2015) Giant Kiruna-type deposits form by efficient flotation of magmatic magnetite suspensions. Geology 43:591–594.

Lund C (2013) Mineralogical, chemical and textural characterisation of the Malmberget iron ore deposit for a geometallurgical model. Ph.D. thesis, Luleå University of technology, 190 p

Lund J (2014) A lithogeochmical study of Northern Sweden and the Kiruna and Malmberget iron-apatite ore deposits. M.Sc. thesis, Uppsala University, 99 p

Martinsson O, Billström K, Broman C, Weihed P, Wanhainen C (2016) Metallogeny of the Northern Norrbotten Ore Province, northern Fennoscandian Shield with emphasis on IOCG and apatite-iron ore deposits. Ore Geology Reviews 78:447–492.

Millet MA, Baker JA, Payne CE (2012) Ultra-precise stable Fe isotope measurements by high resolution multiple-collector inductively coupled plasma mass spectrometry with a Fe-57-Fe-58 double spike. Chemical Geology 304: 18–25.

Ovalle JT, La Cruz NL, Reich M, Barra F, Simon A, Konecke BA, Rodriguez-Mustafa MA, Deditius AP, Childress TM, Morata D (2018) Formation of massive iron deposits linked to explosive volcanic eruptions. Scientific Reports 8.

Parák T (1975) Kiruna iron ores are not "intrusive-magmatic ores of the Kiruna Type. Economic Geology 70:1242–1258.

Simon AC, Knipping J, Reich M, Barra F, Deditius AP, Bilenker, L, Childress T (2018) Kiruna-Type Iron Oxide-Apatite (IOA) and Iron Oxide Copper-Gold (IOCG) Deposits Form by a Combination of Igneous and Magmatic-Hydrothermal Processes: Evidence from the Chilean Iron Belt. In: Arribas AM, Mauk JL (2018) Metals, Minerals, and Society. Society of Economic Geologist, Special Publication 21, p. 89–114.

Sarlus Z, Andersson UB, Martinsson O, Bauer TE, Wanhainen C, Andersson JBH, Whitehouse MJ (2020) Timing and origin of the host rocks to the Malmberget iron oxide-apatite deposit, Sweden. Precambrian Research 342:105652.

Sarlus Z, Martinsson O, Bauer TE, Wanhainen C, Andersson JBH, Nordin R (2018) Character and tectonic setting of plutonic rocks in the Gällivare area, northern Norrbotten, Sweden. GFF 141:1-20.

Severmann S, Anbar AD (2009) Reconstructing paleoredox conditions through a multitracer approach: the key to the past is the present. Elements 5:359-364.

Taylor HP (1968) The oxygen isotope geochemistry of igneous rocks. Contributions to Mineralogy and Petrology 19:1–71.

Tornos F, Velasco F, Hanchar JM (2016) Iron-rich melts, magmatic magnetite, and superheated hydrothermal systems: The El Laco deposit, Chile. Geology 44:427-430.

Troll VR, Weis FA, Jonsson E, Andersson UB, Majidi SA, Högdahl K, Harris C, Millet M, Chinnasamy SS, Kooijman E, Nilsson KP (2019) Global Fe-O isotope correlation reveals magmatic origin of Kiruna-type apatite-iron-oxide ores. Nature Communications 10:1712–1712.

Wen G, Li JW, Hofstra AH, Koenig, AE, Lowers HA, Adams D (2017) Hydrotemral reequilibration of igneous magnetite in altered granitic plutons and its implications for magnetite classification schemes: Insights from the Handan-Xingtai iron district, North China craton. Geochimica et Cosmochimicha Acta 213:255-270.

Westhues A, Hanchar JM, Whitehouse MJ, Martinsson O (2016) New constraints on the timing of host-rock emplacement, hydrothermal alteration, and iron oxide-apatite mineralization in the Kiruna district, Norrbotten, Sweden. Economic Geology 111:1595–1618.

Xie QH, Zhang ZC, Campos E, Deng J, Cheng Z, Fei X, Ke S (2021) Constraints of Fe-O isotopes on the origin of magnetite in the El Laco Kiruna-type iron deposit, Chile. Ore Geology Reviews 130:103967.

Zheng Y (1991) Calculation of oxygen isotope fractionation in metal oxides. Chemical Geology 55:2299–2307.

Variations in Trace Element Chemistry of Pyrite from the Starra IOCG deposit, Queensland, Australia as proxy for Cu-Au mineralization

Max Hohl[1], Jeffrey A. Steadman[1], Jonathan Cloutier[1], Shaun L.L. Barker[2], David R. Cooke[1]
[1]CODES (Centre for Ore Deposit and Earth Sciences), University of Tasmania, Hobart TAS 7001, Australia
[2]Mineral Deposit Research Unit, Department of Earth and Ocean Sciences, University of British Columbia, Vancouver, Canada BC V6T1Z4

Abstract. Iron oxide copper-gold (IOCG) systems are globally significant ore deposits that host essential and critical minerals. Copper-Au mineralization at the Starra IOCG deposit is hosted in magnetite-hematite-rich ironstone lodes, which are emplaced along the Starra shear. Pyrite is a key mineral to assess fluid conditions due to its presence in all rock types and hydrothermal assemblages at Starra. Imaging analysis via LA-ICPMS of pyrite reveals diverse internal chemical zonation with Co, As, Ni and Se as the main non-stoichiometric elements. Cobalt concentrations reach a maximum of 6 wt.%. Gold is predominantly deported together with Te and Bi as micro-inclusions in pyrite. The presence of a high temperature, high salinity magmatic-hydrothermal fluid, likely of a mafic source is inferred from Co/Ni ratios ~100, which locally exceed 1,000. Changes in Ni/Se ratio within a single pyrite grain indicate fluctuating redox and/or temperature conditions. Starras setting along a major shear zone allowing for efficient fluid movement together with an effective chemical trap such as the abundant magnetite-hematite ironstone lodes could have served as major driver in mineralization and especially in Au enrichment.

1 Introduction

Iron oxide copper-gold (IOCG) deposits are a loosely defined group of hydrothermal ore deposits. Since its inception in the early 1990s (e.g., Hitzman et al. 1992), multiple studies have attempted to constrain their paragenetic and geological context (e.g., Williams et al. 2005; Groves et al. 2010). Various criteria like structural setting, relationship to intrusive units, predominant ore mineralogy, and alteration paragenesis have been employed to achieve an agreed definition of a typical IOCG deposit, but it has remained elusive. Common mineral assemblages and spatial association in the Andes between IOCG and iron oxide-apatite (IOA) deposits have provoked ongoing debate about a genetic relationship between both deposit types (e.g., Sillitoe 2003; Knipping et al. 2015; Reich et al. 2016; Tornos et al. 2021). Proposed fluid sources range from purely magmatic (e.g., Rotherham, 1997) to oxidized evaporitic brines (e.g., Barton, 1996) as well as mixtures of both fluid types (e.g., Haynes et al. 1995).

Pyrite chemistry as a proxy for fluid evolution is an established tool in IOCG systems (Rusk et al. 2010; Steadman et al. 2021; del Real et al. 2020). Pyrite occurs in most IOCG systems, where it ranges from being an accessory phase at hematite-dominant IOCG deposits like Olympic Dam (Haynes et al. 1995) to significantly higher abundance in more magnetite-rich members of the IOCG clan, such as Ernest Henry (Williams et al. 2005, Rusk et al. 2010).

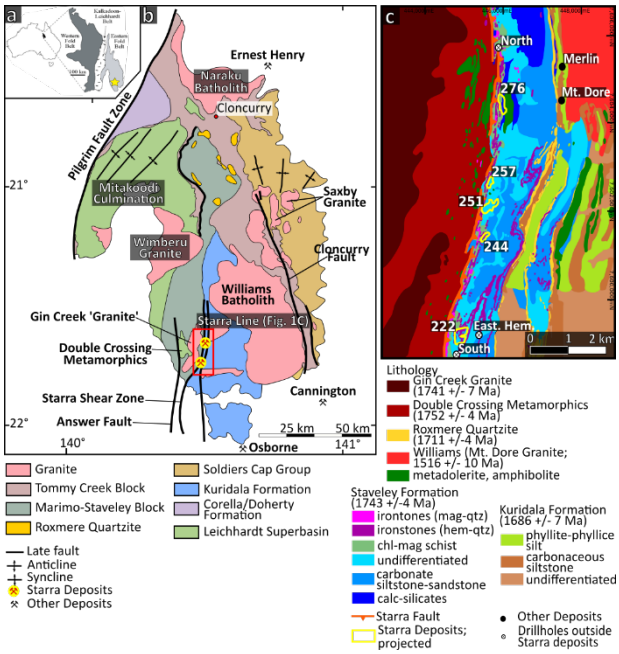

Figure 1. a Location of the Mt. Isa Inlier in Northwest Queensland. **b** Geological map of the Easter Fold Belt with the Starra deposits located in the southern part. **c** Main lithological units in the Starra area

The Starra IOCG system is in the southern part of the Cloncurry district, within the Eastern Succession of the Mt. Isa Inlier in northwest Queensland, Australia. Mineralization occurs at five physically separate deposits in association with unique magnetite-hematite ironstone lodes along the Starra shear (Fig. 1). An early model for Starra included a synsedimentary origin for the ironstones and a sedimentary-exhalative process for Cu-Au mineralization (Davidson, 1989). Subsequent studies suggested a hydrothermal origin for both ironstones and mineralization (Rotherham, 1997) or an involvement of metamorphic derived fluids (Duncan et al. 2014). Among IOCG deposits Starra is considered a relatively Au-rich deposit relative to its Cu content, with a pre-mining resource of 37.4 Mt @ 1.2% Cu and 1.6 g/t Au (Groves et al. 2010).

The main iron oxide in the ironstones ranges between hematite and magnetite dominant. Chalcopyrite is the most abundant Cu-mineral at Starra, followed by bornite and chalcocite. Gold occurs as

Au-Bi tellurides, free gold, and electrum. Gangue minerals in the ironstones are mainly albite, quartz, calcite, and chlorite. Mushketovite, magnetite after hematite, occurs in the magnetite ironstones containing inclusions of scheelite ($CaWO_3$, Fig. 2a).

Metasiltstones of the Staveley Formation in the Starra footwall are strongly hydrothermal altered with mineral assemblages consisting of actinolite, magnetite, biotite and pyrite formed during Ca-Fe-K alteration overprinting earlier albite (Fig. 2b).

In this study, we present trace elemental maps of two pyrite grains using quantitative wavelength dispersive X-ray spectrometry (WDS) and laser ablation-inductively coupled plasma mass spectrometry (LA-ICPMS). The pyrites are from Starra 222 mineralized ironstone and barren footwall. Principal component analysis (PCA) was used to extract covariation of elements across both pyrite grains. Results from the PCA were used for k-nearest neighbor (k-NN) classification to identify chemical comparable zones in both pyrites.

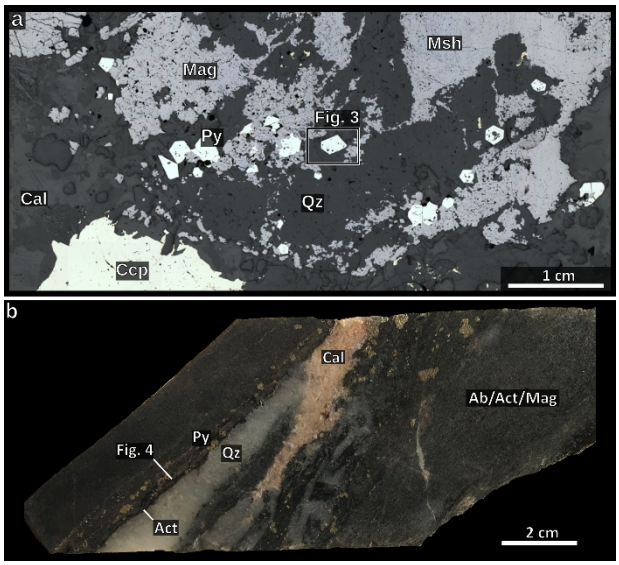

Figure 2. a Reflected light photomicrograph of mineralized magnetite-rich ironstone containing mushketovite and pyrite from Starra 222. **b** Strongly altered footwall sample crosscut by calcite – quartz vein

2 Methods

2.1 Laser ICPMS

All trace element images were acquired at CODES, University of Tasmania. The laser systems consisted of a RESOlution Laser ablation platform with Coherent COMPex Pro 193 laser and Lauren Technic S-155 ablation cell, which was connected to an Agilent 7700 ICPMS, equipped with an extraction lens. For measurement of chalcophile and siderophile elements in sulfides, both STDGL2b2 and STDGL3 were used as standard material. Reference material was analyzed by using a 51 µm round beam ablating at 10 Hz.

2.2 Microprobe

Mineralogy, textural and paragenetic relations were assessed by both reflected light and scanning electron microscopy. Back-scattered electron (BSE) imaging was performed using a Hitachi SU-70 field emission (FE) scanning electron microscope (SEM) housed at the Central Science laboratory (CSL), University of Tasmania (UTAS). Quantitative WDS element maps (S Kα, Fe Kα, Ni Kα, Co Kα, As Kα) were acquired using a JEOL JXA-8530F Plus field emission electron probe microanalyzer (EPMA) at CSL, UTAS. The electron beam was operated at an accelerating voltage of 15 kV, a beam current of 150 nA and a beam diameter of 0.5 µm. Dwell time for each step was 100 ms with a step size of 1 µm.

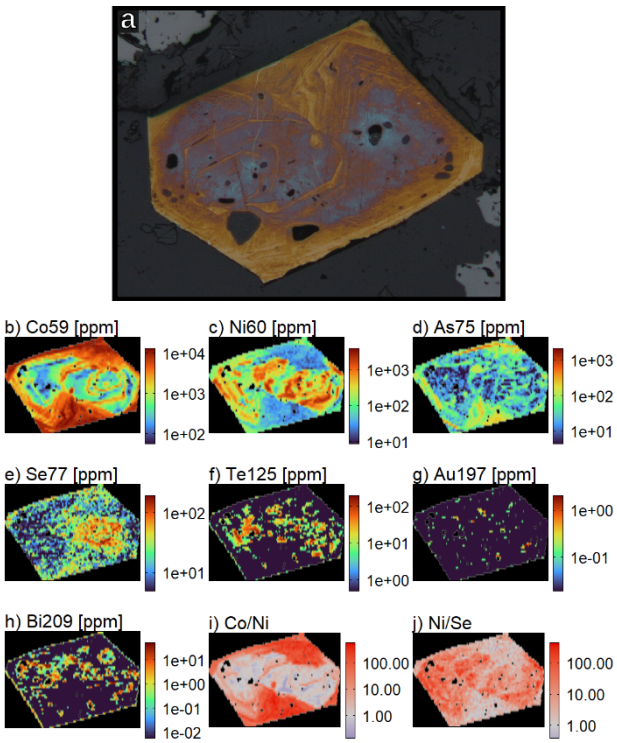

Figure 3. a Reflected light photomicrograph of etched pyrite from the magnetite ironstone. **b-J** Laser ICPMS trace element images of the pyrite shown in **a**

3 Results

3.1 Trace elements composition of pyrite

Concentrations of Co, Ni, As and Se can vary over multiple order of magnitudes within a single pyrite grain (Fig. 2). Cobalt, As and Ni concentration can locally exceed 1 wt. %. Arsenic concentration of > 100 ppm are commonly associated with high Co concentration, whereas high Se of > 100 ppm are correlated with elevated Ni concentrations. Gold occurs as micro inclusions together with Te and Bi, unrelated to As concentrations.

3.2 Multivariate Analysis

Combining both pyrite laser images resulted in 9443 sweeps of the spectrometer. The first principal component (PC) reflects the largest variance within the data set and is defined by correlated variations

in Co, As and ± Se. The second PC is defined by covarying Ni and Se. To a lesser degree Au, Bi and Te variations are covered by the second PC suggesting a mild affinity of gold deportment associated with elevated Ni and Se concentration.

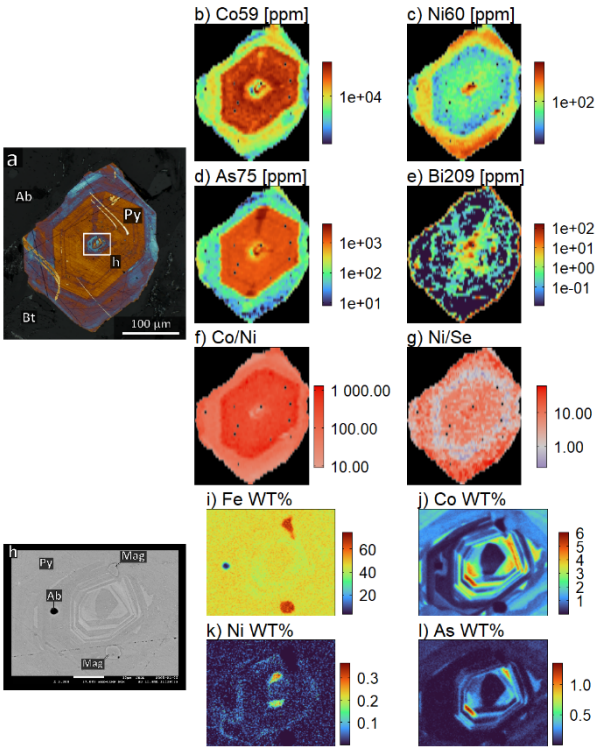

Figure 4. a Reflected light photomicrograph and **b-g** corresponding LA-ICPMS trace element images. **h** Backscattered electron (BSE) photograph and WDS images **i-l** of the pyrite core reveals chemical micron scale zonation, with Co concentration reaching locally up to 6 wt. %

Eigenvalues from the first five PCs, explaining ~88.2 % of the data, are used for a k-NN clustering algorithm, from which three clusters were extracted (Fig. 5). Cluster3 high Co and As concentration, cluster 2 reflects elevated Ni and Se concentration and cluster 3 low concentration of non-stoichiometric elements in pyrite such as Co, Ni, As, Te, Tl, Zn, Cu and Pb. Pyrite from the mineralized ironstone has a core that is represented by cluster 2 and a rim classified as cluster 3. The pyrite associated with early Ca-Fe-K alteration contains all three clusters, with cluster 1 defining the core 1 and 3 defining the rim.

4 Discussion

4.1 Trace Element Systematics

High Co/Ni ratios in pyrite (Co/Ni > 50) are thought to be characteristic of high temperature magmatic-hydrothermal fluids likely sourced from a mafic magma (Reich et al. 2016). Both Co and Ni are enriched in mafic magmas compared to more evolved melts; however, Co distribution coefficient between the melt and the fluid is higher, which results in a higher Co/Ni concentration in the hydrothermal fluid (Liu et al. 2011, 2012). In pyrite a Co/Ni ratio > 50 and a Co/As ratio > 1 can also be associated with hypersaline brines (Keith et al. 2022), which were likely present at Starra during mineralization (Williams et al. 2001). High Co/Ni ratios in pyrite are common in IOCG systems globally (e.g., Rusk et al. 2010; del Real et al. 2020; Steadman et al. 2021) as well as in IOA systems (Reich et al. 2016). This may indicate a potential mafic affinity of the fluids involved in different IOCG systems, as suggested for some of the Andean systems (Sillitoe 2003; Reich et al. 2016; Real et al. 2020).

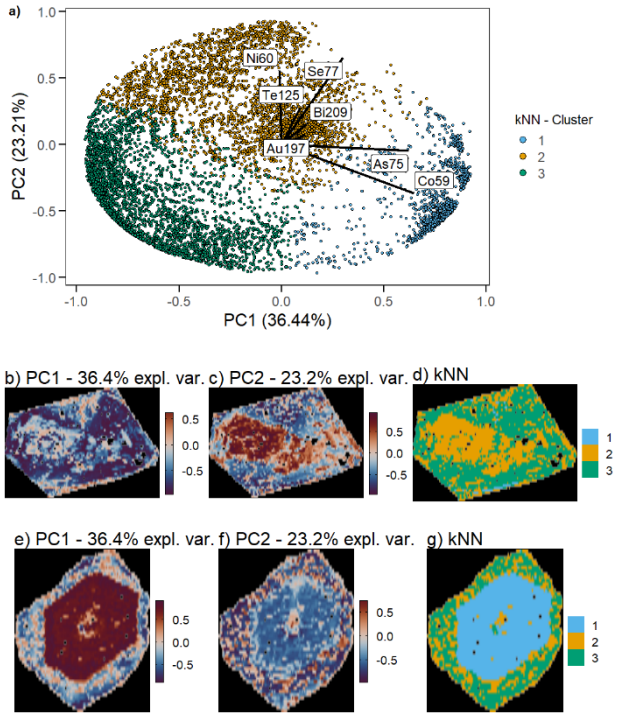

Figure 5. Principal component (PC) analysis of the combined pyrite trace element data. **a** The first two PC separate 3 distinct cluster determined by k-nearest neighbor analysis. **b-g** Eigen Values of PC1 and 2 for both pyrite grains and their corresponding cluster

4.2 Fluid mixing and mineralization

The first PC (based on Co ± As) represents changes in fluid type and source (Reich et al. 2016), the second PC, based on positive correlation between Ni and Se, reflects changes in fluid temperature and/or redox state (Huston et al. 1995, del Real et al. 2020). The three clusters defined by kNN represent major changes in the pyrite chemistry, which are interpreted to be the result of fluids from different sources. Cluster 1only occurs in pyrite associated with early, high-temperature Ca-Fe-K alteration stage (Fig. 5g), which likely reflects highly saline and a mafic affinity of the fluid present during this stage. Gold-Te-Bi inclusions are associated with cluster 2, relatively low Co/Ni and high Ni/Se ratio implying gold deportment under relative oxidizing conditions. The rim of the pyrite associated with mineralization formed likely under more reduced

condition compared to the core based on Ni/Se ration (Fig. 3i-j). A pulse of reduced fluid following more oxidized conditions is also suggested by the occurrence of mushketovite in the ironstone assemblage, which coincides with chalcopyrite formation. The difference between Cu and Au deportment suggests that at least two distinct fluids contributed to the mineralization at Starra. It is likely that the regional structures, such as the Starra Shear, functioned as fluid conduits for basinal brines, that led ultimately to Au enrichment of the Starra deposits, explaining their relative Au-rich nature compared IOCG deposits globally (Groves et al. 2010).

5 Conclusions

Trace element analysis of pyrite has revealed highly variable chemical clusters, reflecting a complex, multistage fluid evolution leading to Cu-Au mineralization. Changes in fluid conditions such as temperature and/or fO_2 are a major process controlling the mineralization at Starra. In the magnetite ironstones Cu mineralization coincides with the formation of mushketovite. Pyrite rims formed during this stage have high Co/Ni (~100) and low Ni/Se (~1) ratios suggesting a reduced, highly saline fluid, with a mafic affinity. Gold inclusion in pyrite are associated with a more oxidized, lower salinity fluid. Starras emplacement along ironstone horizons and regional structures, which likely represented major conduits for basinal derived fluids, are inferred to be crucial in making Starra an Au-rich member within the IOCG deposit spectrum.

Acknowledgements

The Geological Survey of Queensland is thanked for providing funding and Chinova Resources for assistance during field work. CODES Analytical Laboratories and Central Science Laboratories, both at UTAS, are thanked for laboratory assistance.

References

Barton MD, Johnson DA (1996) Evaporitic-source model for igneous-related Fe oxide–(REE-Cu-Au-U) mineralization. Geology 24:259–262

Bastrakov EN, Skirrow RG, Davidson GJ (2007) Fluid evolution and origins of iron oxide cu-au prospects in the Olympic Dam district, Gawler craton, South Australia. Economic Geology 102:1415–1440

Davidson GJ (1989) Starra and trough tank: iron-formation-hosted gold-copper deposits of North-West Queensland, Australia. PhD thesis, University of Tasmania

Duncan RJ, Hitzman MW, Nelson EP, Togtokhbayar O (2014) Structural and lithological controls on iron oxide copper-gold deposits of the southern Selwyn-Mount Dore corridor, Eastern fold belt, Queensland, Australia. Economic Geology 109:419–456

del Real, I., Thompson, J.F.H., Simon, A.C., and Reich, M., 2020, Geochemical and isotopic signature of pyrite as a proxy for fluid source and evolution in the Candelaria-Punta del Cobre iron oxide copper-gold district, Chile: Economic Geology, v. 115, p. 1493–1517.

Groves DI, Bierlein FP, Meinert LD, Hitzman MW (2010) Iron oxide copper-gold (IOCG) deposits through Earth history: Implications for origin, lithospheric setting, and distinction from other epigenetic iron oxide deposits. Economic Geology 105:641–654

Haynes DW, Cross KC, Bills RT, Reed MH (1995) Olympic Dam ore genesis; a fluid-mixing model. Economic Geology 90:281–307

Hitzman MW, Oreskes N, Einaudi MT (1992) Geological characteristics and tectonic setting of Proterozoic iron oxide (Cu-U-Au-REE) deposits. Precambrian research 58:241–287

Hu, X., Chen, H., Beaudoin, G., and Zhang, Y., 2020, Textural and compositional evolution of iron oxides at Mina Justa (Peru): Implications for mushketovite and formation of IOCG deposits: American Mineralogist: Journal of Earth and Planetary Materials, v. 105, p. 397–408.

Huston D, Sie S, Suter G (1995) Selenium and its importance to the study of ore genesis: the theoretical basis and its application to volcanic-hosted massive sulfide deposits using pixeprobe analysis. Nuclear Instruments and Methods in Physics Research Section B: Beam Interactions with Materials and Atoms 104:476–480

Keith, M., Haase, K. M., Chivas, A. R., and Klemd, R., 2022, Phase separation and fluid mixing revealed by trace element signatures in pyrite from porphyry systems: Geochimica et Cosmochimica Acta.

Knipping JL, Bilenker LD, Simon AC, et al (2015) Trace elements in magnetite from massive iron oxide-apatite deposits indicate a combined formation by igneous and magmatic-hydrothermal processes. Geochimica et Cosmochimica Acta 171:15–38

Liu W, Borg SJ, Testemale D, et al (2011) Speciation and thermodynamic properties for cobalt chloride complexes in hydrothermal fluids at 35–440 c and 600 bar: An in-situ XAS study. Geochimica et Cosmochimica Acta 75:1227–1248

Liu W, Migdisov A, Williams-Jones A (2012) The stability of aqueous nickel (II) chloride complexes in hydrothermal solutions: Results of UV–visible spectroscopic experiments. Geochimica et Cosmochimica Acta 94:276–290

Reich M, Simon AC, Deditius A, et al (2016) Trace element signature of pyrite from the Los Colorados iron oxide-apatite (IOA) deposit, Chile: A missing link between Andean IOA and iron oxide copper-gold systems? Economic Geology 111:743–761

Rotherham JF (1997) Origin and fluid chemistry of the Starra ironstones and high grade Au-Cu mineralisation, Cloncurry district, Mount Isa inlier, Australia. PhD thesis, James Cook University of North Queensland

Rusk B, Oliver N, Cleverley J, et al (2010) Physical and chemical characteristics of the Ernest Henry iron oxide copper gold deposit, Australia; implications for IOGC genesis. PGC Publishing

Sillitoe RH (2003) Iron oxide-copper-gold deposits: an Andean view. Mineralium Deposita 38:787–812

Steadman JA, Large RR, Olin PH, et al (2021) Pyrite trace element behavior in magmatic-hydrothermal environments: An LA-ICPMS imaging study. Ore Geology Reviews 103878

Tornos F, Hanchar JM, Munizaga R, et al (2021) The role of the subducting slab and melt crystallization in the formation of magnetite-(apatite) systems, Coastal Cordillera of Chile. Mineralium Deposita 56:253–278

Williams, P. J., Dong, G., Ryan, C. G., Pollard, P. J., Rotherham, J. F., Mernagh, T. P., and Chapman, L. H., 2001, Geochemistry of hypersaline fluid inclusions from the Starra (Fe oxide)-Au-Cu deposit, Cloncurry district, Queensland: Economic Geology, v. 96, p. 875–883.

Williams PJ, Barton MD, Johnson DA, et al (2005) Iron oxide copper-gold deposits: Geology, space-time distribution, and possible modes of origin. Economic Geology 371–405

Hydrothermal origin of bladed titanomagnetite during early alteration stages at the Starra IOCG deposits, Queensland, Australia

Max Hohl[1], Jeffrey A. Steadman[1], Jonathan Cloutier[1], Karsten Goemann[2]
[1]CODES (Centre for Ore Deposit and Earth Sciences), University of Tasmania, Hobart TAS 7001, Australia
[2]Central Science Laboratory, University of Tasmania, Hobart, TAS 7001, Australia

Abstract. The Starra iron oxide copper-gold (IOCG) deposits are located in the Cloncurry district, Queensland, Australia. Mineralization at Starra is hosted by extensive hematite and magnetite lodes, locally referred to as ironstones. The origin of both ironstones and Cu-Au mineralization in the Cloncurry district remains debated. Improving our understanding of fluid conditions during early IOCG formation is critical for future exploration success in the district.

In this study we present a sample from the Starra footwall containing titanomagnetite hosted by a calcite vein. The calcite vein crosscuts unaltered metasedimentary host rocks and is associated with early alteration stages. The titanomagnetites texture resembles specular hematite and contains exsolution of ilmenite and rutile. Near its tip the titanomagnetite breaks down into a mixture of titanite, anhydrite, and calcite. Based on the titanomagnetites texture, associated mineralogy and the stratigraphic position of the calcite vein a hydrothermal origin of the mineral assemblage is inferred. The bladed texture of the titanomagnetite implies rapid growth, which promotes the incorporation of trace elements into the magnetite lattice. The high Ti concentration of the magnetite implies the presence of a highly saline and/or high temperature fluid, which can mobilize significant Ti concentrations, during early alteration stages at Starra.

Acknowledgements

The Geological Survey of Queensland is thanked for providing funding and Chinova Resources for assistance during field work. CODES Analytical Laboratories at UTAS are thanked for laboratory assistance.

A geological update on the Viscaria Cu-Fe deposit, Kiruna district, Northern Sweden.

Marcello Imaña[1], Ross Armstrong[1,2], Daniel Sandoval[1,2], Maciej Jeż [1,3], Elvis Nkioh[1], Maximilian Krockert[1]
[1]*Copperstone Resources AB*
[2]*Uppsala University, Sweden*
[3]*Polish Academy of Sciences, Poland*

Abstract. The Viscaria Cu-Fe ore deposit is located adjacent to the Fe-oxide-apatite-REE Kiruna mining operation in the Proterozoic domain of Northern Sweden. Despite common geological features existing between Viscaria and the epigenetic Kirunavaara ores, an initially conceived syngenetic hypothesis for Viscaria ore formation has remained unquestioned. This contribution brings a re-evaluation through a holistic interpretation of both historical and new stratigraphic, geochemical, and geophysical data. Primary lithological and structural constraints are outlined as key controls for fluid flow and metal deportment, thus impacting the exploration outlook for undiscovered Cu deposits in the district.
The Viscaria deposit consists of stratabound, massive and semi-massive magnetite with varied proportions of Fe and Cu sulphides and carbonate. Mineralization extends laterally within a well-preserved low metamorphic volcano-sedimentary stratigraphy, showing preference to horizons of enhanced permeability within areas of contrasting redox compositions. High temperature coarse grained calc-silicate-sulphides assemblages occur in dissolution and upward escape channel breccias and vein networks to pervasive replacement of pre-existing Fe-enriched lithologies, indicating that the ore fluid was underpressured. A mineral and textural zonation indicates that stratigraphically upper parts of the stratigraphy receive higher proportion of volatile and finer grained components indicating that vertical temperature gradients appeared prior to major tectonic tilting.

1 Introduction

The Viscaria Cu deposit was subject to continuous open pit and underground mining between 1985 and 1995, yielding a production of 12.54 Mt of ore at 2.3% Cu. The updated total resources (mined and remaining) in the deposit contains over 1 Mt metal Cu, as well as a significant amount of magnetite and minor accompanying metals such Co, Ag, Zn, REEs and Au. The Viscaria system is of particular interest not only for its proximal location to the stratigraphically-higher Kirunavaara Fe-apatite ore deposit (>2000 Mt @ 62% Fe) but also due to the spatial and temporal relationship that is commonly observed between Fe and Cu-Fe deposits in mining districts across the world: e.g., the Malmberget-Nautanen district (Sweden), Punta del Cobre district (Chile), Carajas district (Brazil), the Coastal Cu Belt (Peru), and the Eastern Gawler Craton (Australia). The subaqueous nature of the Viscaria greenstones and the close connection of parts of the Cu mineralization with carbonaceous shales has led to the traditional acceptance of VMS-type ore genesis for Viscaria. In addition to Viscaria, several other Cu deposits exist in the district (Fig.1), emplaced at similar but also different stratigraphic positions, ranging from stratabound replacements to discordant hydrothermal breccias and shear-hosted orebodies: e.g., Rakkurijarvi, (Smith et al. 2007), Pahtohavare (Martinsson 1997), and Kiskamavaara (Martinssson 2011).

Despite the Proterozoic age of the host formation, deformation and metamorphism have only had a limited effect and a penetrative fabric is widely missing in the area, except for very localized shear zones. The volcano-sedimentary sequence is well-preserved and tilted 90 degrees, with a distinct geophysical signature that can be traced for several kilometers. Therefore, tectonic tilting and a subsequent lack of major intrusion emplacement in the area has left an unusually thick and continuous succession of altered stratigraphy exposed that represents a transition from 2.1 to 1.88 Ga volcanic activity. Despite the Viscaria ore being hosted in the westward, older parts of the sequence, its emplacement style and links to common structural and paragenetic features with the overlying Kiruna ores possibly point toward a similar age of emplacement.

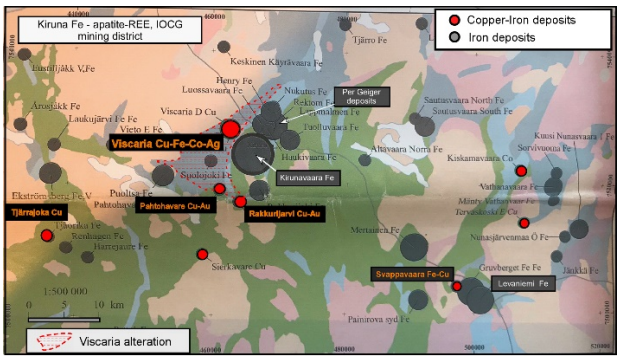

Figure 1. Map showing the location of the Kiruna deposit within the Kiruna mining district

2 District architecture, alteration footprint and metal deposition

2.1 District architecture

Good preservation and a lower intensity of regional metamorphism is characteristic of the Viscaria-Kiruna area (Andersson et al 2021). The area is mostly buried by moraine cover which has enabled the utilization of regional and district scale geophysical datasets to investigate the structural configuration. The Viscaria-Kiruna deposits coincide within a NW-SE trending gravity lineament that is interpreted to represent reactivated basement structures originated as part of a failed regional rift

during the Rhyacian period. Magnetic and airborne electromagnetic information have outlined local reactivated structures that link Viscaria and Per Geijer ores. Figure 2.

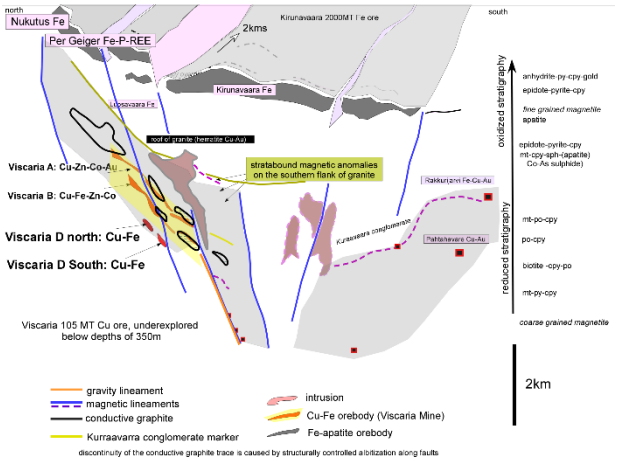

Figure 2. Schematic section originated from airborne and ground geophysical data tilted 90 degrees from Viscaria Kiruna area.

2.2 Alteration footprint

The near-surface extent of hydrothermal alteration in Viscaria exceeds an area of 20 km^2, affecting several kilometers of the stratigraphic sequence. A part of the alteration in the district is represented by Fe-enriched facies, followed by enrichments in Na, K and Mg represented by albite, biotite and tremolite-actinolite alterations respectively. The extent of these alterations is much larger than areas where sulphur reduction and Cu-sulphide precipitation has occurred.

Alteration is pervasively constrained within permeable lithologies, and the composition varies drastically from west to east, from deeper to shallower levels of the stratigraphy being affected with Mg, K and Na enrichment accordingly. Favorable structural lineaments transect the stratigraphy from west to east without producing major dislocations. Fluid flow carried out along these structures has affected the composition of adjacent rock sequences; this effect is more-clearly observed in areas where pervasive albitization has bleached and obliterated the strong conductivity signature of black shales, representing areas of a consequently reduced conductivity signature and truncation of magnetic anomalies. Proximal alteration linked to sulphide precipitation is represented by amphibole and epidote formation accompanied by lower temperature barren talc, silica and carbonate deposition.

2.3 Depositional pathways

These structures can be extrapolated into the northeastern parts of the district where they transect upper volcanic rhyodacitic sequences host of the Kiruna and Per Geiger ores (Figure 2). At this level, limited overprinting sulphide mineralization has a more oxidized character than observed in Viscaria. Coherent sills of gabbroic composition occur within the Viscaria stratigraphy and are vein-mineralized in proximity to main ENE WSW structures.

3 Discussion and Conclusions

The Viscaria Kiruna stratigraphy depicts the incursion and pervasive interaction and mixing with variably saline brines resulting in a clear stratigraphic differentiation of the alteration composition. The oxide and sulphide paragenesis is represented by early magnetite replacement of hematite, magnetite pyrite, cobaltite-Ag, magnetite-pyrrhotite-chalcopyrite and late pyrite-chalcopyrite-anhydrite veins. The relative abundance of these paragenesis is dictated by the redox potential encountered at different levels of the stratigraphy. Higher in the stratigraphy, the Per Geijer ores are typical of the more oxidised, hydrous, lower temperature assemblages that occur above magnetite in IOCG deposits (Hitzmann et al., 1992). Thus, they give a vector that indicates that the upper parts of the system occur to the northeast and east (Redwood 2022).

Although there is an impressive Fe enrichment and magnetite formation towards the stratigraphy hosting the Kirunavaara Fe ores, these ores lack the exceptional Cu and sulphide enrichment observed in the lower Viscaria level. Oxidized sulphur (anhydrite) carbonates and apatite are all common component depicting devolatilization and accumulation of these component towards the upper parts of stratigraphy. The overall magmatic hydrothermal flux is suspected to have happened before the major compression that has originated the present days tilted geology of the volcanic and sedimentary Viscaria-Kirunavaara succession. Thus, continuous epigenetic fluid flux is highly influenced by the redox behaviour of early alteration assemblages and the organic carbon.

Acknowledgements

Copperstone Resources AB is acknowledged for allowing to present this contribution. District geology and drillcore discussions with Dr. Stewart Redwood and Dr. William X. Chavez during their visits to the Viscaria site are greatly appreciated.

References

Andersson JBH, Bauer TE, Martinsson O (2021) Structural Evolution of the Central Kiruna Area, Northern Norrbotten, Sweden: Implications on the Geologic Setting Generating Iron Oxide-Apatite and Epigenetic Iron and Copper Sulfides. Economic Geology 116:1981–2009. https://doi.org/10.5382/ECONGEO.4844

Martinsson O (1997) Tectonic Setting and Metallogeny of the Kiruna Greenstones. Luleå University of Technology

Martinsson O (2011) Kiskamavaara a shear zone hosted IOCG-style of Cu-Co-Au deposit in Northern Norrbotten, Sweden. In: The 11th Biennial Meeting of The SGA, Antofagasta, Chile. pp 393–414

Redwood SD (2022) Review of the exploration, geology and deposit model of the Viscaria copper project, Norrbotten County, Sweden

Smith M, Coppard J, Herrington R, Stein H (2007) The Geology of the Rakkurijarvi Cu-(Au) Prospect, Norrbotten: A New Iron Oxide-Copper-Gold Deposit in Northern Sweden. Economic Geology 102:393–414. https://doi.org/10.2113/gsecongeo.102.3.393

The Formation of the Pilot Knob Iron Ore Cluster in Southeast Missouri, USA: Implication for the Exploration for Iron Oxide Apatite Deposits

Marek Locmelis[1], Bolorchimeg Nanzad Tunnell[2], Brandon Sullivan[3], Cheryl Seeger[4], Sarah Dare[5], Marilena Moroni[6], Ryan Mathur[7]
[1]Department of Geosciences and Geological and Petroleum Engineering, Missouri University of Science and Technology, Rolla, Missouri, USA
[2]Department of Geology and Hydrogeology, Mongolian University of Science and Technology, Ulaanbaatar, Mongolia
[3]Doe Run Company, Viburnum, Missouri, USA
[4]Missouri Department of Natural Resources, Missouri Geological Survey, USA
[5]Département de Sciences Appliquées, Université du Québec á Chicoutimi, Canada
[6]Department of Earth Sciences, University of Milan, Italy
[7]Juniata College, Huntingdon, Pennsylvania, USA

Abstract. The St. Francois Mountains Terrane in southeast Missouri, USA, contains 7 major Iron Oxide Apatite (IOA) and Iron Oxide Copper Gold (IOCG) deposits as well as numerous smaller iron ore deposits. These deposits were mined for iron ore from the 1800s until 2001. Although there are currently no iron ore mining activities in Missouri, there is renewed interest in these deposits because of their 'critical mineral' potential, most notably cobalt and the rare earth elements. Here we present the findings of an ongoing study that examines the potential of the St. Francois Mountains Terrane to host undiscovered IOA and IOCG deposits. The focus is on the Pilot Knob Ore cluster that comprises the subsurface Pilot Knob Magnetite IOA deposit, and the outcropping Pilot Knob Hematite, Shepherd Mountain, and Cedar Hill deposits. New data is presented for hematite from the Cedar Hill deposit and integrated with data from the other deposits in the Pilot Knob Ore Cluster. We argue that all deposits are part of the same magmatic to hydrothermal plumbing system and that studies of other outcropping small-scale deposits in southeast Missouri may lead to the discovery of subsurface IOA ore bodies.

1 Introduction

The St. Francois Mountains Terrane in southeast Missouri, USA, contains 7 major Iron Oxide Apatite (IOA) and Iron Oxide Copper Gold (IOCG) deposits. Additionally, the region hosts more than twenty smaller deposits, including steeply dipping vein-type deposits and low-temperature hydrothermal hematite replacement ore deposits that occur within early-to-middle Mesoproterozoic plutonic, volcanic and volcaniclastic sedimentary rocks. These deposits were mined for iron ore from the 1800s until 2001. Although there are currently no iron ore mining activities in Missouri, there is renewed interest in these deposits because of their 'critical mineral' potential, most notably cobalt and the rare earth elements. Here we present the findings of an ongoing study that examines the potential of the St. Francois Mountains Terrane to host undiscovered IOA and IOCG deposits.

2 Geologic Overview

Iron ore deposits in southeast Missouri are hosted in 1.3 to 1.5 Ga granites and rhyolites of the St. Francois Mountains Terrane (Fig. 1). The terrane is characterized by extensive caldera-forming volcanism and cogenetic subvolcanic and plutonic rocks, mostly rhyolitic in composition with minor intermediate to mafic rocks. Iron ore deposits in the region have been suggested to be genetically associated with early Mesoproterozoic ring intrusions (1.50–1.44 Ga) with a structurally controlled emplacement of iron ore along caldera-related ring structures (Tunnell et al. 2021 and references therein).

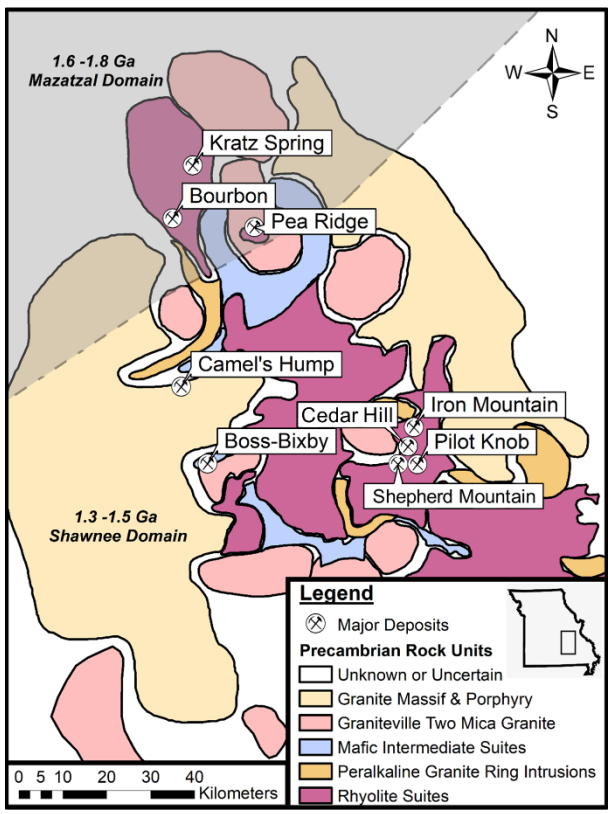

Figure 1. Geologic map that shows the location of the Pilot Knob Ore Cluster in in the St. Francois Mountains Terrane modified from Day et al. (2016) and Sullivan et al. (2023). The inset shows the location of the map within the US State of Missouri.

2.1 The Pilot Knob Ore Cluster

The Pilot Knob Ore Cluster is located near the town of Pilot Knob in Iron County, Missouri. The cluster comprises four iron ore deposits that were previously mined, i.e., (i) the Pilot Knob Magnetite subsurface IOA deposit, and the outcropping (ii) Pilot Knob Hematite deposit that is located 240 m stratigraphically above the IOA ore body, (iii) the vein-type Shepherd Mountain magnetite-dominated deposit, and (iv) the vein-type Cedar Hill hematite-dominated deposit. The four deposits occur within less than 2 km of one another.

3 Methodology

New data is presented for the vein-type Cedar Hill deposit. Because the ore veins are fully mined out, sampling was restricted to tailing piles. Representative samples were prepared as polished thin sections and reflection mounts. The major and minor element chemistry of hematite was determined using a JEOL JXA-8200 electron microprobe in the Department of Earth Sciences, University of Milan, Italy. Major elements were determined with an accuracy of better than 3% and an external precision of better than 3 % (2-sigma). Minor elements were determined with an accuracy of better than 5% and an external precision of better than 4% (2-sigma). The trace element composition of iron oxide minerals was determined via laser ablation ICP-MS analysis at LabMaTer at the Université of Québec at Chicoutimi, Canada, using a Resonetics M-50 193 nm laser unit connected to an Agilent 7900 ICP-MS. Most trace elements were determined with a precision of better than 8% and an external precision of better than 6% (2-sigma). The iron isotope chemistry of hematite concentrates was conducted using a Neptune multi-collector ICP-MS at Pennsylvania State University, USA, following hematite dissolution in aqua regia and iron purification using BioRad MP-1 anion exchange resin. Errors were within the range of 0.1‰ (2-sigma) of the standards.

4 Results

Iron ore mineralization at Cedar Hill occurred in two approximately parallel veins that were emplaced into a pinkish to greyish tuff breccia that is interlayered with flow-banded rhyolites, imbricated breccias and conglomerates, massive rhyolite ash-flow tuffs, and banded rhyolite tuffs. The fully mined-out veins were 0.3-1.2 m in width and outcropped for a distance of about 30 m in a northwest-southeast direction (Crane, 1912). Petrographic studies of representative samples from tailing piles show that the mineralization is dominated by laminated fine-grained hematite (Fig. 2A-B) with locally rounded hematite grains with colloform textures (Fig. 2C). In some samples, coarse crosscutting specular hematite fills open spaces within the host volcanic breccia (Fig. 2D).

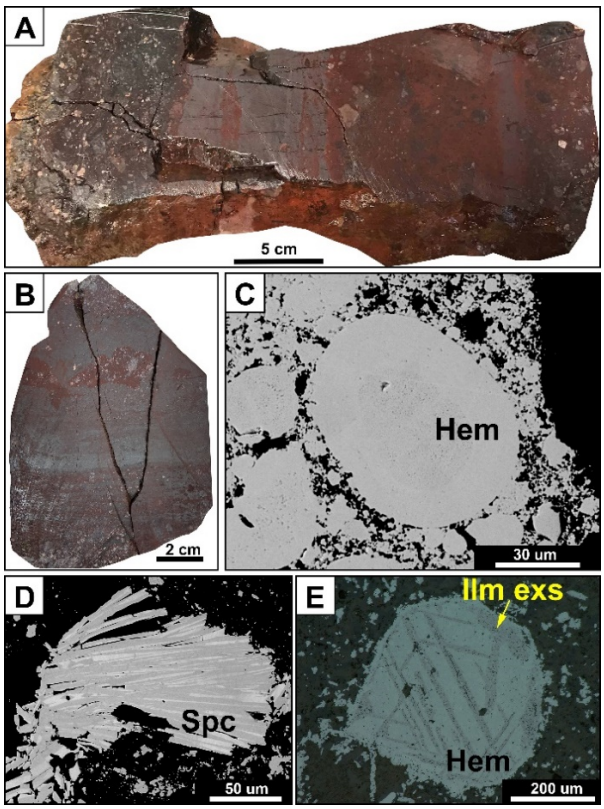

Figure 2. (A-B) Hand samples showing the laminated hematite ore within tuff breccia at Cedar Hill. (C-D) Back-scattered electron images showing rounded hematite (Hem) with colloform texture and specularite (Spc). (E) Hematite with ilmenite exsolutions in reflected light from the Cedar Hill deposit.

Locally, hematite grains contain ilmenite exsolutions (Fig. 2E), similar to hematite observed in brecciated ores from the Pilot Knob Hematite deposit. The major, minor and trace element chemistry of hematite from the Cedar Hill deposit is notably similar to the composition of hematite from other iron ore deposits in the Pilot Knob cluster, i.e., the Pilot Knob hematite deposit (Fig. 3A) and the Shepherd Mountain and Pilot Knob Magnetite IOA deposits (Fig. 3B). The δ^{56}Fe values of hematite from Cedar Hill range from -0.13‰ to -0.41‰. These values are similar to the δ^{56}Fe values observed for iron oxide minerals from Shepherd Mountain (δ^{56}Fe = -0.07‰ to -0.55‰), slightly lower than ratios of brecciated hematite reported for the Pilot Knob Hematite deposit (δ^{56}Fe = -0.19‰ to 0.01‰), and notably lower when compared to iron oxides from the bedded hematite and magnetite zones from the two Pilot Knob deposits (δ^{56}Fe = 0.06‰ to 0.30‰; Fig. 4).

5 On the formation of the Cedar Hill Deposit

The presence of hematite with ilmenite exsolutions is interpreted to reflect a magmatic origin wherein ilmenite exsolved from Ti-rich magmatic magnetite along its crystallographic planes prior to eruption. The magnetite was subsequently replaced by hematite during more oxidizing conditions, resulting in hematite with ilmenite lamellae, similar to the

observations made for the brecciated hematite with ilmenite lamellae from the Pilot Knob Hematite deposit (Tunnell et al. 2021). Later hydrothermal fluids infiltrating the brecciated tuff precipitated fine-grained hematite and specular hematite ('specularite') within the host breccia tuff. The narrow range of δ^{56}Fe values of hematite from Cedar Hill (-0.13‰ ~ -0.41‰) likely reflect precipitation from hydrothermal fluid(s) as opposed to a sedimentary origin that commonly results in more variable δ^{56}Fe signatures (Dauphas et al., 2007). A hydrothermal origin, rather than a sedimentary origin, is also in agreement with the vein-type emplacement style of the Cedar Hill ore veins. Similar to the observations made for the Shepherd Mountain deposit (Tunnell et al. 2022), the slightly lighter δ^{56}Fe values of Cedar Hill hematite when compared to brecciated hematite from the Pilot Knob Hematite deposit, likely reflect the higher stratigraphic emplacement level of the Cedar Hill deposit and associated Fe isotope fractional upon ascend/cooling, as well as mixing with meteoric waters.

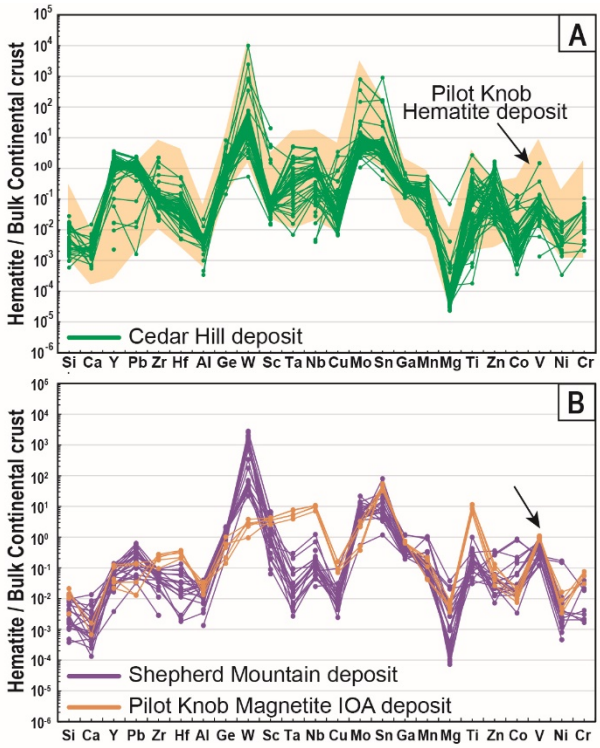

Figure 3. (A) Composition of hematite from the Cedar Hill and the Pilot Knob Hematite deposits. (B) Composition of hematite from the Shepherd Mountain and the Pilot Knob Magnetite IOA deposits. The order of elements is based on increasing compatibility into magnetite (Dare et al. 2014). All data are normalized against the composition of the bulk continental crust after Rudnick and Gao (2003).

6 New insights into the formation of the Pilot Knob Ore Cluster

Recent studies have shown that the Pilot Knob Magnetite IOA deposit and the outcropping Pilot Knob Hematite and Shepherd Mountain deposits are genetically related (Tunnell et al. 2021, 2022). Magmatic-hydrothermal fluid(s) exsolved from a deep-seated magma chamber migrated upwards and formed the subsurface Pilot Knob Magnetite IOA deposit. Further upward migration of hydrothermal fluids along local fault systems resulted in the formation of the hematite-dominated replacement ore in the Pilot Knob Hematite deposit and the magnetite-dominated vein-type Shepherd Mountain deposit.

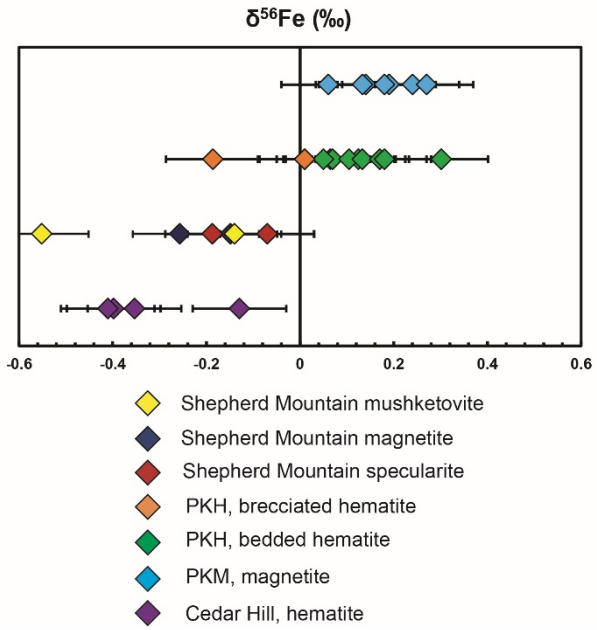

Figure 4. The δ^{56}Fe iron isotopic compositions of hematite from the Pilot Knob Ore cluster. Magnetite data are included for comparison. With data from Childress et al. 2016, Tunnell et al. 2021 (Pilot Knob), (Pilot Knob), and Tunnell et al. 2022 (Shepherd Mountain).

Several lines of evidence suggest that the Cedar Hill deposit is also genetically related to the other deposits in the Pilot Knob ore cluster. In addition to the spatial proximity and the vein-type emplacement style similar to the Shepherd Mountain deposit, the chemistry of hematite is notably similar to hematite from the other deposits in the ore cluster (Fig. 3). Moreover, there are distinct similarities in the δ^{56}Fe iron isotopic values for iron oxide minerals from the two vein-type deposits in the system, i.e., Cedar Hill and Shepherd Mountain (Fig. 4). It is noted that these values are notably lower when compared to the Pilot Knob Hematite deposit replacement ore, as well as the underlying IOA deposit, likely reflecting the higher stratigraphic emplacement level of the vein-type deposits as discussed above.

Because of the similarities, it is argued that all four iron ore deposits in the Pilot Knob area belong to the same magmatic-hydrothermal plumbing system. In this scenario, the fluids that were exsolved from the Pilot Knob Magnetite IOA ore body and migrated upwards along local faults not only formed the Pilot Knob hematite and Shepherd

Mountain deposits, but also the iron ore veins at Cedar Hill (Fig. 5).

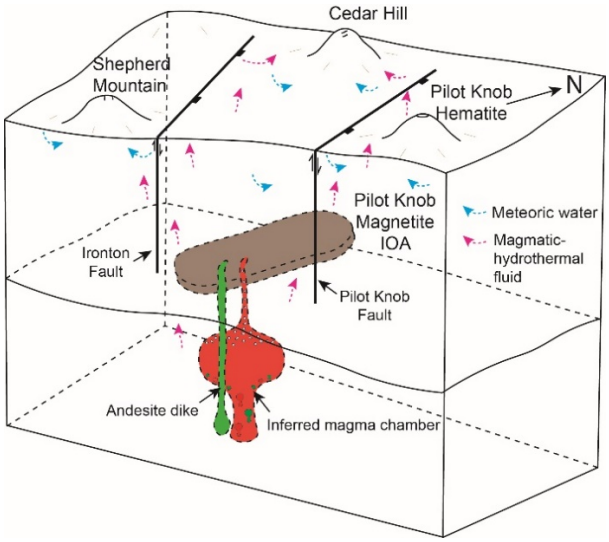

Figure 5. Proposed model for the formation of the Pilot Knob Ore Cluster integrating observations from this study and Tunnell et al. (2021, 2022). Not to scale.

7 Implications for the Exploration for IOA and IOCG Deposits

The model for the formation of the Pilot Knob ore cluster illustrated in Figure 5 suggests that the Pilot Knob Hematite, Shepherd Mountain, and Cedar Hill deposits are the outcropping hydrothermal expressions of the deeper magmatic-hydrothermal ore-forming processes that formed the sub-surface Pilot Knob Magnetite IOA deposit. It is noted that more than 20 other prospects exist in the St. Francois Mountains terrane that were discovered, but never scientifically studied. Prominent examples include Ketcherside Gap, Cuthbertson Mountain, and College Hill all of which occur along the edge of caldera ring structures (Day et al. 2016). We argue that understanding the magmatic-hydrothermal plumbing system that was feeding the near-surface-near prospects might lead to the discovery of subsurface IOA ore bodies. It is noted that this hypothesis appears to be supported by the presence of large subsurface magnetic susceptibility anomalies that were discovered during aeromagnetic surveys (e.g., McCafferty et al. 2016; 2019). Our future research will integrate geophysical models with field studies and petrological, mineralogical, and geochemical studies to guide conceptual exploration targeting for subsurface IOA ore bodies in Southeast Missouri.

Acknowledgements

M. L. acknowledges support through the National Science Foundation (NSF) CAREER award #1944552 “Investigating the source, transport and deposition of economically important metals in the lower continental crust”. Audrey Lavoie at LabMaTer of the UQAC is thanked for carrying out the LA-ICP-MS analysis. We further thank Mr. Andrea Risplendente, University of Milan, for assistance during the microprobe analyses. Lisa Lori from the Doe Run Company and Patrick Scheel from the Missouri Department of Natural Resources are thanked for help during fieldwork.

References

Crane GW (1912) The iron ores of Missouri. Missouri Bureau of Geology and Mines. 10:434.

Childress TM, Simon AC, Day WC, Lundstrom CC, Bindeman IN (2016) Iron and Oxygen Isotope Signatures of the Pea Ridge and Pilot Knob Magnetite-Apatite Deposits, Southeast Missouri, USA. Econ Geol 111:2033-2044. https://doi.org/10.2113/econgeo.111.8.2033.

Dare SA, Barnes SJ, Beaudoin G, Méric J, Boutroy E, Potvin-Doucet C (2014) Trace elements in magnetite as petrogenetic indicators. Miner Deposita 49:785-796. https://doi.org/ 10.1007/s00126-014-0529-0.

Dauphas N, Cates NL, Mojzsis SJ, Busigny V (2007) Identification of chemical sedimentary protoliths using iron isotopes in the >3750 Ma Nuvvuagittuq supracrustal belt, Canada. Earth Planet Sci Lett 254:358-376. https://doi.org/10.1016/j.epsl.2006.11.042.

Day WC, Slack JF, Ayuso RA, Seeger CM (2016) Regional Geologic and Petrologic Framework for Iron Oxide ± Apatite ± Rare Earth Element and Iron Oxide Copper-Gold Deposits of the Mesoproterozoic St. Francois Mountains Terrane, Southeast Missouri, USA. Econ Geol 111:1825-1858. https://doi.org/10.2113/ econgeo.111.8.1825.

McCafferty AE, Phillips JD, Driscoll RL (2016) Magnetic and Gravity Gradiometry Framework for Mesoproterozoic Iron Oxide-Apatite and Iron Oxide-Copper-Gold Deposits, Southeast Missouri. Econ Geol 111:1859-1882. https://doi.org/10.2113/econgeo.111.8.1859.

McCafferty AE, Phillips JD, Hofstra AH, Day WC (2019) Crustal architecture beneath the southern Midcontinent (USA) and controls on Mesoproterozoic iron-oxide mineralization from 3D geophysical models. Ore Geol Rev 111:102966. https://doi.org/10.1016/j.oregeorev.2019.102966.

Rudnick RL, Gao S (2003) Composition of the continental crust. Treatise on Geochemistry 3:659-723.

Sullivan B, Locmelis M, Tunnell BN, Seeger C, Moroni M, Dare S, Mathur R, Schott T (2023) Genesis of the 1.45 Ga Kratz Spring Iron Oxide Apatite Deposit Complex in Southeast Missouri, USA: Constraints from Oxide Mineral Chemistry. Econ Geol in press.

Tunnell BN, Locmelis M, Seeger C, Mathur R, Dunkl I, Sullivan B, Lori L (2021) The Pilot Knob Iron Ore Deposits in Southeast Missouri: A High-To-Low Temperature Magmatic-Hydrothermal Continuum. Ore Geol Rev 131:103973. https://doi.org/10.1016/j.oregeorev.2020.103973.

Tunnell BN, Locmelis M, Seeger C, Moroni M, Dare S, Mathur R, Sullivan B (2022) The Shepherd Mountain iron ore deposit in Southeast Missouri, USA – An extension of the Pilot Knob magmatic-hydrothermal ore system: Evidence from iron oxide chemistry. Ore Geol Rev 141:104633. https://doi.org/10.1016/j.oregeorev.2021.104633.

Assessing silicate-liquid immiscibility using trace element in titanomagnetite and ilmenite in the Raftsund intrusion, Lofoten-Vesteraalen AMCG suite, Northern Norway

Nolwenn Coint, Eduardo Mansur, Jakob K. Keiding
[1]*Geological Survey of Norway (NGU), Leiv Eirikssons vei 39, 7040 Trondheim, Norway*
[2]*Geological Survey of Denmark (GEUS), Øster Voldgade 10, 1350 Copenhagen, Denmark*

Abstract. Magmatic processes responsible for the formation of Fe-Ti-P-rich rocks and nelsonites remain contentious. Fractional crystallization coupled with crystal sorting, magma mixing, and silicate-liquid immiscibility are the three processes considered. The two first processes are relatively well understood and testable, whereas the third one remains difficult to assess, especially in intrusive systems where melt compositions are rarely preserved. This study uses trace element in titanomagnetite and ilmenite to test these processes in the Raftsund intrusion, Northern Norway, where the role of silicate-liquid immiscibility has already been demonstrated. The Raftsund intrusion, composed mainly of monzonite and syenite, contains Fe-Ti-P-rich rocks and nelsonite occurrences. Ilmenite and titanomagnetite from the occurrences show enrichments in elements that behave compatibly and incompatibly in fractionating monzodioritic systems (e.g. Sc, V, Mn, Zn, Zr, Hf), compared to the same mineral in the host monzonite and syenite. The trace element behaviour in Fe-Ti oxides, combined with field observation and textural evidence of the presence of two separate melts, suggests that silicate-liquid immiscibility played an important role in the formation of the Fe-Ti-P-rich rocks in the Raftsund intrusion.

1 Geological setting

The Raftsund intrusion, a 75 by 35 km large monzonitic to syenitic batholith, was emplaced at 1800 Ma as part of the Lofoten-Vesteraalen Anorthosite-Mangerite-Charnockite-Granite (AMCG) suite.

While such suites are usually characterized by the presence of massif anorthosite, the Lofoten-Vesterålen AMCG one is composed of large volumes of monzonite and syenite, whereas gabbro and anorthosite are subordinate.

The two main anorthosite intrusions, Eidsfjord and Flakstadœy, show evidence of polybaric crystallization from 9 to 4 kbar, whereas monzonites and syenites crystallized at 4 kbar (Markl and Frost, 1998). Temperature estimates using the QUILF equilibria reach 925 C for the monzonite, oxygen fugacity was -0.6 below the FMQ buffer, while the silica activity was around 1.

The Raftsund intrusion is the most voluminous monzonitic intrusion of the AMCG suite and contains occurrences of Fe-Ti-P-rich rocks and nelsonite.

2 Raftsund intrusion

2.1 Type II monzonite

The Raftsund intrusion can be subdivided in three units based on textural observation. In this study we focus on the medium-grained equigranular type-II unit.

This unit can be further subdivided into an inverted pigeonite-augite syenite (Pgt-Aug syenite), cropping out in the north and a fayalite-augite monzonite (Fay-Aug monzonite) in the south. The contact between the two has not been observed in the field but seem to occur gradually in a zone where orthopyroxene and augite characterize the mineral assemblage instead of inverted pigeonite or fayalite. Evidence of mingling between type II and type III monzonite is preserved in the centre of the intrusion.

The Pgt-Aug syenite is composed of subhedral ternary feldspars, inverted pigeonite and augite (Mg#:51-57). Biotite and hornblende are late phases. Accessory minerals consist of titanomagnetite, ilmenite, apatite and zircon.

The Fay-Aug monzonite is characterized by subhedral ternary feldspar and Fe-rich mineral clusters composed of subhedral fayalite (Fo17-8.3), augite (Mg#:38-18), ilmenite and rare titanomagnetite. Apatite, locally abundant zircon, and allanite are accessory phases.

2.2 Associated Fe-Ti-P-rich rocks occurrences

Fe-Ti-P-rich rocks, associated with the Pgt-Aug syenite occur as scattered lenses which can reach up to 120 x 50 m. They consist of inverted pigeonite of subhedral Fe-rich olivine (Fo22–29), augite (Augite M#: 29-65), surrounded by interstitial titanomagnetite and ilmenite containing abundant apatite inclusions. Hornblende and biotite are minor interstitial phases. Resorbed ternary feldspar are abundant close to the contact between the host-syenite but are absent in the center of the largest Fe-Ti-P-rich rock lenses. Thin µm-scale plagioclase rims are locally preserved at the contact between resorbed ternary feldspar and the Fe-rich minerals. The contact between the Fe-Ti-P-rich rocks is sharp but curved attesting to the syn-magmatic nature of the mineralizations.

Fe-Ti-P-rich rocks from the Fay-Aug monzonite are limited to the mingling zone between the type II and type III monzonite. Centimeter-thick Fe-Ti-P-rich-rocks presenting a similar mineral assemblage as

the Fe-rich clusters in the host monzonite occur at the border of the type-III monzonite enclaves.
Nelsonite bodies are located towards the southwestern part of the intrusion and are hosted by the Fay-Aug monzonite. The sole location visited for this study, is a 15 by 20 m-lage massive nelsonite lenses. The contact between the nelsonite and the surrounding monzodiorite and monzonite can be sharp and lobate or gradational like in a mingling zone (Fig. 1). The nelsonite consists of titanomagnetite, ilmenite, subhedral apatite, mm-size resorbed zircon crystals and subordinate Fe-rich silicates (Fig. 1).

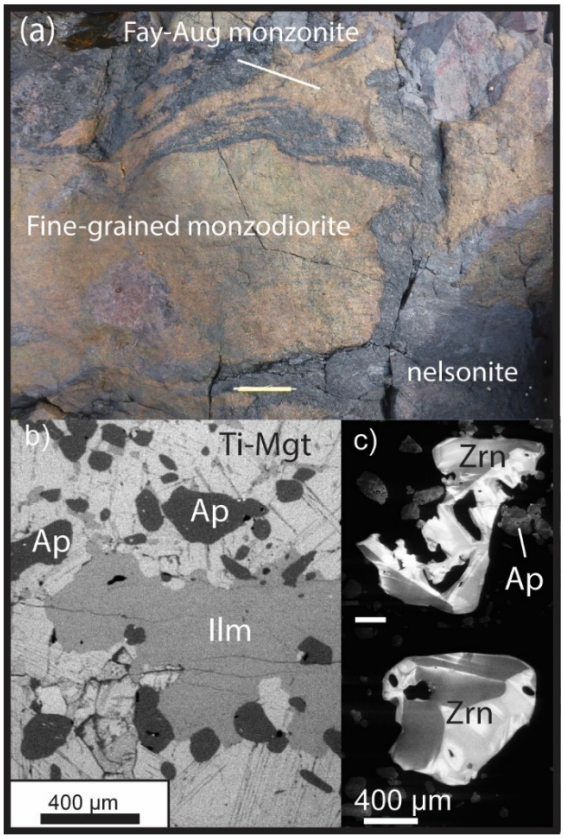

Figure 1. Nelsonite occurrence in the Fay-Aug monzonite. a. Contact between the nelsonite and the surrounding monzonite and monzodiorite. b. Mineral assemblage of the nelsonite. c. Resorbed zircon crystals.

3 Geochemistry

3.1 Whole-rock data

Whole-rock geochemistry indicate that Fe-Ti-P-rich rocks associated with the Pgt-Aug syenite have composition reaching up to 50 wt.% $Fe_2O_3^{tot}$, 9 wt.% TiO_2 and 6 wt.% P_2O_5. They are enriched in compatible elements such as Sc, V, Co but also in incompatible elements such as REE and to a lesser extend HFSE, compared to the host syenite.
Centimetre-thick Fe-Ti-P-rich rocks in the Fay-Aug monzonite are difficult to analyse because of their reduced size, but based on their mineral assemblages (abundant apatite and zircon), they clearly are enriched in REE and HFSE compared to the host monzonite.
The nelsonite, which contains only 3 wt% SiO_2 but in contrast >70 wt% Fe_2O_3tot, 15 wt% TiO_2 and 2.8 wt% P_2O_5 is characterized by similar but more pronounced enrichments relative to the Fe-Ti-P-rich rocks.
These elements are predicted to concentrate in an Fe-rich melt formed by silicate liquid-immiscibility (e.g. Charlier and Grove, 2012; Veksler and Charlier, 2015) but can, however, often not be observed in whole-rock data because whole-rock compositions in cumulates are affected by extensive accumulation and thus rarely represent melt compositions. An alternative method to test silicate-liquid immiscibility is to analyze the minerals which composition is controlled by the chemistry of the conjugate immiscible melts.

3.2 Trace element record of Ilmenite and titanomagnetite

Titanomagnetite and ilmenite from the Fe-Ti-P-rich rocks associated with Pgt-Aug syenite are enriched in Mg, Al, Sc, Zn and Mn and V compared to the one in the host syenite (Fig. 2). In addition, ilmenite is enriched in Hf and Zr, elements more compatible in the latter mineral than in titanomagnetite.

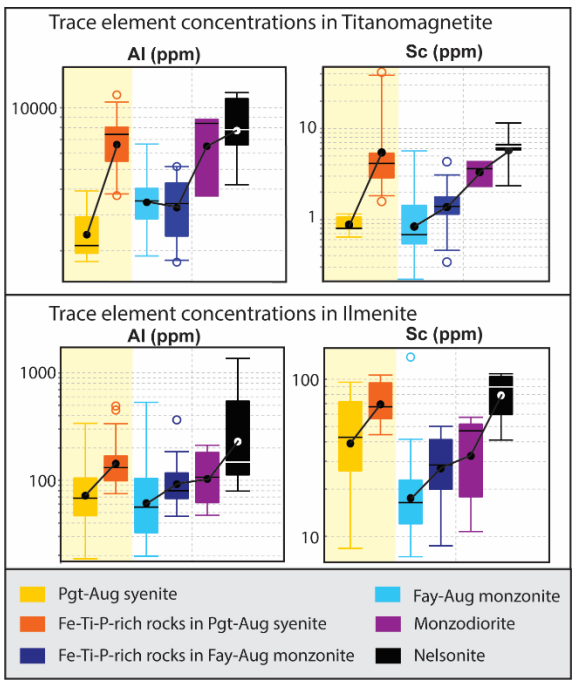

Figure 2. Variations of trace element concentration in titanomagnetite and ilmenite from the various investigated units.

Such enrichments in the Fe-Ti oxides from the Fe-Ti-P-rich rocks associated with the syenite and the nelsonite support that neither fractional crystallization nor magma mixing can explain the mineral record. Instead, they favour silicate-liquid immiscibility where they would result from the

crystallization of an Fe-rich melt enriched in numerous elements such as Mg. Furthermore, high concentrations of Sc and Al in both Fe-Ti oxide phases are consistent with crystallization from a melt enriched in Sc, despite the crystallization of augite, but where feldspar was not stable.

It is worth noticing however that Fe-Ti oxides from the Fe-Ti-P-rich rocks associated with the Fay-Aug monzonite do not record such enrichments. In this unit, Fe-rich mineral clusters, found scattered in the monzonite are thought to result from silicate-liquid immiscibility (Coint et al., 2020). The centimetre-thick veins are therefore best explained by the simple ponding of Fe-rich droplets at the contact with the type III monzonite.

The trace element record of Fe-Ti oxides from the nelsonite, showing enrichments in Al, Sc but also Mg and Mn, similar to the ones observed in Fe-Ti-P-rich rocks, indicate that silicate-liquid immiscibility is also involved in the formation of nelsonite in the Raftsund intrusion. The lack of lower temperature hydrous minerals precludes an important influence of hydrothermal fluids.

The transition between an Fe-rich melt presumably containing at least 30 wt.% SiO_2 and the formation of the nelsonite remains unclear. Segregation between the Fe-silicates and Fe-Ti-oxides, apatite and zircon upon fractional crystallization is a likely explanation, however it is not supported by experiments, often performs on systems of different compositions.

4 Conclusions

Fe-Ti-P-rich rocks associated with monzonites and syenites from the Raftsund are best explained as the product of silicate-liquid immiscibility, as summarized in figure 3. These results indicate that the process can influence thoroughly the evolution of dry and hot magmas of intermediate to felsic composition.

The process can be assessed by looking for evidence of textural disequilibrium between the minerals in the monzonite or syenite, and associated Fe-Ti-P-rich rocks and/or nelsonite.

The trace element record of minerals such as ilmenite and titanomagnetite can be used as an important tool to identify and unravel magmatic processes including ore formation. Specifically, in this case, Fe-Ti oxides trace element record attest to the important role of liquid-immiscibility in the genesis of nelsonite.

The transition between Fe-Ti-P-rich rocks and a nelsonite, however, remains poorly understood and require further experiments with appropriate composition and intrinsic variables.

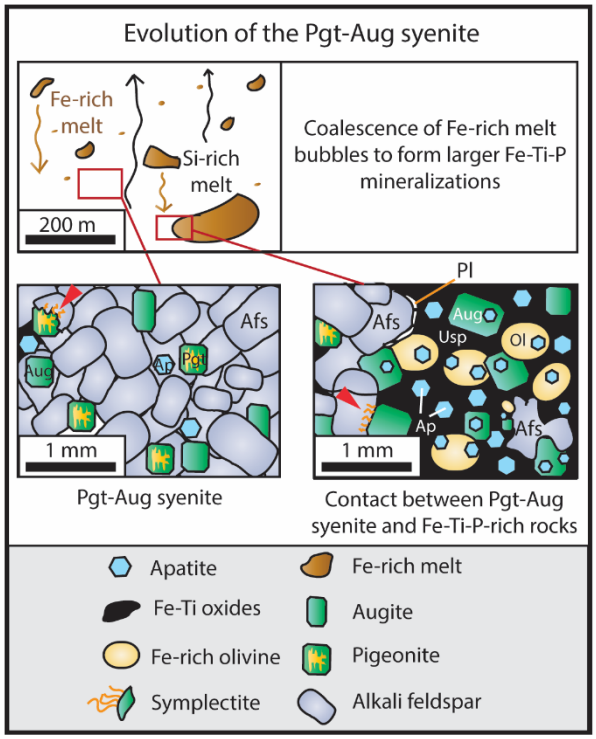

Figure 3. Petrogenesis of Fe-Ti-P-rich rocks associated with the Pgt-Aug syenite (from Coint et al., 2020)

Acknowledgements

The authors are grateful for the assistance of the lab at the Geological Survey of Norway, where most analyses were conducted and to Kristian Drivenes (NTNU, Trondheim, Norway) and Jessica Langlade (IFREMER, Brest, France) who helped with the microprobe analysis.

The Research Council of Norway is acknowledged for the support to the Norwegian Laboratory for Mineral and Materials Characterisation, MiMaC, project number 269842/F50.

References

Charlier, B and Grove TL (2012). "Experiments on liquid immiscibility along tholeiitic liquid lines of descent." Contributions to Mineralogy and Petrology **164**: 27–44. doi.10.1007/s00410-012-0723-y

Coint, N, Keiding JK and Ihlen PM (2020) Evidence for Silicate–Liquid Immiscibility in Monzonites and Petrogenesis of Associated Fe–Ti–P-rich rocks: Example from the Raftsund Intrusion, Lofoten, Northern Norway. Journal of Petrology **61**(4) https://doi.org/10.1093/petrology/egaa045

Markl, G, Frost, RB, and Bucher K (1998). The origin of anorthosites and related rocks from the Lofoten Islands, Northern Norway: I. Field relations and estimation of intrinsic variables. Journal of Petrology **39**(8): 1425-1452.

Veksler, IV and Charlier B (2015). Silicate Liquid Immiscibility in Layered Intrusions. Layered intrusions. Charlier B, Namur O, Latypov R and Tegner C, Springer Geology (eds.), Layered Intrusions: 229-258. https://doi.org/10.1007/978-94-017-9652-1_5

Genesis of iron ore deposit at Ga-Nchabeleng area.

Julia M. Maponya[1], Humbulani R. Mundalamo[1], Jason S. Ogola[1]
[1]Department of Earth Sciences, University of Venda, South Africa.

Abstract. The study area falls within the Sekhukhune District Municipality in Limpopo province. It is situated near the contact between the Bushveld Igneous Complex and the Transvaal Group sedimentary rocks. The aim of the study was to establish the mode of occurrence and origin of iron ore deposits at Ga-Nchabeleng area. The outcrops of the iron ore cover mainly the four hills with the host rocks forming mainly contacts between the iron ore. The geological mapping was conducted along traverses drawn across the general strike of the lithology. Iron ore and host rock samples were collected at an exposed area within and around four hills. Ore sampling was done following the trend of the ore deposits. Collected rock and iron samples were physically and geochemically characterised and X-ray fluorescence spectrometry method was used for selected samples for geochemical characterisation.

1 Introduction

Iron ore is a rock from which metallic iron can be extracted from. Iron is the most common element in the world and makes up close to 5% of the Earth's crust. Iron ore that contains a high quality of hematite or magnetite are known as "natural ore" and they can be entered directly into blast furnaces that produce iron. It has been argued that iron ore is the most important commodity in the global economy except for perhaps oil (www.softschools.com/facts/rocks/iron_ore_facts/2986/) . Iron ore is an important commodity because it is the primary source of iron, the metal most used by man. The most common gangue minerals in iron ores are quartz, feldspar, calcite, dolomite, clays, and carbonaceous matters. Ore deposits are natural concentrations of different metals in a wide range of geological settings, such as sedimentary, metamorphic, hydrothermal, and magmatic formations. The exploration of new deposits, and knowledge about their formation is crucial to today's society.

The Rustenburg Layered Suite which represents the Bushveld Igneous Complex in this region, consists of several igneous rock types varying from dunite and pyroxenite to norite, gabbro, anorthosite (Johnson et al 2009). The Ga-Nchabeleng area is characterised with hills of iron ore separated with granitic rocks in between. Consequently, the study focused on the characterisation of the host rocks samples to understand the mode and origin of the iron ore within the study area. This paper focuses on the genesis of the iron ore deposit at Ga-Nchabeleng area. To achieve more certainty about the formation of the Ga-Nchabeleng iron ore deposit, natural samples from the area were investigated as a case study with various petrological and geochemical methods. It lies in the south-eastern part of the Limpopo province, bordering on the Capricorn and Second Mopani Districts in the north, Mpumalanga province on Nkangala and Ehlanzeni Districts in the south a and east, and the Waterberg District in the west.

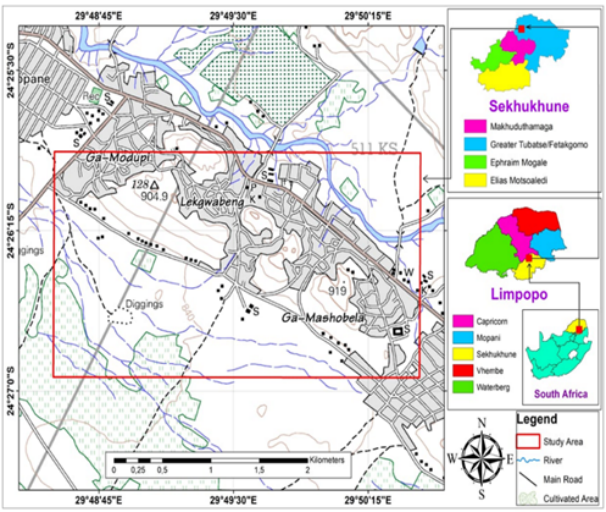

Figure 1. Location of the study area ArcGIS (2019).

2 Methodology

Fieldwork involved the collection of geological data in the study area. During fieldwork, geological field mapping, ore and rock sampling was carried out. The information required include identification of types of rocks, their location altitudes, and their structural features. The equipment which were used during fieldwork included; tape measure which was used to measure the thickness and the length of the outcrops, geological and sledgehammer were used for collection of specimens, hand lens was used as a magnifier for mineralogical identification in the fields, sample bags, clino-ruler, GPS was used to take coordinates of the sampling points, base map, map tube, clip board, permanent marker, crayons, tracing paper, field book and pens.

2.1 Geological field mapping.

The main objective of carrying out geological field mapping was to come up with a detailed geological map and to identify lithologies that host iron ore deposit. The study area was demarcated into an area of 1.8 km by 2.4 km. The demarcated area was divided into four traverses of 600 m each cutting across the lithologies in Figure 2. The GPS was used in the field for location purposes in the field in relation to the base-map and compass was used to show direction. The compass was also used to measure attitudes of lithologies while the GPS was used to record the location of outcrops. The geological and sledgehammer were used to break the fresh sample from the outcrop. Then rock samples were numbered according to the traverse,

position which they are found at, using permanent marker.

During the geological field mapping, the description of texture and minerology of the rock specimens was done with an aid of a hand lens and recorded in a notebook. The contact between the rock outcrop and geological structures were recorded in a notebook and photographed for later referencing when compiling a geological map of the study area.

2.2 Sampling

A total of 58 samples of rock specimen and ore were collected during the field mapping for rock identification, petrographic study, and geochemical analysis. About 2 kg of fresh specimens and ore samples were collected for laboratory work. The rock specimen was collected for further laboratory analysis using petrographic study and whole-rock microscopy. Data collected from the geological field mapping was used to compile a geological map of the area as well as a cross-section.

The study area was divided into four hills, the hills were identified based on the availability of iron ore. The sampling points of each hill are represented on Figure 3 a to d. A permanent marker was used to mark the samples during sampling, and the sample was then stored in a sample bag. The samples were also collected from contacts of host rocks and veins filled with magnetite.

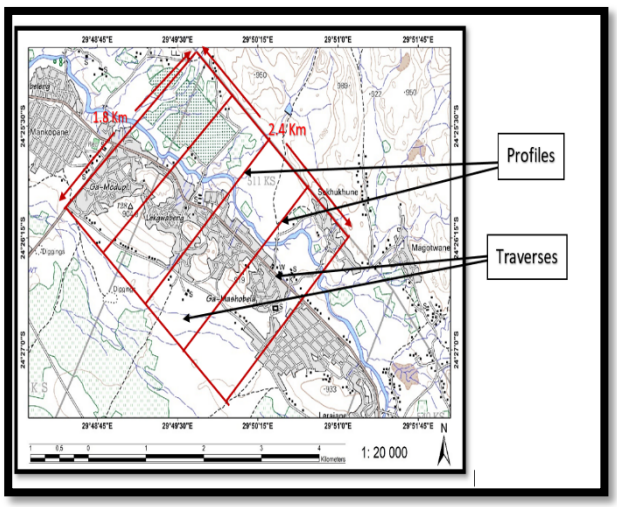

Figure 2. Map indicating the traverses that were mapped in the study area Google Earth (2019).

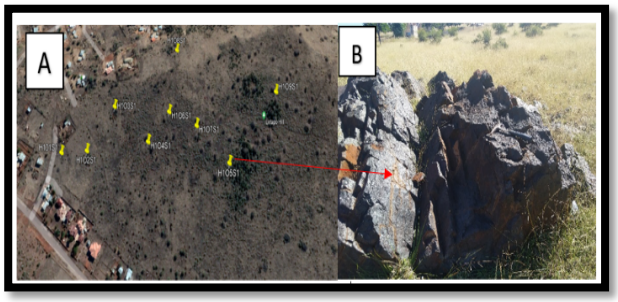

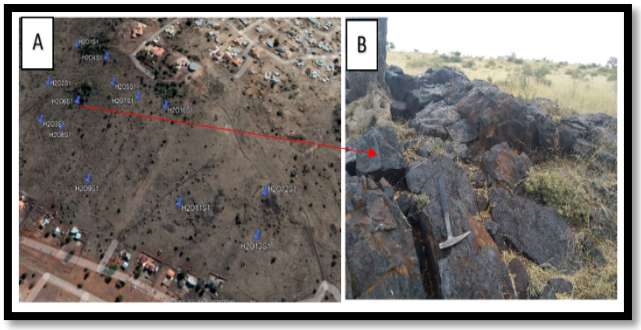

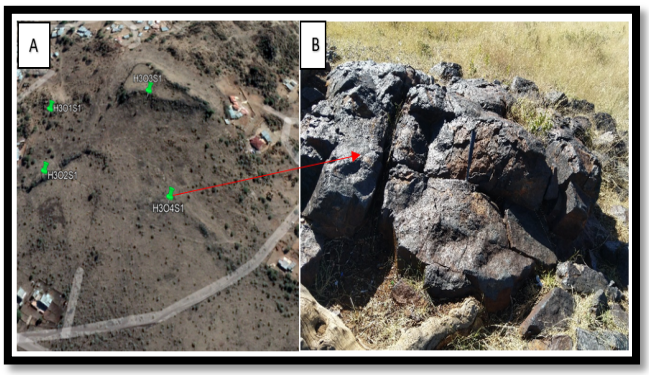

Figure 3. a Sampling points of iron ore: A-Hill 1; and B-Outcrop in Hill 1. **b** Sampling points of iron ore: A- Hill 2; and B-Outcrop in Hill 2**. c** Sampling points of iron ore: A-Hill 3; and B-Outcrop in Hill 3. **d** Sampling points of iron ore: A- Hill 4; and B-Outcrop in Hill 4.

2.3 Laboratory work

Laboratory work involved rock identification, petrographic studies, and X-ray florescence. This was done to gain information on the physical and chemical characteristics of iron ore and rock samples collected from the study area. Thirteen samples were dried for 12 hours in the Vacutec drying oven at 330°C to release any moisture before milling to avoid the jamming of the milling pots. Samples were milled using the Restch RS 200 milling machine on manual operation mode for 5 minutes to particle size of about 75 µm. Milling pots were cleaned using quartz to prevent contamination before analysis, the pots were cleaned to ensure that quartz will not affect the SiO2 content of the sample during analysis.

The samples were pelletized by adding the sample into a pallet cup and using boric acid powder as a binding agent and acetone to prevent cross

contamination of samples. Pulverized sample powder was then pressed with about 3 grams of boric acid. The pellet cup was placed on the manual hydraulic press and a force of 30 tons was applied for 30 seconds. Once the pallet is ready was removed from the die-set and placed in a container with label indicating sample number and then ready for X-Ray Fluorescence spectrometry analysis.

3 Findings of the Current study

On the current study, the mode of occurrence and genesis of Ga-Nchabeleng iron ore deposit has been studied. The geological processes that are responsible for ore mineralization and genesis of the Ga-Nchabeleng iron ore deposits has been studied. The distribution of the iron ore at Ga-Nchabeleng area revealed the stock-work - stringers - finger-like structures wherein geologic structures such as veins acted as conduits. Several lithologies were identified that included varieties of gabbronorite and an iron ore magnetite. Mineralization occurred along micro-fractures which resulted in ore stockworks. The bulk chemical composition of magnetite samples revealed the occurrence of the following major oxides: SiO2, Al2O3, Fe2O3, MgO, CaO and Na2O as well as minor oxides of TiO2, MnO, K2O and P2O5 in Figure 4. The Ga-Nchabeleng iron ore was dominated by the presence of TiO2, Al2O3 and Fe2O3 with average of 24.16%, 7.69% and 52.36% respectively. TiO2, Fe2O3 and SiO2 were the most abundant oxides at Ga-Nchabeleng area this enrichment can be corroborated by the prevalence of quartz minerals and hematite in the iron noted in petrographic study of iron ore. Hill three was the one with high content iron oxides, and this concludes that it was the one with rich magnetite at 55.56%.

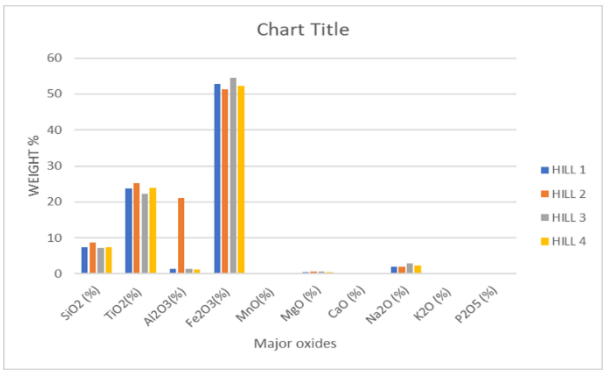

Figure 5. Major oxides average of 4 hills.

4 Genetic Model of Ga-Nchabeleng iron ore deposit.

Genesis of ore deposits is very complex, and researchers tend to change the origin of the source material so that it can match the depositional environment of the deposits (Mundalamo 2019). Iron forms under different conditions which may range from magmatic to metamorphic. The Ga-Nchabeleng iron ore deposit is an example of ore that was formed during the magmatic eruption. A genetic model is there to show an order of information describing how a mineral deposit was formed. It also describes different attributes and factors which contributed to the formation even though their relationship is not known. There are aspects which are required for a genetic model; it must be clear and open to allow new types of deposits in the future and the model must be appropriate to the rock and the environment being investigated (Mundalamo 2019).

Mode of occurrence can be used as the first aspect when trying to identify a genetic model. The genetic concepts are used to help in knowing how the ore was formed based on site-specific concepts. The Ga-Nchabeleng iron ore deposit is of epigenetic in nature because the orebodies were localized along the fault planes and around the igneous rocks namely gabbronorite. Geological structures also help in the formation of ore deposits because they give direction of ore occurrence. Fractures in the area suggest that faults acted as a way for magma to erupt on the ground that finally resulted in the localized iron ore deposit. There was a direct crystallization of Fe-rich melt separated from a parent silica magma. The ore occurred as veins and disseminated orebodies which suggest that mineralization took place along microfractures which resulted in stockworks. The Ga-Nchabeleng orebody was formed during magmatic segregation which involved the separation of an immiscible Fe-P-rich melt from a silicate melt with the subsequent intrusion and crystallization of an Fe-rich ore body at upper crustal level. The ore contains a very pure magnetite, containing more than 50% iron. The mineralized solution originated from magma as shown in Figure 5.

This was supported by the fact ore minerology, ore microscopy, and the geochemical results of the area. The iron ore composed entirely of magnetite and less content of hematite. It also had a high amount of vanadium and titanium oxide which is evidence of magmatic origin.

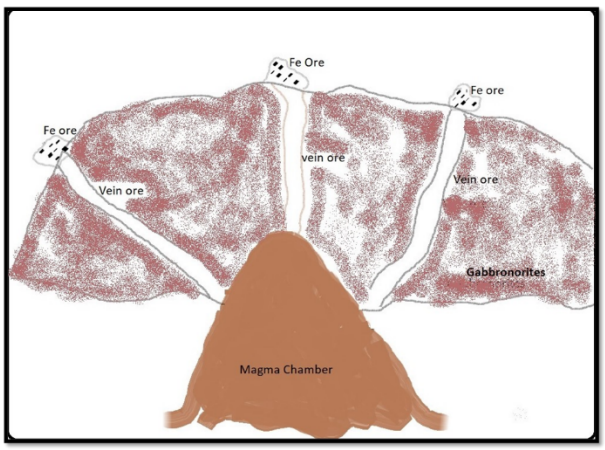

Figure 5. Genetic model of the Ga-Nchabeleng Iron ore deposit.

5 Conclusions

A detailed geological map of Ga-Nchabeleng area was produced and the following rock is associated with Iron ore; Dark and light Gabbronorite. These rocks strike to the north-west. These rocks are not associated with any other rock type in their occurrence and some are far away from the magnetite ore. Iron ore at Ga-Nchabeleng area was formed during magmatic eruption and crystallization of magma. This is further corroborated by the presence of rocks associated with magma such as Gabbronorite.

The rock is associated with rock forming minerals and have high content of iron oxide. The study concluded that the iron ore is hosted by intermediate to felsic igneous rocks which were found to be gabbronorite and the magnetite ore formed stringers zones that were randomly oriented veins associated with fractional crystallization of the layered complexes.

Acknowledgements

DSI-NRF CIMERA for funding the project and all other guidance. University of Pretoria for the analysis of samples for the geochemical results. My supervisors for support and patience throughout the project.

References

Jonsson, E., Troll, V.R., Högdahl, K., Harris, C., Weis, F., Nilsson, K.P. and Skelton, A., (2013): Magmatic origin of giant 'Kiruna-type'apatite-iron-oxide ores in Central Sweden. Scientific reports, 3, p.1644

Google earth V 6.2.2.6613. (2019). Digital Globe 2012. http://www.earth.google.com [April 30, 2019].

Insights into IOA and IOCG deposit genesis from comparative isotopic analysis of Fe and Cu isotope compositions in magnetite and ores

Ryan Mathur[1], Michael Di Maio[2], Linda Godfrey[2], Adam C. Simon[3], Chris Emproto[3], Vladamir Lisitsin[4], Courtney Dhnaram[4], Ioan Sanislav[5], Irene del Real[6]

[1] *Geology Department, Juniata College, Huntingdon PA U.S.A.*
[2] *Department of Earth and Planetary Sciences, Rutgers University, U.S.A.*
[3] *Department of Earth & Environmental Sciences, University of Michigan, Michigan, U.S.A.*
[4]. *Geological Survey of Queensland, Brisbane, Australia*
[5]. *Earth and Environmental Science, James Cook University, Townsville Australia*
[6]. *Department of Geology, Universidad Austral* de Chile*, Chile*

Abstract.
Transition metal isotope compositions of ores from IOA and IOCG deposits compared to each other as well as other deposit types provides insight into mechanisms of ore deposit formation. In this contribution, we provide new Fe isotope data from classic IOAs in Bafq, Iran, several Fe-oxide apatite deposits in New Jersey and compare them to data in the literature. Clearly, IOAs have tighter ranges of values than IOCGs and higher mean values which could indicate magmatic /orthomagmatic versus hydrothermal processes that operated in each deposit type respectively. New copper isotope data from chalcopyrite in IOCGs from Candelaria, Ernst Henry, Jericho, and Mina Justa show an identical range to porphyry copper deposits and have a lower mean value to porphyry copper sulfides Figure 2. Sed Ex copper deposits and VMS have larger ranges and higher means values as well. Potential interpretations for these distinct differences in copper isotope compositions could range from ligand transport mechanism to different copper sources. Constraining sources for the ores can difficult given overlapping values of crustal and mantle sources (figure 2). The comparative analysis presented show the importance of metal isotope analysis and how direct information can be obtained to metal transport and ore genesis through study of the isotopes of the metal commodities.

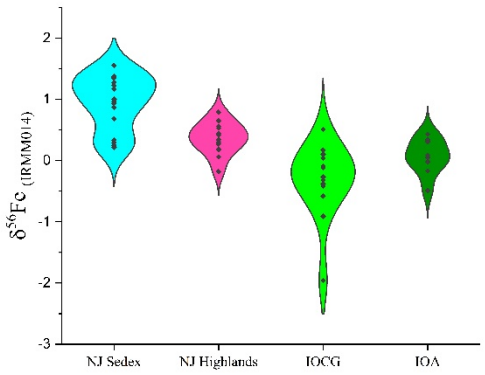

Figure 1- Fe isotope data presented here and from the literature from magnetite.

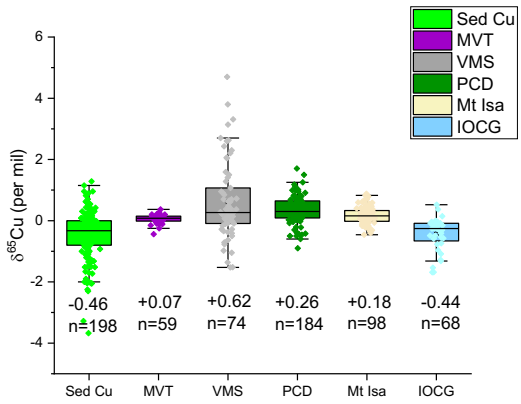

Figure 2- Copper isotope comparison of chalcopyrite from major ore deposit types, data presented here and taken from the literature. Data reported relative to NIST 976.

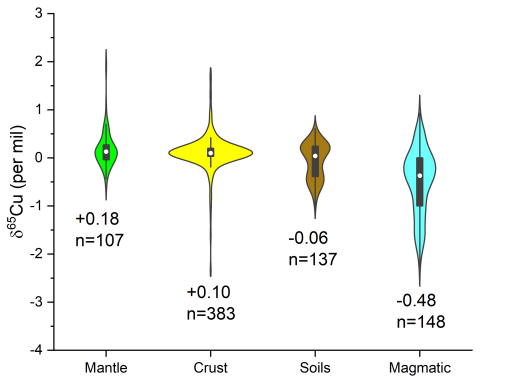

Figure 3- Summary of copper isotope data of geological materials, data taken from the literature. Data reported relative to NIST 976.

Controls on iron oxide-Cu-Au mineralisation: dogma versus data

Tobias U. Schlegel, Weihua Liu, Helen B. McFarlane, Renee Birchall, and James R. Austin
CSIRO Mineral Resources, Australia

Abstract. The shear zone hosted Starra-276 IOCG deposit shows high Au/Cu ratios combined with high Cu ore grades. Zoning in gold, copper and Cu sulphides corresponds to a transition from hematite–quartz–carbonate ironstones and breccias to magnetite (±hematite)–quartz–chlorite–muscovite–carbonate altered rocks. Systematically collected, SEM-based modal mineralogy, structural information from measurements of the anisotropy of magnetic susceptibility in combination with thermodynamic alteration calculations enable a consistent model for IOCG ore formation in which hydrolytic alteration and in particular the fluid-rock ratios during alteration exert control on the zoning of principal alteration minerals and the distribution of gold, copper and Cu sulphides in the deposit. Hematite–quartz ± carbonate ± barite ironstones and breccias form simultaneously with the precipitation of gold and native copper via acidic fluid-neutralisation in hydrothermal alteration regimes characterised by increasing fluid-rock ratios because intense hydrolytic alteration produces new porosity. Copper sulphides precipitate in areas of lower fluid-rock ratio showing aluminosilicate-stable hydrothermally altered rocks. The zonation in Au–Cu–chalcocite–bornite–chalcopyrite–pyrite is the result of a low-T, very acidic, SO_4-bearing ore fluid. Our alteration models involving Fe-Na-K-Cl-rich and CO_2–H_2S-bearing brines failed to reproduce ore mineral assemblages.

1 Introduction

Iron oxide-copper-gold (IOCG) deposits are characterised by a system-scale alteration mineral zoning with some deposits showing distinct, yet unexplained, gross (or partial) zoning of economic elements and minerals from centre to margin Au–Cu–chalcocite–bornite–chalcopyrite–pyrite (e.g., at Olympic Dam, Ehrig et al. 2012) consistent with the transition from hematite–quartz ± carbonate ± barite breccias and ironstones to hematite/magnetite–aluminosilicate bearing breccias and ironstones. Although Cu–Au mineralisation has been interpreted to result from hydrothermal brecciation and genetically-related infill and veining, ore bodies typically form by host rock replacement and show spatial relations to faults, shear zones, unconformities, and breccias which led to the widely accepted, but weakly defined, interpretation that IOCG deposits are structurally controlled. The structures typically extend beyond the footprint of the deposit and are largely barren; thus, it is unlikely that they control the exact location of high-grade Cu-Au mineralization. The structures are thought to primarily act as fluid pathways allowing ore fluids to migrate from their source regions towards target areas where mineralisation is caused by alteration-related infill into rock pores, the breccia matrix, and by replacement of pyrite. Regardless of their importance for fluid flow and mineralisation, structures and neighbouring rocks represent locations of extreme contrasts in fluid-rock ratio (f/r). Importantly, the f/r exerts primary control on mineral stability at any given conditions during alteration and mineralisation (e.g., T, P, oxidation and sulfidation state, fluid conditions, Reed 1997). The Cloncurry METAL project characterised 1590 samples from 23 deposits and prospects across the Cloncurry district in Australia and resulted in a published integrated, geoscience dataset with data from 10 analytical techniques (Austin et al. 2021).

In this contribution, we focus on the Starra-276 shear zone hosted IOCG deposit and use modal mineralogy, structural data, and thermodynamic modelling to decipher the cause for the zoning in alteration, ore minerals (Figures 1 and 2) and explore the basis for high-grade Cu mineralisation (Figure 3). We test if the mineral zoning can be obtained by hydrothermal alteration reactions between host rocks and previously proposed ore-fluid compositions and conditions between 550°C and 200°C determined from fluid inclusions (Baker et al. 2008, Schlegel et al. 2018). Previous alteration studies conducted at Starra focused on mineral paragenesis, structural controls and described general relations among zones of alteration minerals (e.g. McFarlane et al. 2020), but insufficiently explained why the Starra-276 deposit shows many aspects of a quality IOCG deposit including high Au/Cu ratio paired with high Cu grades in ores. Together, several deposits along the Starra and related shear zones produced 11.4Mt @ 2.1% Cu and 3.2g/t Au between 1992 and 2002 (McGeough and Faulkner 2017).

2 Methodology

The mineralogy in samples from the Starra-276 deposit was determined using a scanning electron microscope (SEM), coupled with 3 EDAX energy dispersive X-ray spectroscopy (EDS) detectors and a backscatter electron (BSE) detector combined with a Tescan Integrated Mineral Analyser (TIMA) at the CSIRO in Perth, Australia. Standard electron beam alignment, focusing, and calibration of the detectors were conducted before each analytical run of up to 22 samples. The anisotropy of magnetic susceptibility (AMS) was determined from the same samples. The AMS defines an ellipsoid of the magnetic susceptibility of a rock. The technique reflects the grain shape of magnetite or the crystallographic-preferred orientation and alignment of Fe-bearing minerals, thus defining the magnetic fabric, allowing the calculation of a dominant

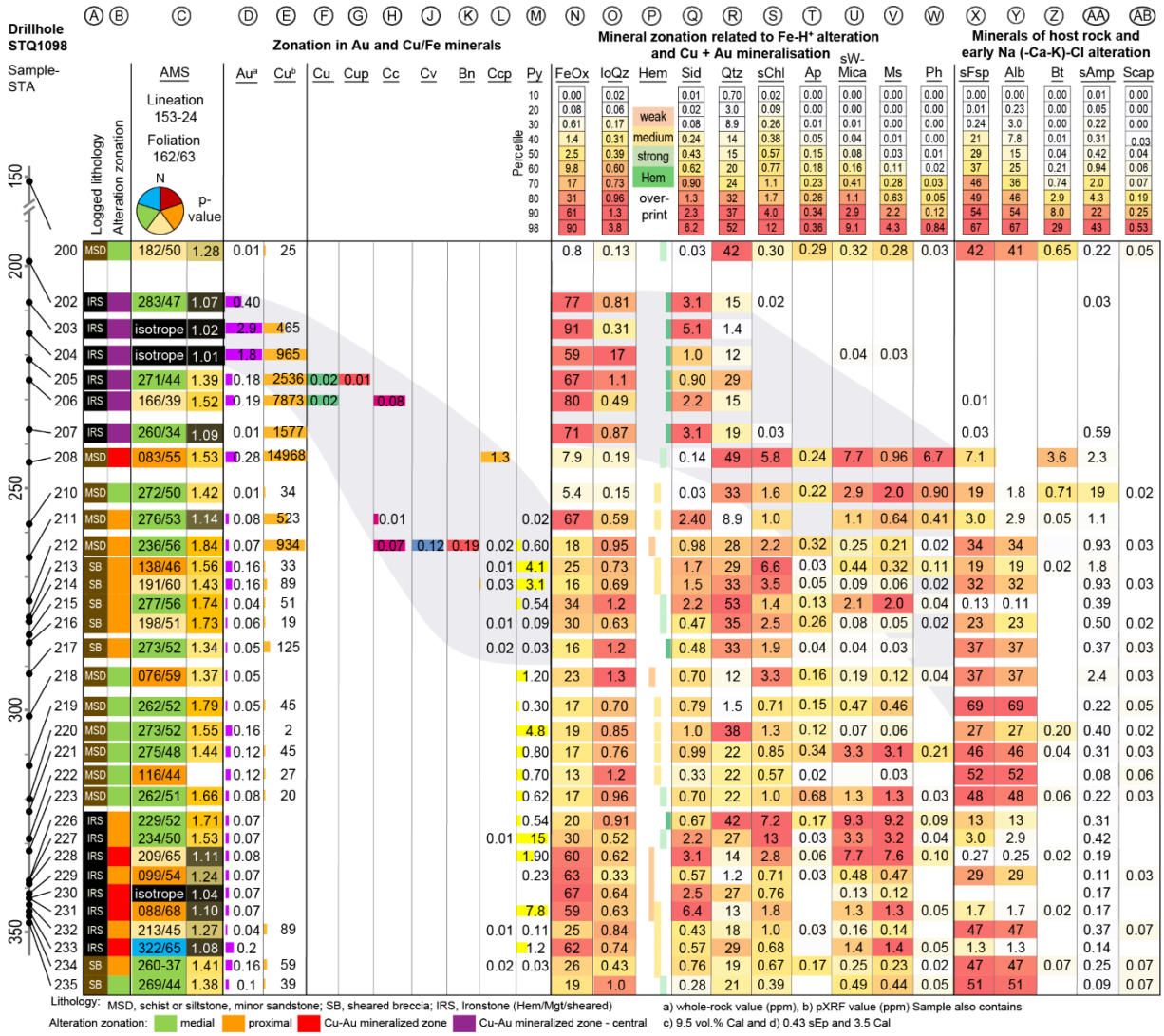

Figure 2. Downhole plot of samples from drill core STQ1095 showing (A–B) the lithology, alteration zonation, (C) AMS-structural data, and (D–AB) the relevant modal mineralogy in vol. %. The mineralogy of one sample is shown per row. A column represents a mineral or a group of minerals. A separate colour-code is used for each column (sFsp = Ab+Pl+Kfsp, sChl=Fe+Mg-chlorite etc). The colours represent percentiles of the entire dataset from the Starra deposit.

lineation or foliation in samples using the Anisoft software. Measurements were acquired using an AGICO Kappabridge magnetometer and yielded the relative intensity, declination, and inclination of the maximum (K1), intermediate (K2) and minimum (K3) principal susceptibilities, as well as the mean susceptibility. The degree of the magnetic anisotropy (P) is P=K1/K3. A rock with a high P value is highly anisotropic, thus shows a strong lineation or foliation whereas one with P≈1 is isotropic and does not show a magnetic fabric (e.g. Rochette et al., 1992). The HCh software (Shvarov, 2008) with a customised UNITHERM database containing thermodynamic parameters of solids, gases, and aqueous species was used for all thermodynamic calculations. Static closed system models were used to determine the alteration mineral assemblages related to changes in f/r.

3 Geology and mineral zoning

The Starra-276 ores are hosted in roughly N-S trending ironstone lenses (hematite and magnetite), quartz–ironstones, magnetite–chlorite/white mica ± biotite schists at the contact between sheared calcareous arenites and metasiltstones. The ores occur within or close to the Starra Shear (Figure 2). AMS results display two magnetic foliation orientations, an NNW striking/NW dipping, and an NNE striking/SSE dipping orientation. P-values systematically decrease, and dip orientations diverge as the drill core traverses from aluminosilicate stable schists- and sheared breccias into Au-Cu bearing, intensively altered quartz–ironstones suggesting that mineralisation-related alteration diminished and distorted the magnetic fabric, which was originally introduced during deformation (Figures 1, Columns A–C and 2A).This suggests that economic mineralisation-related hydrothermal alteration was perhaps synchronous with, but certainly outlasted shearing. The modal mineralogy reveals the gross zoning from centre to margin as Au–Cu–cuprite–chalcocite–covellite–bornite–chalcopyrite–pyrite/pyrrhotite (Figure 1, Columns D–M). Gold, native Cu, and cuprite are hosted within the core of the alteration system in

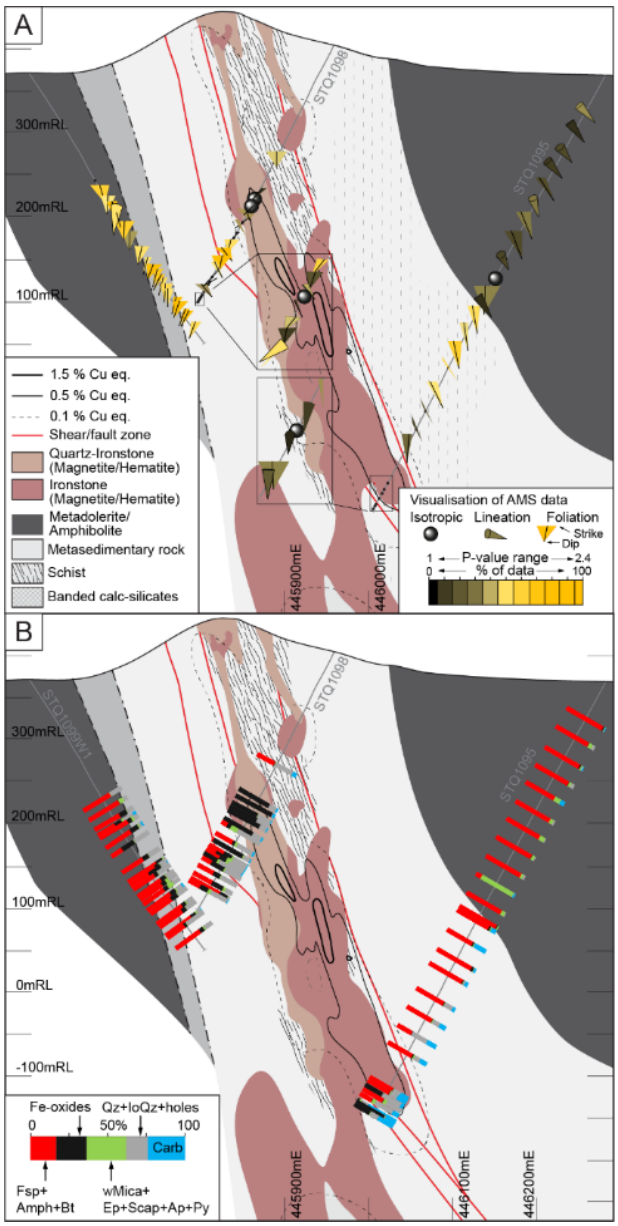

Figure 3. E–W trending cross-section across the Starra-276 deposit showing (A) AMS data and (B) the alteration zoning illustrated in 100% stacked bar mini-illustrations for each sample in relation to the Cu grades and simplified lithologies derived from company data.

intensively quartz–hematite ±carbonate (siderite, dolomite, calcite) altered, and aluminosilicate depleted, originally magnetite ironstones (Figure 1, Columns N–R). Chalcocite, covellite, and bornite formed at the transition between quartz–hematite–siderite ironstones and magnetite (±hematite)–quartz–chlorite–muscovite–carbonate ironstones (Figure 1, Columns E–W) whereas chalcopyrite is hosted in ironstones and magnetite–pyrite schists showing abundant chlorite and white mica which partially (or completely) replace feldspar, biotite, and amphibole bearing host rocks and early alteration minerals (Figure 1, Columns S–X). The zoning suggests that economic mineralisation was associated with H^+-CO_2 (hydrolytic) alteration. The high-grade ore zone is surrounded by sheared rocks affected by Fe(±K)-S alteration (magnetite-hematite-biotite–apatite–quartz–pyrite), which overprinted broad zones of Na-Ca altered host rocks (albite–actinolite–scapolite; Figure 1, Columns Y–AB). The dominant type of feldspar in the medial to distal alteration halo around the ore zone is albite but the type of feldspar is irrelevant because mineralisation-related hydrolytic alteration was feldspar-destructive (Figure 2B).

4 Thermodynamic calculations and interpretations

Hydrothermal alteration at Starra was modelled by reacting two fluid types A and B to a mineral assemblage, aiming to reproduce the ore mineral compositions at the Starra-276 deposit (Figure 1, Columns G–AA). Fluid A is a low salinity and at low-T very acidic, SO_4-bearing fluid containing 1000 ppm Cu (ore fluid A in Schlegel et al., 2018). Fluid B is a Fe–Na–K–Cl-rich, CO_2, H_2S, and Cu-bearing brine (fluid B with 100 ppm Cu and added CO_2, see Schlegel et al. 2018). The brine approximates the composition of one fluid inclusion for which Cl, K, Fe, Cu concentrations are available. In absence of more relevant compositional fluid inclusion data from Starra, thermodynamic models explored hydrothermal alteration conditions between 550 °C /2.5 kbar and 125 ˚C/P_{sat} representing the range of homogenisation temperatures of fluid inclusions from Starra (Baker at al., 2008). Both fluids reacted to a rock showing a mineral composition characteristic of the medial alteration footprint at the Starra-276 deposit (Figure 1). Alteration models at 200 °C involving fluid A reproduce the quartz–hematite–chlorite–muscovite ironstones and result in high Cu grades from chalcocite (~2.5 vol.%) at f/r between 25 and 60 (Figure 3A). Bornite (~1.2 vol.%) and chalcopyrite (~1.5 vol.%) form in quartz–magnetite/hematite–chlorite–muscovite ironstones and in magnetite/hematite–chlorite altered host rocks at f/r between about 3 and 12. The calculated mineral composition is consistent with the mineral abundance in the marginal ore zone. Cuprite formed at 125 °C in quartz–hematite–chlorite–muscovite ironstones, thus in rocks like sample STA205 (Figure 1). Addition of CO_2 to fluid A results is quartz–hematite–siderite–muscovite ironstones with chalcocite (~2 vol.%), bornite (~0.3 vol.%) and chalcopyrite (~0.6 vol.%) between f/r of 5 and 40. All models with fluid A resulted in IOCG-characteristic chalcocite–bornite–chalcopyrite–pyrite zoning (Figure 3A) and thus indicate that the mineral sequence develops due to a systematic decrease in fluid-rock ratio from the ore-fluid feeder zone to significantly more rock-dominant parts of the developing ore body and its alteration footprint (Figures 2 and 3A). Importantly, alteration models between 400 °C and 250 °C result in significant reduction of the rock volume (Figure 3B).

As a result, reactions between ore fluid A and the host rocks likely foster fluid-flow by enhancing the permeability of the shear zone due to increasingly connected rock-pores and may even by local

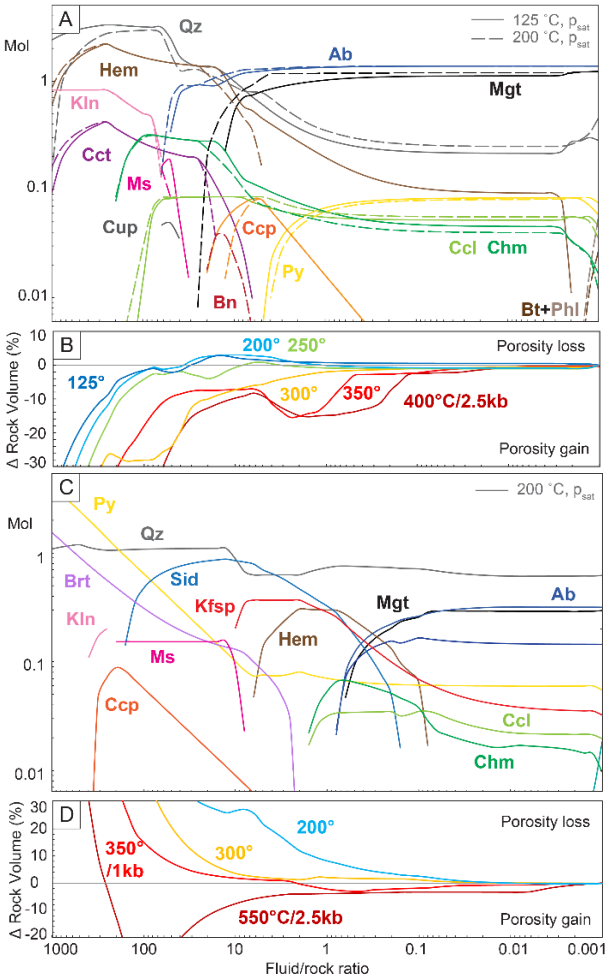

Figure 3. Static closed system models of alteration reactions between albite-magnetite schists and (A, B) the low salinity, ore fluid A, and (C, D) a Fe-Na-K-Cl-rich, CO_2-bearing brine B at variable T and P. Vertical concentration lines are not. Abscissa shows decreasing f/r ratios from left to right. (A, C) Alteration minerals in moles/kg of initial fluid. (B, D) Change of the rock volume. Mineral abb. Whitney and Evans (2010).

collapse brecciation. Alteration models between fluid B and the host rock at 500 °C/2.5 kbar and high f/r result quartz–magnetite–barite ironstones. Mineral assemblages including feldspars, diopside, and biotite/phlogopite form at low f/r. Cooling and decompression to about 200 °C/P_{sat} result in increasing amounts of pyrite, hematite, quartz, muscovite, and chalcopyrite at high f/r and in siderite, K-feldspar, chlorite-bearing rocks at low f/r (Figure 3C). Any of the models resulted in a composition like the quartz–hematite–siderite–chlorite–muscovite ironstone with sulphides as they occur in the ore zone (Figure 1), or in the characteristic Cu sulphide zoning. In addition, all but one model resulted in a large increase in rock volume at any f/r between about 0.1 and about 100 (Figure 3D). The alteration mineral assemblages would successfully clog ore-fluid flow in the Starra shear zone, or in any geologically reasonable structure, and thus inhibit economic Cu-Au mineralisation. For these reasons, the saline Fe–Na–K–Cl (±CO_2) rich fluid B alone is an implausible ore fluid. In contrast, fluid-rock reactions involving fluid B likely produce mineral assemblages like the ones observed in IOCG prospects containing subeconomic Cu grades.

5 Conclusions

The Au-Cu–cuprite–chalcocite–bornite–chalcopyrite–pyrite mineral zoning in IOCG deposits is controlled by changes in f/r ratio active during mineralisation and associated hydrolytic alteration. Gold-bearing, but Cu-barren quartz–hematite (±siderite±barite) ironstones and breccias develop where ore fluids enter the mineralising system. At the transition to chlorite–muscovite–feldspar bearing ironstones and breccias, which host the Cu ores, alteration reactions occur at lower f/r and Cu sulphides precipitate due to acidic-fluid neutralisation. Economic mineralisation involves at least one Cu-Au charged ore fluid A containing S as sulphate. The reactions of ore fluid A with the rocks previously modified by Na–Ca±Fe alteration foster ore-fluid infiltrations by changes in the porosity-permeability patterns within and adjacent to faults, shears, breccias, and unconformities. These structures exert control on regional to more local fluid flow but not necessarily on the location of economic mineralisation itself.

References

Austin JR, Stromberg J, Birchall R, et al (2021) The Cloncurry METAL Geodatabase mk1: A scale-integrated relational geodatabase for the Cloncurry District, Northwest Queensland. Part I: Cloncurry METAL Report 2018/21. CSIRO, Australia, 50p.

Baker T, Mustard R, Fu B, Williams PJ, et al (2008) Mixed messages in iron oxide-Cu-Au systems of the Cloncurry district, Australia: insights from PIXE analysis of halogens and copper in fluid inclusions, Min Dep 43:599–608.

Ehrig K, McPhie J, and Kamenetsky V (2012): Geology and mineralogical zonation of the Olympic Dam iron oxide Cu-U-Au-Ag deposit, South Australia, Econ Geol Spec Pub 19:237–267.

McFarlane HB, Austin JR, Schlegel TU, et al (2021) Starra 276: Redox Gradients and Structural controls: Integrated petrophysical, structural and mineralogical analysis: Part V: Cloncurry METAL Report 2018/2021 CSIRO, Australia, 58p.

McGeough MA, and Faulkner IL (2017) Selwyn mineral field, In Phillips GN (ed) Australian Ore Deposits, AusIMM, Melbourne, 864p.

Reed ME (1997) Hydrothermal alteration and its relationship to ore fluid composition, In Barnes HL, (ed) Geochemistry of hydrothermal ore deposits, 3rd edn, Whiley New York, pp 303–365.

Rochette P, Jackson M, and Aubourg C (1992) Rock magnetism and the interpretation of anisotropy of magnetic susceptibility, Rev of Geophys 30:20–226.

Schlegel TU, Wagner T, Wälle M, Heinrich CA (2018) Hematite breccia-hosted iron oxide copper-gold deposits require magmatic fluid components exposed to atmospheric oxidation: evidence from Prominent Hill, Gawler craton, Econ Geol 113:597–644.

Shvarov, YV (2008) HCh: New potentialities for the thermodynamic simulation of geochemical systems offered by windows, Geochemistry International 46: 834-839.

Characterization of the Kiskamavaara IOCG-(Co) deposit, northern Norrbotten, Sweden.

Iris van der Werf[1], Joel B. H. Andersson[1], Tobias E. Bauer[1] Thomas Kearney[2]
[1] Division of Geosciences, Luleå University of Technology, 97187 Luleå Sweden.
[2] Talga Group AB, Kungsgatan 5B, 972 35 Luleå

Abstract. This study presents new insights into the structural geometry and the distribution of cobalt in the Kiskamavaara IOCG-(Co) deposit which is located in the northern Norrbotten ore province in Sweden. The aim of the study is to determine the structural controls and cobalt distribution in the ore body along with establishing the correlation between Co-Cu mineralization in deposit scale by drill core logging, geophysical map interpretation, 3D modelling, and geochemical analyses. The results show that the host rock is composed of rhyolites/dacites, andesites and basalts that belong to the Porphyrite group. Most mineralization styles form the matrix of hydrothermal breccias of several generations and form three clusters that are situated at junctions between a first order shear zone and associated second order structures. Geochemical analyses show a weak correlation between cobalt and copper, especially at the mineralization margins, either indicating an evolving mineralization system, a multi-stage mineralization event or different mobilization behaviors during overprinting alteration events. Kiskamavaara as a case study has the potential to increase the understanding of the origin and evolution of cobalt in IOCG systems within Norrbotten and perhaps beyond.

1 Introduction

The Kiskamavaara ore deposit is classified as an iron oxide-copper-gold (IOCG) deposit and is located in northern Norrbotten, Sweden (Martinsson et al. 2011). The deposit is situated in the Karesuando–Arjeplog deformation zone (Fig. 1; KADZ; Bergman et al. 2001). However, recently Bauer and Andersson (2021) argue for a SSE deflection of the crustal shear zone into the Nautanen deformation zone (NDZ), which also hosts the Nautanen IOCG- and the Aitik porphyry Cu-Au-Ag deposits.

The Kiskamavaara deposit was discovered by the Swedish Geological Survey (SGU) during a drilling campaign between 1972-1980 (Persson 1980). The Fe, Cu and Au mineralization is hosted within three elongated lenses that are also enriched in Co (Persson 1980). Due to the increasing importance of cobalt as a battery metal in recent years, SGU classified the Kiskamavaara deposit as a deposit of 'national interest' (SGU 2018). The deposit constitutes a mineralized zone that is approximately 900 m in length. The total resource is estimated at 3.2 Mt at 0.06% Co and 0.37% Cu (Persson 1981; Persson 1982).

Despite the general interest in northern Norrbotten ore deposits, only few studies have focused on the Kiskamavaara deposit itself (Martinsson, 2011; Metzger, 2019). Instead, several studies investigated the regional geology and structure (e.g., Bergman et al. 2001; Weihed et al. 2005; Martinsson et al. 2016; Bauer and Andersson 2021), thus providing a robust regional framework for further deposit- to grain-scale studies.

This study aims to understand the structural and geochemical controls on the Kiskamavaara IOCG-(Co) deposit with a focus on Co-Cu distribution at the deposit scale. Establishing a more detailed framework on Cu-Co distribution and associated structural and geochemical controls on the Kiskamavaara deposit has the potential to increase the understanding of the origin and evolution of cobalt in IOCG deposits.

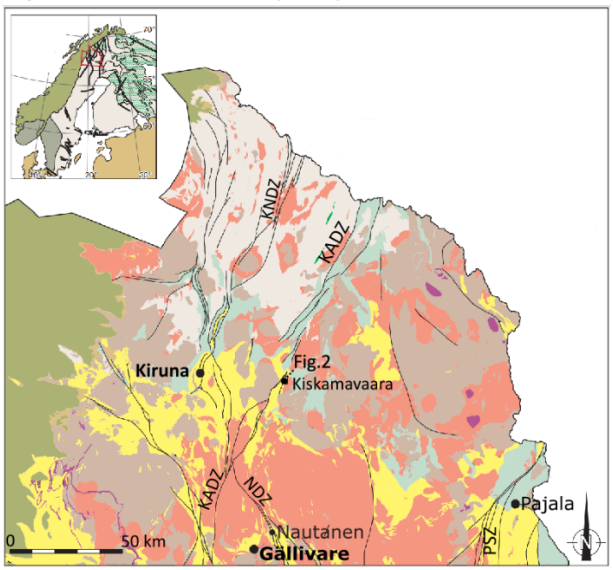

Figure 4: Simplified geological map of northern Norrbotten area (modified after Bergman, 2018). Green= Allochthonous rock, Mustard=Sedimentary cover rock, Purple= Gabbro, metagabbro, diabase, Orange=intrusive rocks (c. 1.8 Ga), Brown= Intrusive rocks (c.1.89-1.84), Yellow=Svecofennian supracrustal rock, Turquoise= Karelian rock, Grey= Archean rock, NDZ=Nautanen deformation zone, black line= ductile shear zone, KADZ= Karesuando–Arjeplog deformation zone, PSZ= Pajala shear zone, KNDZ=Kiruna-Naimakka deformation zone.

2 Geological background of the northern Norrbotten area

Northern Norrbotten is part of the Fennoscandian shield. The basement rocks consist of Archean (3.2-2.7 Ga) tonalite-trondhjemite-granodioritic gneisses (Martinsson et al., 2018; Bergman et al. 2001). Between 2.44 and 2.01 Ga intracontinental rifting caused mafic volcanism and the deposition of ultramafic sequences now being metamorphosed to a widespread greenstone sequence (Gaal & Gorbatschev 1987; Martinsson 1997). On top of the greenstones, Svecofennian supracrustal rocks

deposited during the Svecokarelian orogeny (ca 1.9-1.8 Ga). These rocks are strongly influenced by crustal reworking, magmatic intrusion events and metamorphism widespread in the northern parts of the Fennoscandian shield. In northern Norrbotten, deformation processes are associated to multistage magmatic and metamorphic events that are linked to early approximately N-S convergent continental margin processes and subsequent E-W crustal shortening, which caused a complex structural-metamorphic pattern (Bergman et al. 2001).

3 Geological characteristics of the Kiskamavaara deposit.

The primary lithologies in the Kiskamavaara area are intermediate porphyritic reddish-grey volcaniclastic rocks, tuffs and quartzite. Intense K-feldspar alteration affected the overall bedrock whereas scapolite-biotite alteration is limited to tuffites (Martinsson 2011). Carbonate-albite alteration is present in more distal parts of the deposit (Persson 1980; Martinsson 2011). Additionally, two intrusions are present in the Kiskamavaara area. An Orosirian granodiorite southwest of the deposit, and a metadiabase intruding the mineralization in the southern part of the deposit (Martinsson 2011).

The mineralization in Kiskamavaara comprises of magnetite, chalcopyrite, and Co-bearing pyrite (Ekström 1978). Central parts of the ore lenses consist largely of pyrite infill as the breccia matrix and decreases in intensity to disseminated pyrite-chalcopyrite-magnetite within the matrix at the lens margins (Martinsson 2011).

The deposit is flanked by two steep WNW-dipping shear zones with reverse oblique dextral components (Metzger 2019). Sets of brittle-ductile faults offset the shear zones with both dextral and sinistral sense-of-shears. Additionally, double plunging non-cylindrical folds with fold axes trending sub-parallel to the shear zones are present in the area (Bauer and Andersson 2021).

4 Results and discussion

4.1 Geological structures

Geophysical aeromagnetic data provided by Talga Group AB, shows a set of magnetic-high lineaments interpreted as fault/shear structures based on results in previous studies, e.g., Lynch et al. (2018) and Bauer et al. (2022). The magnetic anomalies indicate a set of NE-SW trending first order ore proximal structures of which one deflects into a E-W trend (Fig. 2). Between the NE-SW trending structures, four N-S trending second order structures connecting both first order structures are indicated on the aeromagnetic map (Fig. 2). Most of the lineaments show dextral offsets along later NW-SE structures or sinistral offset along E-W to NE-SW directions.

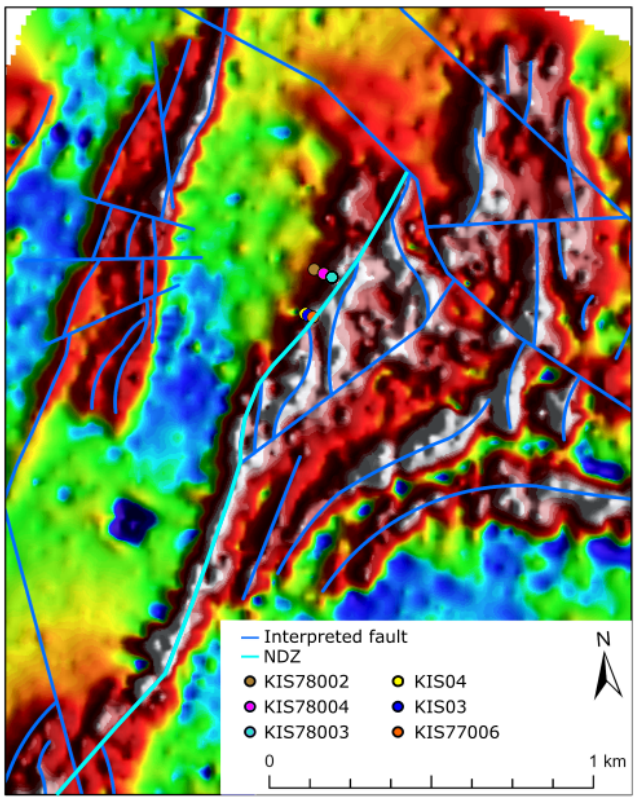

Figure 5: Structural interpretation of the Kiskamavaara deposit on top of EM geophysical map. The drill core locations correspond with the drill cores in Figure 4. NDZ = Nautanen deformation zone.

4.2 Geochemical analyses

Chemical analyses of four drill cores in the central part of the deposit indicate the rocks are sub-alkaline with basaltic, andesitic, rhyolitic/dacitic and minor trachytic compositions (Pearce 1996; Fig.3). The trachytes exhibit a similar composition to the rhyolite/dacite group albeit being slightly more alkaline. Therefore, the rhyolite/dacite and trachyte will be regarded as one group.

Furthermore, the rock samples display low concentrations of Ti and Zr, indicating that the porphyritic rocks in the central part of the Kiskamavaara deposit belong to the Porphyrite group (Bergman et al. 2001). Plotting Cu vs Co shows a cluster without a clear trend, indicating a low correlation between the occurrence and distribution of both metals in the deposit (Fig. 3).

We suggest the low correlation between Co and Cu mirrors either an evolving mineralization system or a multiphase mineralization/remobilization event(s). In either case further evaluation of the mineralization is needed for concluding remarks

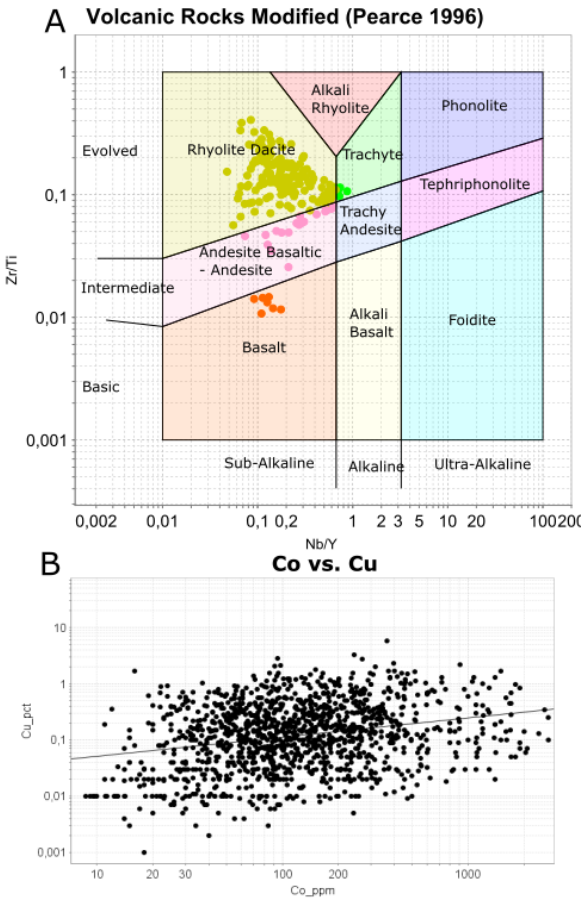

Figure 6: A: The rock classification model after Pearce (1996) shows that four rock types are present in the Kiskamavaara area. B: Co vs. Cu plot with regression line shows a weakly correlated cluster of datapoints between both elements.

4.3 Co-Cu Mineralization geometry

Geochemical analyses of drill cores obtained by SGU and Talga Group AB, combined with structural interpretations based on aeromagnetic maps indicate that the junctions between first and second order structures were the most favorable trap sites in the system. The second-order structures were only drilled near the ore proximal first order structure. Since the mineralization is located around the fault junctions the mineralization may extend along the second order structures and is not yet constrained in that direction. Such an interpretation would be largely in line with the structural configuration of the Nautanen deposit (Bauer et al. 2022).

The Kiskamavaara mineralization Consists of three separate clusters along the first order structure. Of the three clusters, the middle cluster exhibits the highest Co-Cu concentrations with an enrichment factor of 108.8 Co and 953.3 Cu compared to the average upper continental crust in up to 2 meter intervals (Fig.4). The mineralization clusters show a zoning pattern of central mainly Co-bearing pyrite, grading into decreasing Co concentrations but increasing Cu concentrations. Towards the cluster margins Cu decreases again and only some Co remains. Presence of cobalt without copper in the furthest margins of the mineralization possibly indicates either primary Co-Cu deposition with a changing mineralization character or that cobalt was transported further than copper during remobilization. However, further investigations are necessary to fully comprehend the metal evolution in the deposit.

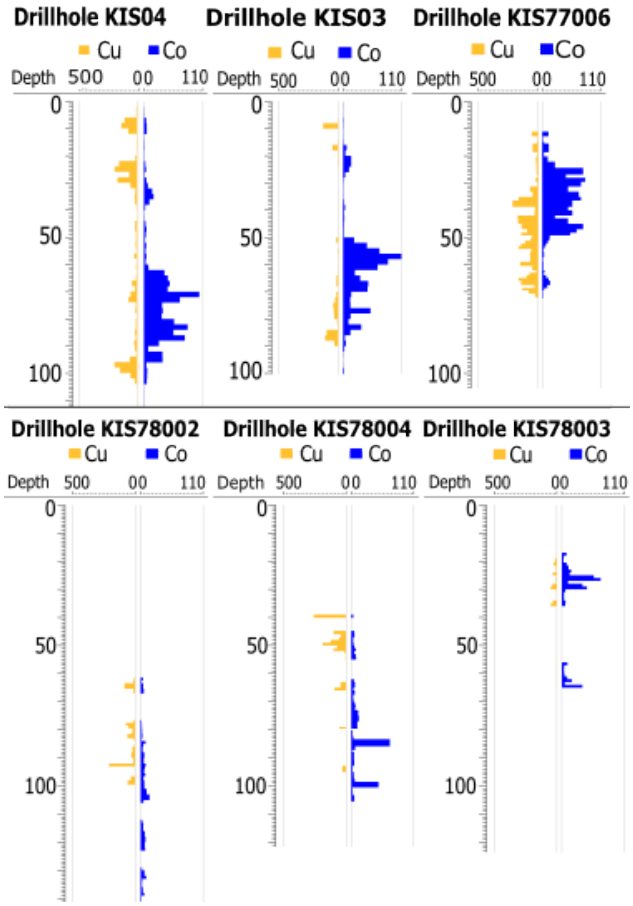

Figure 7: Schematic overview of drill cores showing the Co-Cu distribution normalized to the average upper continental crust within the center of the mineralization (top panel) and the mineralization margin (bottom panel). Drill core locations in Figure 2.

5 Conclusions

The Kiskamavaara deposit is a structurally controlled IOCG-(Co) deposit, characterized by the occurrence of three Co-Cu mineralization clusters with the highest mineralization grades concentrated in the central part decreasing outwards. The zonation pattern of the mineralization shows a wider distribution of cobalt compared to copper into the mineralization margins, which either indicates an evolving mineralisation character, a multiphase mineralization event or different behaviors during later remobilization. The centers of the mineralization clusters are primarily situated at the junction of the main NNW-SSE shear zone and second-order brittle-ductile NW-SE structures. Cobalt bearing pyrite is the main ore mineral in the Kiskamavaara deposit and frequently accompanied by chalcopyrite.

Whole rock geochemical analysis indicates that the central part of the Kiskamavaara deposit is composed of three rock types: basalts, rhyolites/dacites and andesites (Pierce 1996). Both the Ti and Zr content in the porphyritic rocks are low, which indicates that they belong to the Kiruna porphyrite group.

Acknowledgements

This project was funded from the European Union's Horizon Europe research and innovation program under Grant agreement n°1010557357, EIS – Exploration Information System.

References

Bauer TE, & Andersson J, (2021) Structural controls on Cu-Au mineralization in the Svappavaara area, northern Sweden–the northern continuation of the IOCG-hosting Nautanen deformation zone. In Paleoproterozoic deformation in the Kiruna-Gällivare area in northern Norrbotten, Sweden: Setting, character, age, and control of iron oxide-apatite deposits. Doctoral thesis, Luleå University of Technology.

Bauer TE, Lynch EP, Sarlus Z, Drejing-Carroll D, Martinsson O, Metzger N, & Wanhainen C, (2022) Structural Controls on Iron Oxide Copper-Gold Mineralization and Related Alteration in a Paleoproterozoic Supracrustal Belt: Insights from the Nautanen Deformation Zone and Surroundings, Northern Sweden. Economic Geology, 117(2), 327–359. https://doi.org/10.5382/econgeo.4862

Bergman S, (2018) Geology of the Northern Norrbotten ore province, northern Sweden. SGU Rapporter och meddelanden

Bergman S, Kübler L, & Martinsson O, (2001) Description of regional geological and geophysical maps of northern Norrbotten County (east of the Caledonian orogen).

Ekström T, (1978). Koboltförande pyrit i två profiler från Kiskamavaara. Sveriges geologiska undersökning Brap 78001.

Gaal, G, & Gorbatschev R, (1987) An Outline of the Precambrian Evolution of the Baltic Shield. In Precambrian Research (Vol. 35). https://doi.org/10.1016/0301-9268(87)90044-1

Lynch, EP., Bauer, TE., Jörnberger, J., Smarlus, Z., Morris, G., & Persson, PO. (2018). Petrological and structural character of c. 1.88 Ga meta-volcanosedimentary rocks hosting iron oxide-copper-gold and related mineralisation in the Nautanen–Aitik area, northern Sweden. SGU Rapporter och meddelanden, 141, 107-150.

Martinsson O, (1997) Tectonic setting and metallogeny of the Kiruna greenstones. Doctoral thesis, Luleå University of Technology.

Martinsson O, (2011) Kiskamavaara a shear zone hosted IOCG-style of Cu-Co-Au deposit in Northern Norrbotten, Sweden. Biennial SGA meeting, Antofagasta, Chile, Abstract, 470-472.

Martinsson O, Billström K, Broman C, Weihed P & Wanhainen C, (2016) Metallogeny of the Northern Norrbotten Ore Province, northern Fennoscandian Shield with emphasis on IOCG and apatite-iron ore deposits. Ore Geology Reviews, 78, 447-492. https://doi.org/10.1016/j.oregeorev.2016.02.011

Martinsson O, Bergman S, Persson PO & Hellström, FA, (2018) Age and character of late-Svecokarelian monzonitic intrusions in north-eastern Norrbotten, northern Sweden. In: Bergman, S.: Geology of the Northern Norrbotten ore province, northern Sweden. Rapporter och Meddelanden 141, Sveriges geologiska undersökning. pp 381–399.

Metzger N, (2019) Structural controls on the shear zone hosted, IOCG-style Kiskamavaara Cu-Co-Au mineralization. MSc-thesis, Luleå University of Technology.

Pearce JA (1996) Pearce 1996 volcanic model. In Wyman, D.A., Ed., Trace Element Geochemistry of Volcanic Rocks: Applications for Massive Sulphide Exploration: Geological Association of Canada, Short Course Notes, 12, 79–113.

Persson G (1980) Kiskamavaara koppar-koboltfyndighet Geologisk beskrivning och kvantitativ beräkning av koppar-koboltinnehållet del 1, Sveriges geologiska undersökning Brap 80524.

Persson G (1981) Kobolt-kopparfyndigheten vid Kiskamavaara. Del 1 tonnage och haltberäkning, del 2 borrprotokoll och analysintyg, Sveriges geologiska undersökning Brap 81552.

Persson G (1982) Kiskamavaara tonnageberäkning på koppar och kobolt, Sveriges geologiska undersökning Brap 82509.

SGU (2018) Nautanen och Kiskamavaara blir riksintressen, https://www.sgu.se/arkiv/arkiv-nyheter/2018/juli/nautanen-och-kiskamavaara-blir-riksintressen/

Weihed P, Arndt N, Billström K, Duchesne JC, Eilu P, Martinsson O, Papunen H, & Lahtinen R, (2005) 8: Precambrian geodynamics and ore formation: The Fennoscandian Shield. https://doi.org/10.1016/j.oregeorev.2005.07.008